THE UNIVERSITY OF ADELAIDE

# PROTEROZOIC TECTONIC MODELS WITH APPLICATION TO THE MOUNT PAINTER INLIER.

by J. TEASDALE

November, 1993

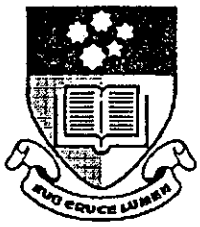


THE UNIVERSITY OF ADELAIDE

Department of Geology and Geophysics

# Proterozoic tectonic models with application to the Mount Painter Inlier

Jonathan Teasdale, B.Sc.

Thesis submitted as partial fulfilment for the
Honours Degree of Batchelor of Science

November, 1993

Supervisor: M Sandiford

# Table of Contents


ABSTRACT 1

TABLE OF CONTENTS 2

PREAMBLE 3

PART ONE **Geological Investigations in the Mount Painter Inlier**

Chapter 1 A geological overview of the Mount Painter Inlier 5

Chapter 2 Lithologies of a section of the Mount Painter Inlier: The Paralana Hot Springs - Mount Adams Valley area 8

Chapter 3 Structural and metamorphic evolution 23

Chapter 4 Tectonic evolution of the Paralana Hot Springs - Mount Adams Valley area 31

PART TWO **Tectonics of Proterozoic Orogenic Belts**

Chapter 5 Orogenic aspects of Proterozoic tectonics 38

Chapter 6 On the mechanical plausibility of ensialic orogenesis 43

Chapter 7 Discussion 58

ACKNOWLEDGMENTS 61

REFERENCES 62

APPENDICES

Appendix 1 Lithospheric strength calculations 67

Appendix 2 *Delamination* program - *Mathematica*™ code 73

Appendix 3 Selected microprobe data and geothermometry 86

Appendix 4 Sample data 101

Appendix 5 Geological map and block diagram: Paralana Hot Springs - Mount Adams Valley area 103

# Abstract

Since many features of Proterozoic orogenic belts are difficult to reconcile with classical plate tectonic theory, alternative mechanisms have been developed to explain phenomena such as high-temperature–low-pressure metamorphism and distinctive intracratonic geochemistry, as seen in the Mount Painter Inlier and other Proterozoic orogenic belts. Delamination of part or all of the mantle lithosphere may play an important role in initiating, localising or terminating convergent deformation in ensialic (intracratonic) settings. The 'thin sheet' model presented here investigates the mechanical plausibility and consequences of ensialic mantle lithosphere delamination. Results indicate that mantle lithosphere delamination will initiate and localise convergent deformation given sufficient tectonic driving forces. Mantle lithosphere delamination from a thickened lithosphere may lead to extensional collapse.

Two discrete Proterozoic tectonothermal events were recognised in the Mount Painter Inlier. Syn-post kinematic, high-temperature metamorphism and plutonism indicates heating may have post-dated deformation and that mantle lithosphere delamination may have occurred in response to thickening.

# Preamble

Many features of Proterozoic orogenic belts are difficult to reconcile with classical plate tectonic theory. These features include their supposed 'ensialic' (intracratonic) setting, the abundance of high-temperature–low-pressure metamorphism, evidence for vertical crustal accretion, and distinctive geochemistry, together with an absence of modern Wilson Cycle tectonic signatures such as obducted oceanic crust (ophiolites), calc-alkaline magmatism (andesites) and high-pressure (paired) metamorphic belts [e.g. Kröner, 1983; Etheridge et al., 1987]. In recent years the idea that thermal evolution of the continental lithosphere may involve decoupling of strain between the crust and mantle lithosphere [Houseman et al., 1981] has had an important impact on models for the evolution of a number of Proterozoic high-temperature–low-pressure metamorphic terrains [e.g. Sandiford, 1989b; Sandiford & Powell, 1990; Loosveld & Etheridge, 1990]. Several scenarios have been proposed to explain such features in terms of mantle lithosphere delamination [e.g. Kröner, 1981; 1983; Etheridge et al., 1987; Loosveld & Etheridge, 1990].

Despite the popularity of such scenarios, very little work has been done to (1) rigorously evaluate the structural and metamorphic evolution of many Proterozoic mobile belts in an 'ensialic' context, and (2) quantitatively examine their mechanical plausibility. The aim of this project is to accomplish this work using geological evidence from the Mount Painter Inlier.

The first part of this thesis comprises an investigation of the structural and metamorphic evolution of the Mount Painter Inlier. In the second part of this thesis the mechanical plausibility of proposed Proterozoic orogenic scenarios is quantitatively examined and applied to the Proterozoic record of the Mount Painter Inlier.

# PART ONE

## Geological investigations in the Mount Painter Inlier

# Chapter 1

## Geological overview of the Mount Painter Inlier

### 1 Introduction

The Mount Painter Inlier in the Northern Flinders Ranges, South Australia is an exhumed antiformal section of pre-Adelaidean crystalline basement, which is unconformably overlain by Adelaidean sediments (see figure 1.1). Despite mineral exploration over the last fifty years very little is known about the geology of the inlier.

Coats & Blissett [1971] briefly outline a simple pre-Adelaidean stratigraphy comprising a thick basal metasedimentary sequence (the 'Radium Creek Metamorphics') intruded by a suite of Mesoproterozoic felsic intrusives (the 'Older Granite Suite') and extrusives. Deformation and metamorphism was ascribed to younger (Palaeozoic) events. Differences in structural style were attributed to strain partitioning between rock types of varying competency during a Palaeozoic orogeny. Recent work by Teale [in press] and Sheard [pers. comm.] suggests that the geological history of the Mount Painter Inlier is longer and more complex than previously thought, necessitating major stratigraphic modifications and a more detailed structural and metamorphic evaluation.

To accomplish this, an area encompassing the Paralana Hot Springs and Mount Adams Valley was mapped during April, May and July 1993 (see figure 1.1 & Appendix 5), in conjunction with Bruce Schaefer . Of particular interest is the supposed Adelaidean outlier forming Mount Adams Valley, colloquially known as Hidden Valley (Appendix 5).

Coats & Blissett [1971] mapped four basic units in the Paralana Hot Springs - Mount Adams Valley area: the basal Radium Creek Metamorphics, Mesoproterozoic intrusives, an Adelaidean outlier and the early Palaeozoic British Empire Granite. Mapping revealed a basal suite of highly deformed gneisses (Four Mile Creek Gneiss Suite) unconformably overlain by a

sequence of moderately deformed metasediments (Freeling Heights Metasediments, Yagdlin Phyllite and Mount Adams Quartzite). Both units have been intruded by the Mount Neill Granite Porphyry and the British Empire Granite. Lithological descriptions for these units are provided in Chapter 2.

A structural and metamorphic evaluation of the Paralana Hot Springs - Mount Adams Valley area is presented in Chapter 3. Chapter 4 contains a discussion of the possible tectonic evolution of the Mount Painter Inlier.

# 2 Previous work

Extensive copper mining around the turn of the century and uranium mining spanning the first half of this century, together with numerous smaller ventures earned the Mount Painter region a reputation of great mineral wealth. Subsequent extensive mineral exploration (uranium, gold, base metals, rare earths) of the Mount Painter Inlier by Exoil (later Transoil), North Flinders Mines, Anaconda and CRA has failed to reveal any significant ore concentrations despite numerous tantalising assays. Very little exploratory work has been published for the Paralana Hot Springs - Mount Adams Valley area. SADME Open File data contains a few large scale maps and passing references to Mount Adams Valley (named 'Carthew Valley' in North Flinders Mines reports). Drilling by Anaconda in the north-west of the area and North Flinders in the south was of no economic significance and no interpretations were made of the brief drill logs. Recent work by CRA has not been released.

Blight [1977] mapped a southern portion of the area as part of an honours project. His thesis contains some petrological and geochemical data. Coats & Blissett [1971] is the only significant published reference and only briefly outlines the pre-Adelaidean geology. Geological maps are large-scale only (1:132000).

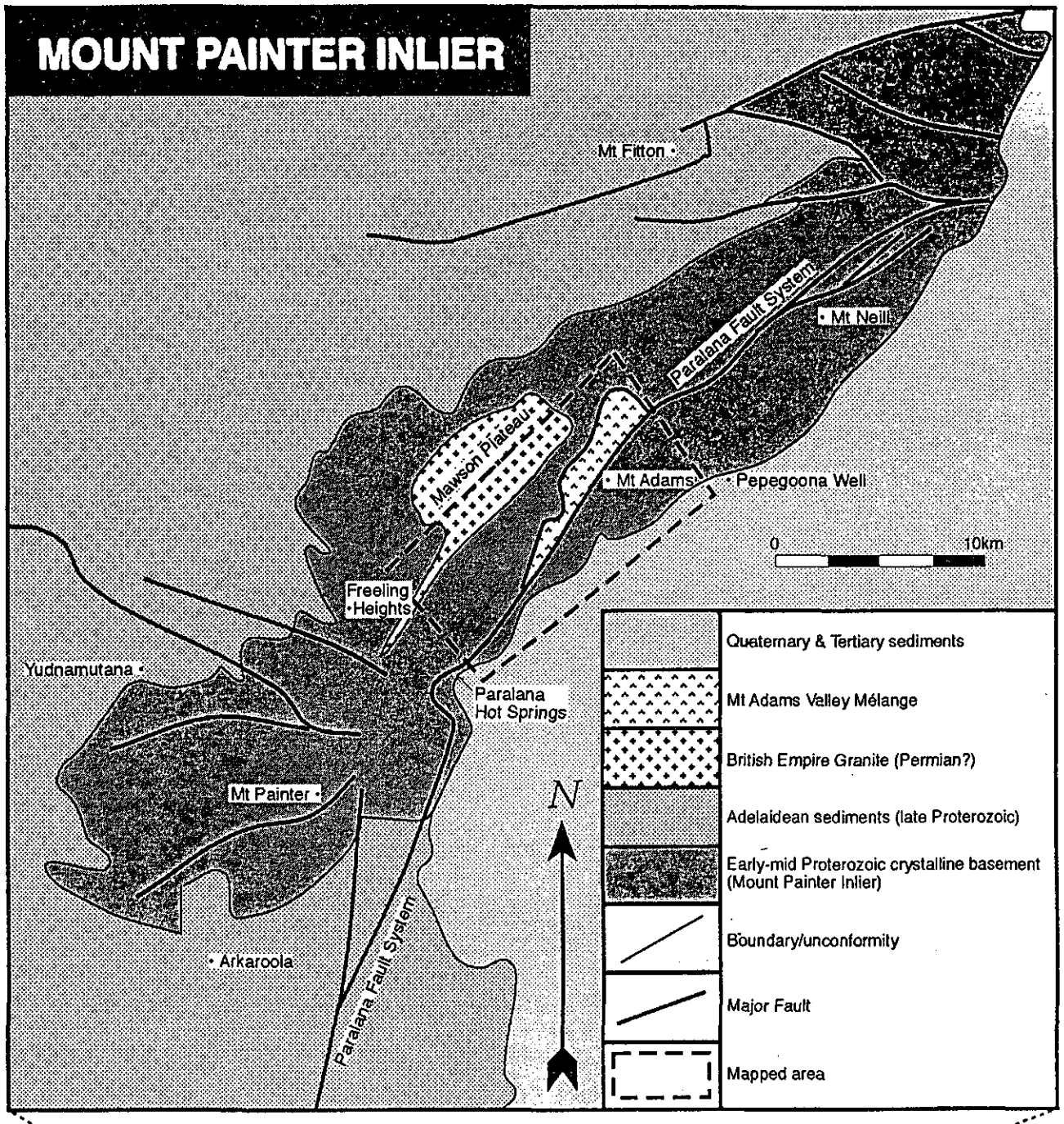


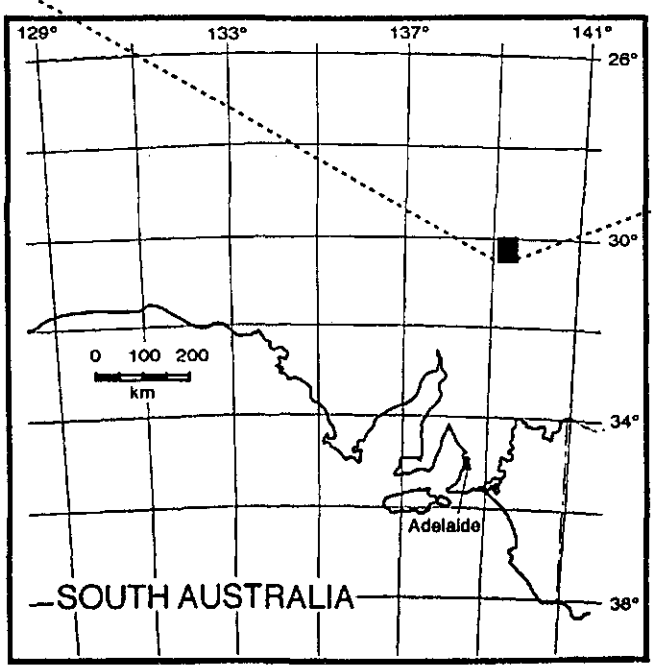


# Figure 1.1

Location map and regional geology of the Mount Painter Inlier [after Coats & Blissett, 1971].

# Chapter 2

## Lithologies of a section of the Mount Painter Inlier: The Paralana Hot Springs - Mount Adams Valley area

## 1 Introduction

Mapped lithologies of the Paralana Hot Springs - Mount Adams Valley area differ from previous data and are summarised in table 2.1. Colour plates illustrating these lithologies can be found at the end of the chapter.

| Name | Age | Previous name* | Brief description |
|---|---|---|---|
| Four Mile Creek Gneiss Suite | 2.4-2.0Ga # | Lower Radium Creek Metamorphics (unnamed member of Freeling Heights Quartzite) | Highly deformed and metamorphosed sequence of ortho- and paragneisses |
| Freeling Heights Metasediments | >1565Ma | Upper Radium Creek Metamorphics (Freeling Heights Quartzite) | Moderately deformed sequence of feldspathic quartzites and mica schists |
| Yagdlin Phyllite and Mount Adams Quartzite | >1565Ma | Unchanged | Relatively undeformed low grade laminated grey-green phyllites and pink feldspathic quartzite |
| Mount Neill Granite Porphyry | 1565 ± 4Ma † | Unchanged | Relatively undeformed heterogeneous sequence of intrusive to sub-volcanic felsic granites, rhyolites and amphibolites |
| British Empire Granite | 270Ma ‡ | Unchanged | Undeformed leucocratic quartz–feldspar–muscovite granites and pegmatites |
| Mount Adams Valley Mélange | ? | Adelaidean Wywyana Formation | Chaotic mass of soft calcareous pale green quartzose grits and clays containing numerous exotic rafts (<1mm to 500m) |
| Lake Frome plains sediments | Mesozoic - Recent | Various | Flatlying, low grade marine and alluvial sediments |

**Table 2.1** Brief stratigraphic summary of the Paralana Hot Springs - Mount Adams Valley area.

* Previous names are taken from Coats & Blissett [1971].
\# Sm/Nd model age derived by Schaefer [1993].
† Model age [SADME unpublished data, 1993].
‡ Rb/Sr age derived by Schaefer [1993].

I interpret the Freeling Heights Metasediments to unconformably overlie the basal Four Mile Creek Gneisses. Evidence for this unconformity is discussed in §3 (this chapter). The Yagdlin Phyllite and Mount Adams Quartzite appear synchronous with the Freeling Heights Metasediments. The Mount Neill Granite Porphyry and British Empire Granite intrude all gneisses and metasediments. The enigmatic Mount Adams Valley Mélange cannot be related structurally or stratigraphically with any other mapped units and intriguingly contains a variety of unusual, apparently exotic units as rafts (see §2.6).

In the following sections I provide a lithological overview of the Paralana Hot Springs - Mount Adams Valley area as illustrated in Appendix 5 (map).

# 2 Lithological descriptions

## 2.1 Four Mile Creek Gneiss Suite

The Four Mile Creek Gneiss Suite is a highly deformed, aerially extensive sequence of ortho- and paragneisses, previously mapped as the lower unnamed member of the Freeling Heights Quartzite [Coats & Blissett, 1971]. The Four Mile Creek Gneisses appear to be substantially older than the Freeling Heights Metasediments (see §3 this chapter). All sedimentary structures have been obliterated by intense deformation and metamorphism.

The Four Mile Creek Gneisses consist of migmatites, paragneisses and orthogneisses. Complex cross-cutting relationships and isotopic data suggest several phases of sedimentation and magmatism.

### 2.1.1 Migmatites

Quartzofeldspathic biotite-rich migmatites (probably orthogneissic) form large partially anatectic rafts in the orthogneisses described below. They also outcrop in the core of the $F_3$ anticlinorium (see Chapter 3).

### 2.1.2 Orthogneisses

The oldest orthogneiss consists of a coarse grained, heterogeneous, quartzofeldspathic, biotite rich, layered granite gneiss which is highly deformed and migmatitic in part. A suite of less deformed orthogneisses intrudes the migmatites and underlies the paragneisses. This suite includes

an early 'black and white' augen gneiss and various medium grained red feldspathic granite gneisses. A late stage fine grained, white leucocratic granite gneiss crosscuts all para- and orthogneisses. Schaefer [1993] provides a more comprehensive petrological, geochemical and geochronological assessment of these orthogneisses.

### 2.1.3 Paragneisses

A highly deformed paragneiss comprising alternating (~2-3mm) leucocratic quartzofeldspathic layers and melanocratic biotite – muscovite ± ilmenite ± apatite layers outcrops in the core of the anticlinorium described in Chapter 3 (see plate 3a). Prograde fibrous sillimanite has formed at the leuco-melanocratic interfaces. This unit appears to predate other paragneisses due to its deformational and metamorphic character.

A sequence of high grade metasediments including highly recrystallised medium-coarse grained quartzites (often micaceous) and sillimanite bearing gneisses (see plate 1a&b) appears to overlie the abovementioned paragneiss and orthogneisses. Interbeds include:

(i) medium grained, black, thin foliated and crenulated biotite – quartz ± garnet ± cordierite ± muscovite schists (plate 4c);

(ii) coarse grained, weakly foliated, grey-green phlogopite – quartz – corundum ± muscovite rocks;

(iii) coarse grained cordierite – orthoamphibole – anorthite – ilmenite rocks containing abundant acicular anthophyllite (plate 1f);

(iv) layered quartz – epidote ± plagioclase rocks (plate 1e);

(v) soft, fibrous, white sillimanite – tourmaline – biotite – (quartz) schists containing 75% fibrous sillimanite and large hexagonal tourmaline porphyroblasts (plate 1c);

(vi) green, medium grained tremolite – quartz – anorthite – ilmenite ± clinopyroxene calc-silicates (plate 1g&h);

(vii) coarse grained, grey epidote – garnet – anorthite – albite – sphene calc-silicates yielding retrograde amphiboles.

Bedding ($S_0$, defined by large scale lithological variation) is parallel to the major pervasive foliation and any primary sedimentary structures have been totally obliterated by intense isoclinal folding, upper amphibolite facies metamorphism and partial anatexis.

## 2.2 Freeling Heights Metasediments

The Freeling Heights Metasediments comprise an interbedded sequence of micaceous massive crossbedded quartzites and various mica schists. They were previously mapped as younger Freeling Heights group sediments by Coats & Blissett [1971]. The metasediments are highly fractured and anatectic in part with abundant pegmatitic quartz – feldspar – muscovite 'sweating' veins which appear related to the British Empire Granite. Schistose units include coarse grained muscovite ± corundum and biotite – plagioclase ± quartz ± corundum ± garnet ± cordierite* rocks (plate 2a). While distinctly different in metamorphic grade from the basement paragneisses, field discrimination between these two units proved difficult due to similar weathering patterns and their highly fractured nature. Since Freeling Heights Metasediments unconformably overlie the Four Mile Creek Gneisses (see §3) and are intruded by the Mount Neill Granite Porphyry, their age is constrained to the Mesoproterozoic.

## 2.3 Metasediments east of the Paralana fault

The metasediments occurring to the east of the Paralana Fault were originally mapped as the oldest sediments of the Mount Painter Inlier# [Coats & Blissett, 1971]. They are lithologically distinct from any other mapped units and comprise:

(i) **Yagdlin Phyllite:** A fine grained sequence of grey-green, micaceous schists and phyllites with garnet and talc bearing interbeds (plate 2f);

(ii) **Mount Adams Quartzite:** A fine grained, feldspathic, cross-bedded quartzite which gradationally overlies the Yagdlin Phyllite (plate 4h).

A well preserved contact metamorphic/metasomatic aureole adjacent to the Mount Neill Granite contains abundant phlogopite – corundum ± sillimanite ± tourmaline ± cordierite units† (plate 3e).

---

* All cordierite in the Freeling Heights Metasediments has retrograded to quartz, corundum or chlorite.

# Coats & Blissett [1971] placed these units at the base of the Radium Creek Metamorphics due to their apparent intrusion by small pods of Pepegoona Porphyry. Field evidence suggests that these pods are in fact Mount Neill Granite Porphyry. Recent geochronological work has dated the Pepegoona Porphyry as being cogenetic with the Mount Neill Granite Porphyry [Sheard pers. comm., 1993], thus rendering this age constraint invalid anyway.

† Coats & Blissett [1971] mapped this as a thrusted contact.

## 2.4 Mount Neill Granite Porphyry

The Mount Neill Granite Porphyry comprises a heterogeneous sequence of relatively undeformed intrusive to sub-volcanic Mesoproterozoic (1565 ± 4Ma) granites, rhyolites and amphibolites. Abundant red, potassic, quartz-undersaturated high level granites form the bulk of the unit, although coarser grained Rapakivi textured granites with ovoid white feldspars outcrop in the north of the area. Large outcrops of coarse grained green phlogopite – chlorite - corundum ± sillimanite schist yielding spectacular blue sapphire are interpreted as rafts or roof pendants of older sediments, probably Yagdlin Phyllite. More detailed descriptions together with isotopic data are provided by Schaefer [1993].

## 2.5 British Empire Granite and associated pegmatites

The British Empire Granite comprises an undeformed, heterogeneous, coarse grained, quartzofeldspathic leucocratic, muscovite rich, S-type granite. Originally thought to be post-Delamerian (Ordovician) in age, recent work by Foden [pers. comm.] and Schaefer [1993] suggests it may be considerably younger - possibly Permian. Schaefer [1993] has suggests an emplacement age of 270Ma (Permian).

## 2.6 Mount Adams Valley Mélange

The Mount Adams Valley Mélange consists of a poorly sorted and consolidated pale green, carbonaceous, quartzose matrix of grits and clays containing numerous exotic clasts and rafts ranging from a few millimetres to over 500m in size (see plate 3f). It was previously mapped as brecciated/diapiric Adelaidean Wywyana and Opaminda Formation* [Coats & Blissett, 1971]. The material is conglomeratic in part and vague planar differentiation may be interpreted as bedding. Small (2-3mm) phlogopite and tourmaline crystals which occur in the matrix probably have metamorphic origins [Sandiford pers. comm., 1993].

Abundant British Empire pegmatites outcrop in Mount Adams Valley. Large

* The Mount Adams Valley fill resembles diapiric calc-silicates of the lower Burra group found at the Needles, west of Arkaroola Village [Sandiford pers. comm., 1993].

blocks (up to 500m) of Freeling Heights Metasediments appear to overlie the valley fill, suggesting a thrusted emplacement. Other clast/block types have distinct compositions and metamorphic grades implying very different histories from all other mapped units. These include:

(i) **Mafic granulites:** Small outcrops of fresh olivine – amphibole – plagioclase – clinopyroxene – spinel gabbro/granulite and 2-pyroxene granulites were found (plate 2b,c,d). These high grade rocks are extremely atypical of the region and do not relate compositionally to other units.

(ii) **Ultramafic units:** An olivine gabbro (troctolite), a coarse grained green pyroxene gabbro (unmetamorphosed and fresh) and several amphibolites were found.

(iii) **Calc-silicates:** Several very hard, high grade, intensely deformed, coarse grained calc-silicate units were found, which cannot be correlated with Adelaidean Wywyana Formation. Complex mineralogies included:

(a) quartz – anorthite – clinopyroxene – garnet – Kfeldspar – sphene – ilmenite (plate 3d);
(b) anorthite – clinopyroxene – garnet – Kfeldspar – wollastonite – sphene – calcite – ilmenite – apatite (plate 3c);
(c) quartz – Kfeldspar – clinopyroxene – biotite.

(iv) **Pelitic gneisses:** A crenulated biotite – corundum – quartz – feldspar rock was found.

(v) **Dolomites, marbles and quartzites:** These highly weathered, undeformed sedimentary units outcrop with occasional coherent bedding and sedimentary structures including ripple marks and foreset beds and may be undeformed Adelaidean sediments. They do not appear to relate compositionally to the matrix.

## 2.7 Lake Frome plains sediments

Marine and alluvial sediments of the Lake Frome plains were deposited during the Mesozoic, Tertiary and Quaternary [Coats & Blissett, 1971]. They are generally flatlying but are drag folded and faulted by Tertiary activity along the Paralana Fault System. Jurassic flora fossils were found in the north-east of the area.

# 3 Evidence for disparity between the Four Mile Creek Gneiss Suite and the Freeling Heights Metasediments

I interpret the Four Mile Creek Gneiss Suite to be older than the Freeling Heights Metasediments based on the following evidence:

(i) the Four Mile Creek Gneisses are of significantly higher metamorphic grade (see Chapter 3);

(ii) the Four Mile Creek Gneisses are more intensely deformed (see Chapter 3);

(iii) sudden orientation changes across the gneiss-metasediment boundary cannot be reconciled structurally and must be attributed to a fault or an unconformity.

Field recognition of this discontinuity is difficult in the mapped area, due to the weathered nature of critical outcrops. The contact between the Four Mile Creek Gneiss Suite and the Freeling Heights Metasediments in both the south and north of the area appears unconformable (see Appendix 5).

# Plate 1

## Photomicrographs from the Four Mile Creek Gneiss Suite

Field of view = 1.8 x 1.4mm

(a) Fibrous sillimanite – Kfeldspar – quartz – muscovite gneiss (A1017-JPT027) showing the prograde reaction q + mus = ksp + sill (q=quartz, mus=muscovite, ksp=Kfeldspar, sill=sillimanite). Sillimanite growth has postdated major foliation development.

(b) Mylonitised sillimanite-bearing paragneiss (A1017-JPT070b) from the Paralana shear zone. Sillimanite needles are now sub-parallel.

(c) Fibrous sillimanite – tourmaline rock (A1017-JPT029d) in plane polarised light (sill=sillimanite, tour=tourmaline).

(d) Sillimanite – quartz – biotite gneiss (A1017-JPT026), showing coexisting prismatic sillimanite and biotite, aligned forming the $S_2$ foliation (bi=biotite, sill=sillimanite, q=quartz).

(e) Highly recrystallised epidote quartzite (A1017-JPT096) showing dark green scapolite (e=epidote, sc=scapolite, q=quartz).

(f) Cordierite – orthoamphibole rock (A1017-JPT115) with opaque ilmenite and plagioclase (cd=cordierite, oa=orthoamphibole [anthophyllite], p=plagioclase [anorthite]). Random alignment of crystals indicates post-kinematic metamorphism or metasomatism.

(g) Orthoamphibole – anorthite calc-silicate (A1017-JPT081) showing prismatic cummingtonite and ilmenite, aligned forming the $S_2$ foliation (an=anorthite, ilm=ilmenite, oa=orthoamphibole).

(h) Prograde example of (g) showing large green diopside crystals have replaced orthoamphibole (i.e. granulite facies metamorphism). Random alignment of crystals indicates post-kinematic metamorphism associated with later plutonism. Sample number A1017-JPT078.

1a

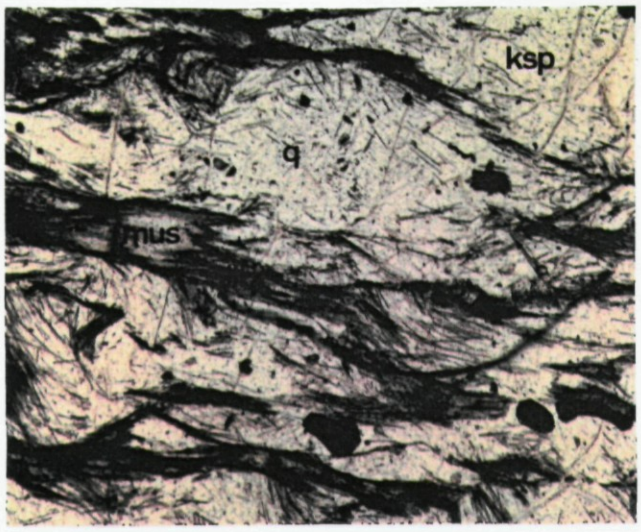


b

c


d

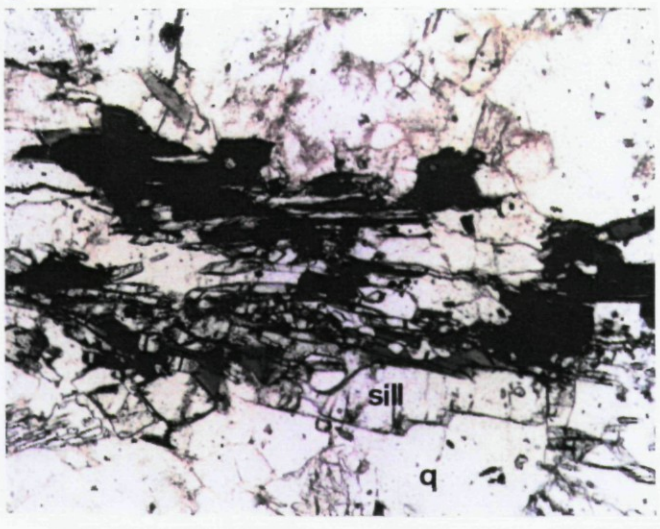


e

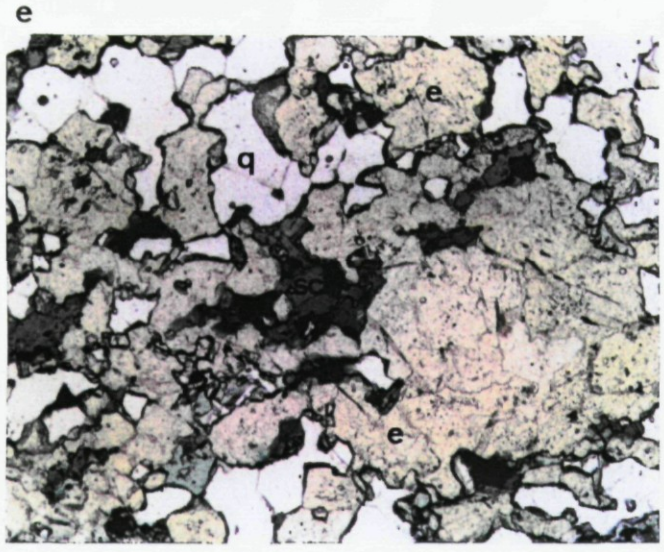


f

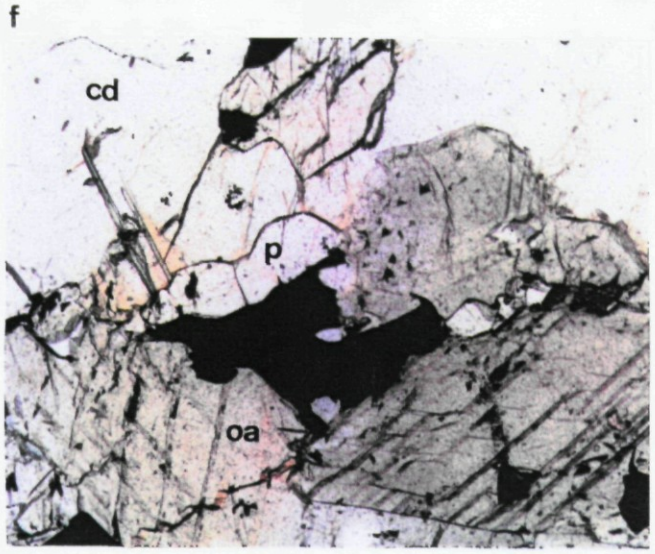


g

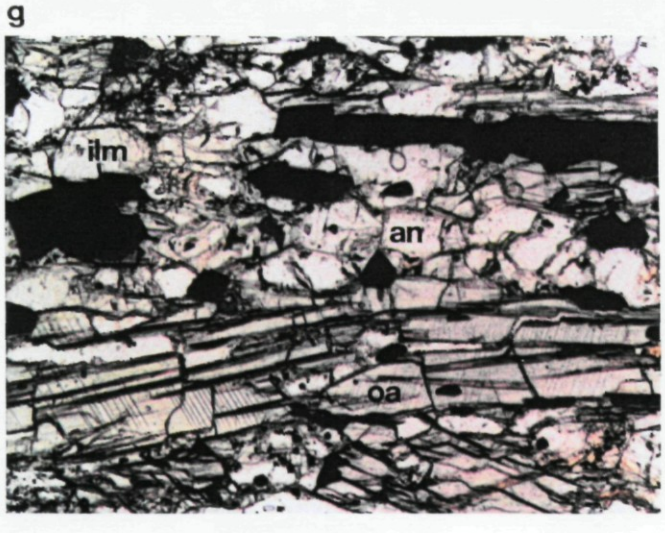


h

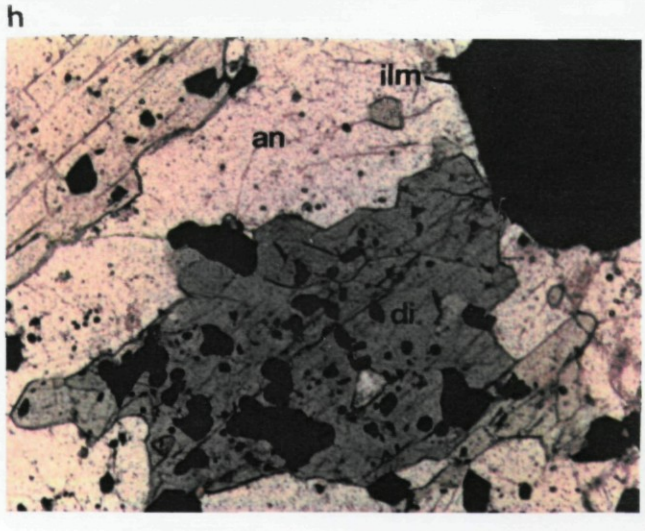

# Plate 2

## Miscellaneous photomicrographs

**Field of view = 1.4 x 1.8mm**

(a) Garnet – biotite – (relict) cordierite schist (A1017-JPT010) from the Freeling Heights Metasediments (g=garnet, bi=biotite). Sample used for geothermometry (see Appendix 3).

(b) Two-pyroxene granulite (A1017-JPT108) from the Mount Adams Valley Mélange (opx=orthopyroxene, cpx=clinopyroxene, p=plagioclase). Sample used for geothermometry (see Appendix 3).

(c) Green spinel – clinopyroxene (augite) symplectites growing from olivine (forsterite) and plagioclase (anorthite) in a meta-gabbro from the Mount Adams Valley Mélange (A1017-JPT033, sp=spinel, cpx=clinopyroxene, ol=olivine, p=plagioclase).

(d) As above, with crossed polars. Note high relief, blue clinopyroxene.

(e) Coarse grained clinopyroxene (diopside) – garnet (andradite) – sphene – plagioclase (anorthite) – Kfeldspar calc-silicate from the Mount Adams Valley Mélange (A1017-JPT084, cpx=clinopyroxene, g=garnet, sph=sphene, p=plagioclase, ksp=Kfeldspar).

(f) Relict ?cordierite porphyroblast in the Yagdlin Phyllite (A1017-JPT002), showing metamorphism postdated deformation (i.e. $S_3$ mica foliation development).

2a

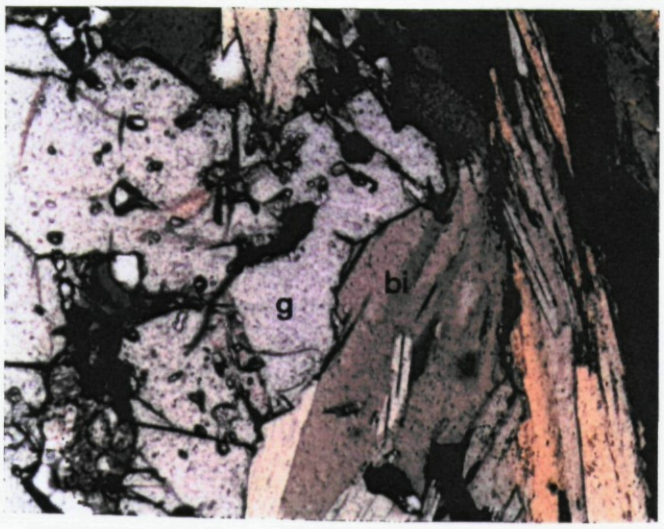


b

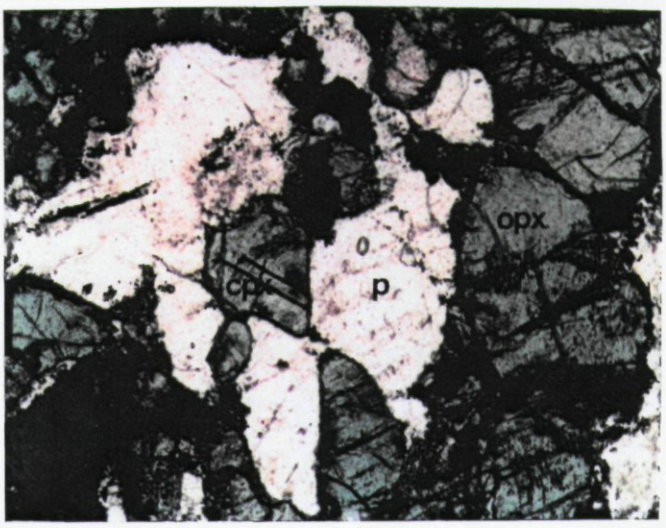


c

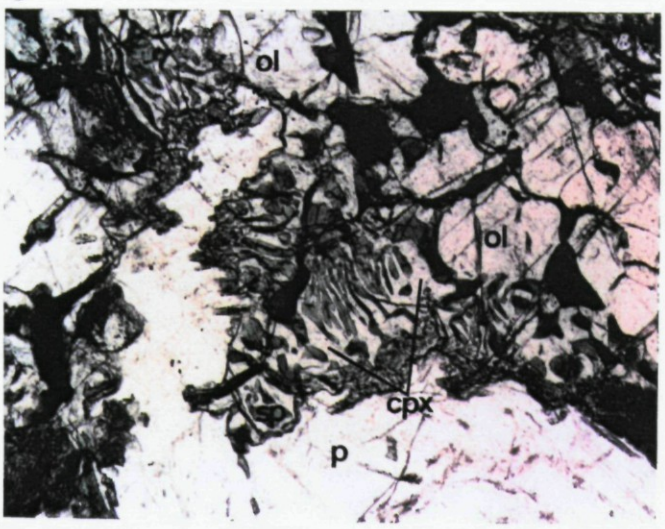


d

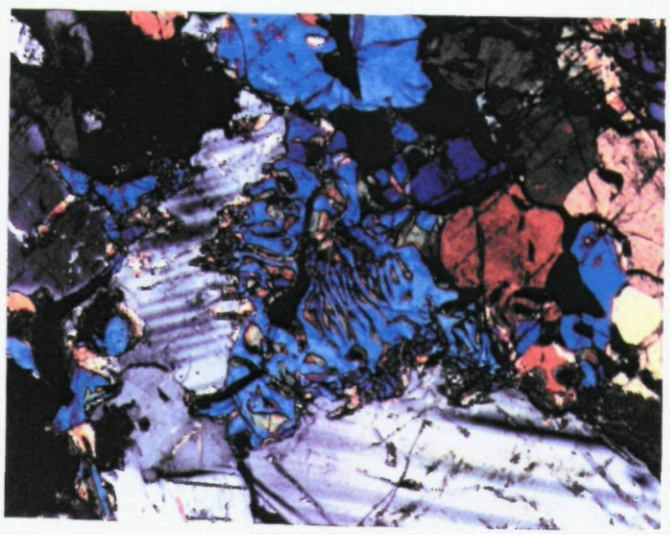

e

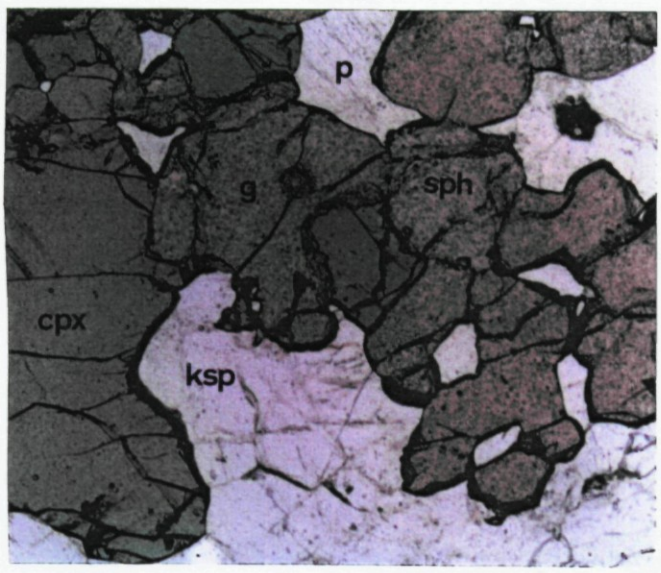


f

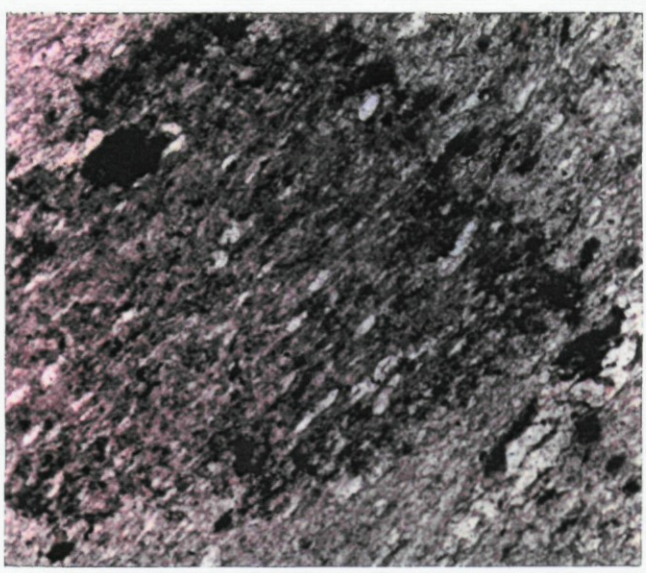

# Plate 3

## Hand specimen photographs

(a) Sillimanite – Kfeldspar – quartz – biotite – magnetite gneiss from the oldest paragneisses in the Four Mile Creek Gneiss Suite (A1017-JPT066). Note distinct $S_1$ gneissic segregation of orange Kfeldspar, mica, quartz and sillimanite and the sillimanite elongation lineation, $L_1$.

(b) Sillimanite – biotite – Kfeldspar – muscovite schist from the Four Mile Creek Gneiss Suite (A1017-JPT029a).

(c) Coarse grained wollastonite – clinopyroxene (diopside) – garnet (andradite) – anorthite – sphene – Kfeldspar – calcite – ilmenite calc-silicate from the Mount Adams Valley Mélange (A1017-JPT092). All white material is wollastonite.

(d) Highly strained Kfeldspar (pink) – diopside (green) – garnet calc-silicate from the Mount Adams Valley Mélange (A1017-JPT086).

(e) Contact metamorphosed and metasomatised Yagdlin Phyllite showing prismatic, white sillimanite needles reacting to bright blue sapphire (A1017-JPT107). Random nature of sillimanite prisms indicates post-kinematic metamorphism and metasomatism.

(f) Well consolidated sample of the Mount Adams Valley Mélange, showing chaotic nature of both matrix and clasts (A1017-JPT040).

3a

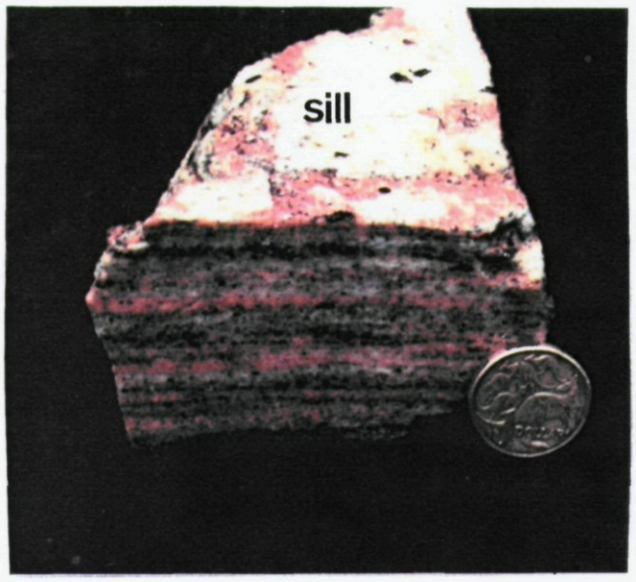


b

c

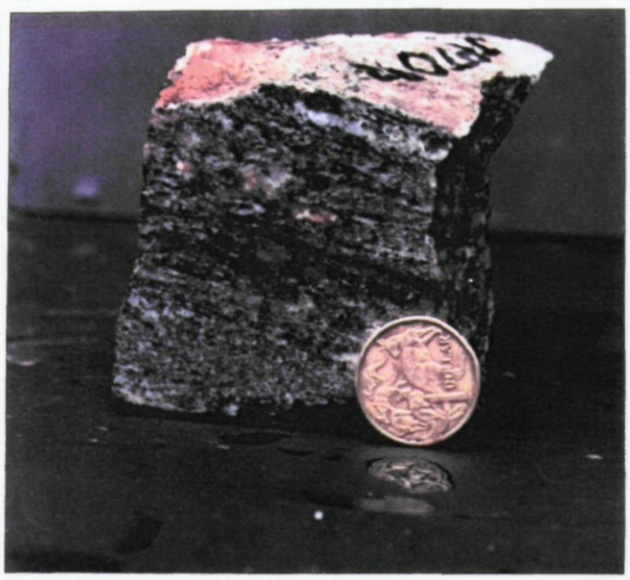

d

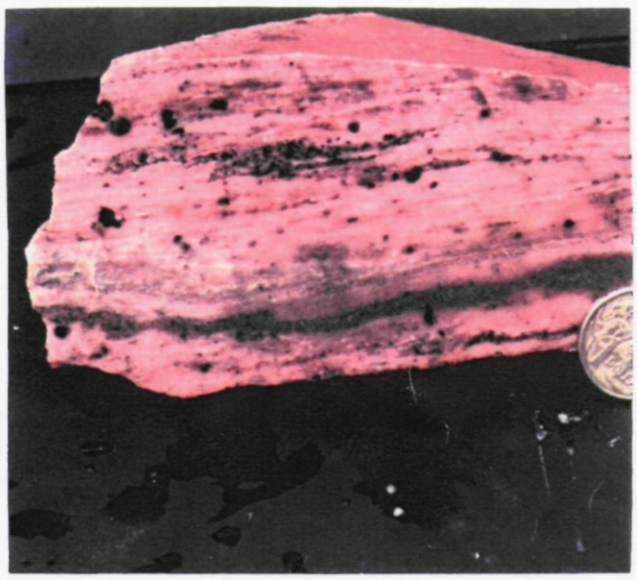

e

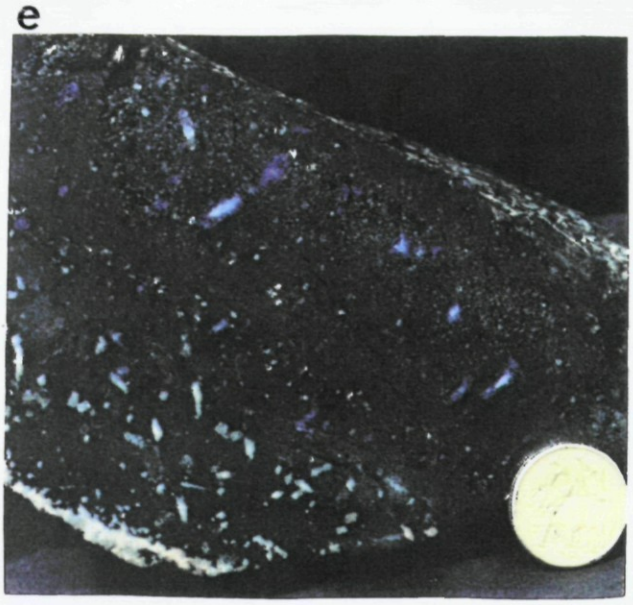

f

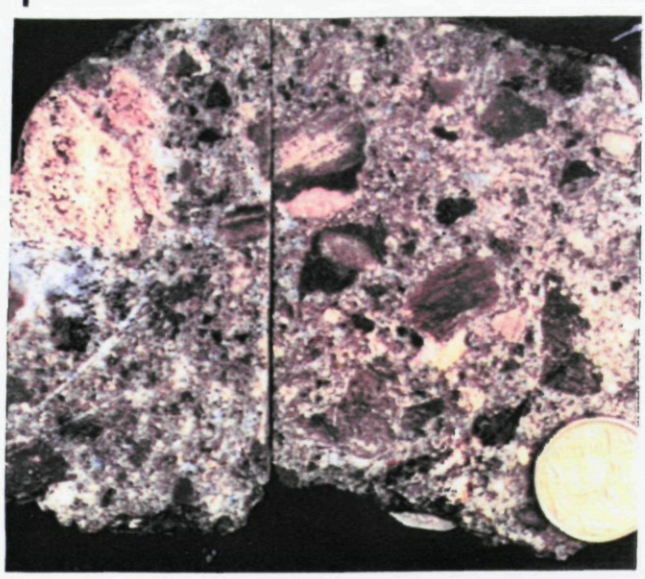

# Plate 4

## Structural photographs and photomicrographs

(a) Chaotic folding and partial anatexis in the basal migmatites of the Four Mile Creek Gneiss Suite, Hot Springs Creek.

(b) $F_2$ isoclinal/elasticas folding of $D_1$ quartz veins in a Four Mile Creek orthogneiss, Paralana Plateau.

(c) $F_4$ crenulations of the $S_2$ foliation in a biotite schist from the Four Mile Creek Gneiss Suite, Four Mile Creek (A1017-JPT083).

(d) $F_3$ parallel folds and small scale growth faults in the Yagdlin Phyllite showing $S_3$ axial planar foliation (lens cap gives scale).

(e) Mylonitised Mount Neill Granite Porphyry (A1017-JPT110) showing characteristic blue quartz phenocrysts, Mount Adams Valley Mélange.

(f) Photomicrograph of (e).

(g) $F_6$ kink folds in mylonitised Mount Neill Granite Porphyry, Mount Adams Valley Mélange, same outcrop as (e) & (f).

(h) $F_6$ kink folds in the Mount Adams Quartzite (A1017-JPT018).

4a

b

c

d

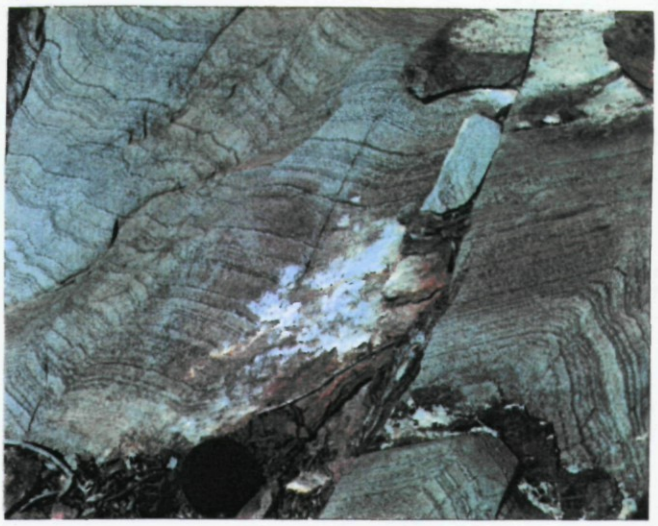

e

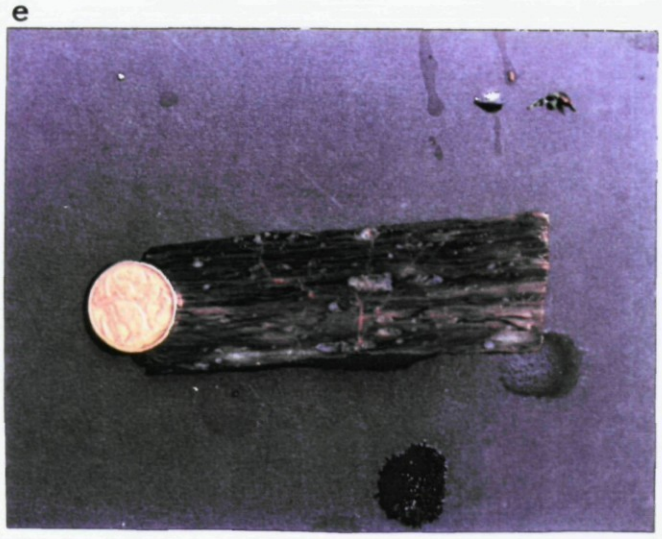

f

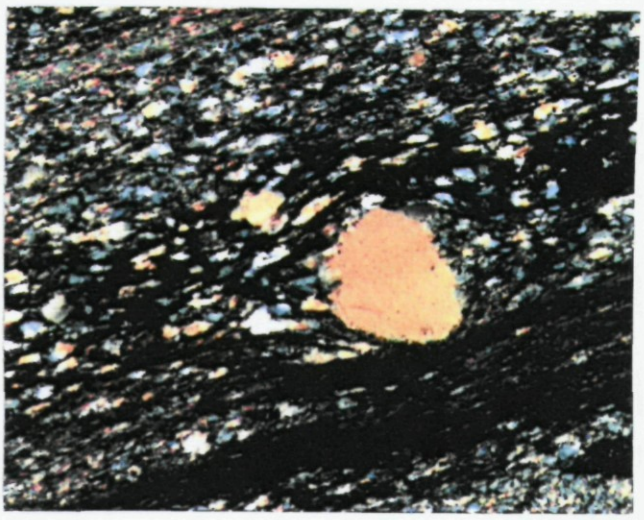

g

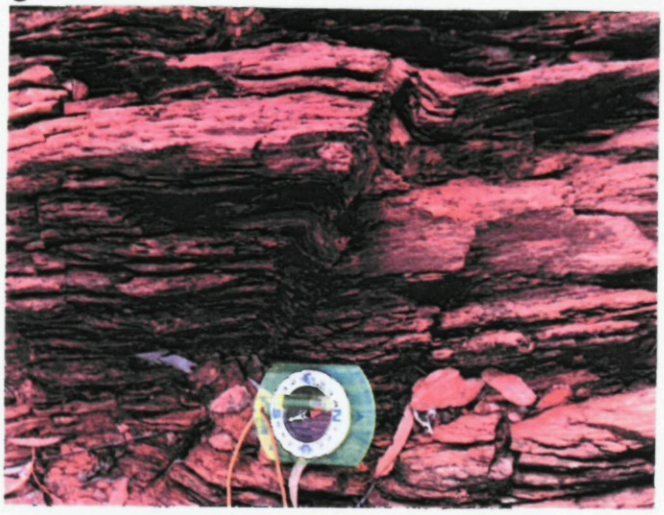

h

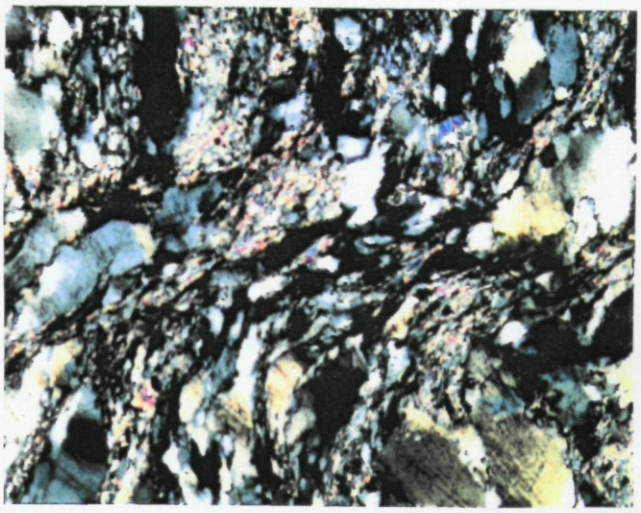

# Chapter 3

## Structural and metamorphic evolution

## 1 Introduction

In this chapter I outline the structural and metamorphic evolution of the Paralana Hot Springs - Mount Adams Valley area. An integrated discussion of these results is presented in Chapter 4.

In this chapter I abbreviate discrete deformation phases to $D_i$, planar features to $S_i$, folding events to $F_i$, metamorphic events to $M_i$ and linear features to $L_i$ (where *i* denotes the order of the event/feature).

| | | | | | |
|---|---|---|---|---|---|
| $D_1$ | $M_1$ | $S_1$ | - | $L_1$ | Gneissic foliation |
| $D_2$ | $M_2$ | $S_2$ | $F_2$ | $L_2$ | Tight isoclinal folding, upper amphibolite facies metamorphism, strong gneissic foliation, intersection lineation |
| $D_3$ | $M_3$ | $S_3$ | $F_3$ | $L_3$ | Open upright folding , low-mid amphibolite facies metamorphism |
| $D_4$ | - | - | $F_4$ | - | E-W trending crenulations |
| - | $M_4$ | - | - | - | Contact metamorphism caused by intrusion of Mt Neill Granite Porphyry |
| $D_5$ | - | $S_5$ | - | $L_5$ | Shearing and mylonitisation along Paralana Fault System |
| $D_6$ | - | $S_6$ | $F_6$ | $L_6$ | Kink folding of mylonites and sediments |
| - | $M_5$ | - | - | - | Regional retrogression of some high-T assemblages |
| $D_7$ | - | - | - | - | Exhumation via major thrusting |

Table 3.1 Summary of deformation and metamorphism.

# 2 Structural observations

Six ductile deformation phases have been recognised in the Paralana Hot Springs - Mount Adams Valley area. The seventh phase involved exhumation via thrust faulting. $D_1$ and $D_2$ are only seen in the Four Mile Creek Gneiss Suite, therefore predate other units. $D_3$ and $D_4$ effected the Four Mile Creek Gneisses, Freeling Heights Metasediments, Yagdlin Phyllite and Mount Adams Quartzite but predate $M_4$ metamorphism. $D_5$ and $D_6$ affected all previously mentioned units as well as the Mount Neill Granite Porphyry, but not the British Empire Granite. $D_7$ exhumation affected all mapped units except for recent alluvium.

## 2.1 $D_1$ and $D_2$

$D_1$ and $D_2$ are only seen in the Four Mile Creek Gneisses. $D_1$ is characterised by a layer parallel gneissic foliation, $S_1$ and abundant quartz veining (plate 4b). Fibrous acicular sillimanite on the leuco-melanocratic interfaces of the older paragneisses suggests the gneissic segregation ($S_1$) preceded peak metamorphism (plate 3a). A strong $L_1$ elongation lineation occurs in the older paragneiss sequence.

$D_2$ is characterised by tight isoclinal folding ($F_2$) of the entire Four Mile Gneiss Suite forming a pervasive layer-parallel axial planar foliation, $S_2$ (plate 4b). $S_2$ has largely overprinted $D_1$ structures. $F_1$ fold axes trend north-east and are doubly plunging due to later ?$F_4$ folding. Field recognition of $F_2$ hinges is difficult although the following may occur:

(i) partially transposed bedding;
(ii) axial planar foliation at some finite angle to bedding (even perpendicular);
(iii) migmatization and boudinage involving mica selvedges;
(iv) thick (≤2m) quartz veins;
(v) excessive anatexis;
(vi) a bedding-foliation intersection lineation, $L_2$.

Boudinage has occurred at all scales as a result of the high strain exploiting rheological inheterogeneities, especially in softer, micaceous units which accommodate much more strain than harder more competent units.

## 2.2 $D_3$

$D_3$ is characterised by the upright large scale open refolding ($F_3$) of the Four Mile Creek Gneisses, and upright tight folding in the Freeling Heights Metasediments, Yagdlin Phyllite and Mount Adams Quartzite (plate 4d). The $S_3$ axial planar foliation is weak in the gneisses, but strong in the metasediments especially in micaceous units. The intersection of $S_3$ with bedding defines the $L_3$ lineation. Boudinage associated with $D_3$ has exploited rheological weaknesses in micaceous units. $F_3$ fold axes generally trend north-east and follow the large scale sinusoidal warping of the entire Mount Painter Inlier and are doubly plunging due to $D_4$ north-south compression.

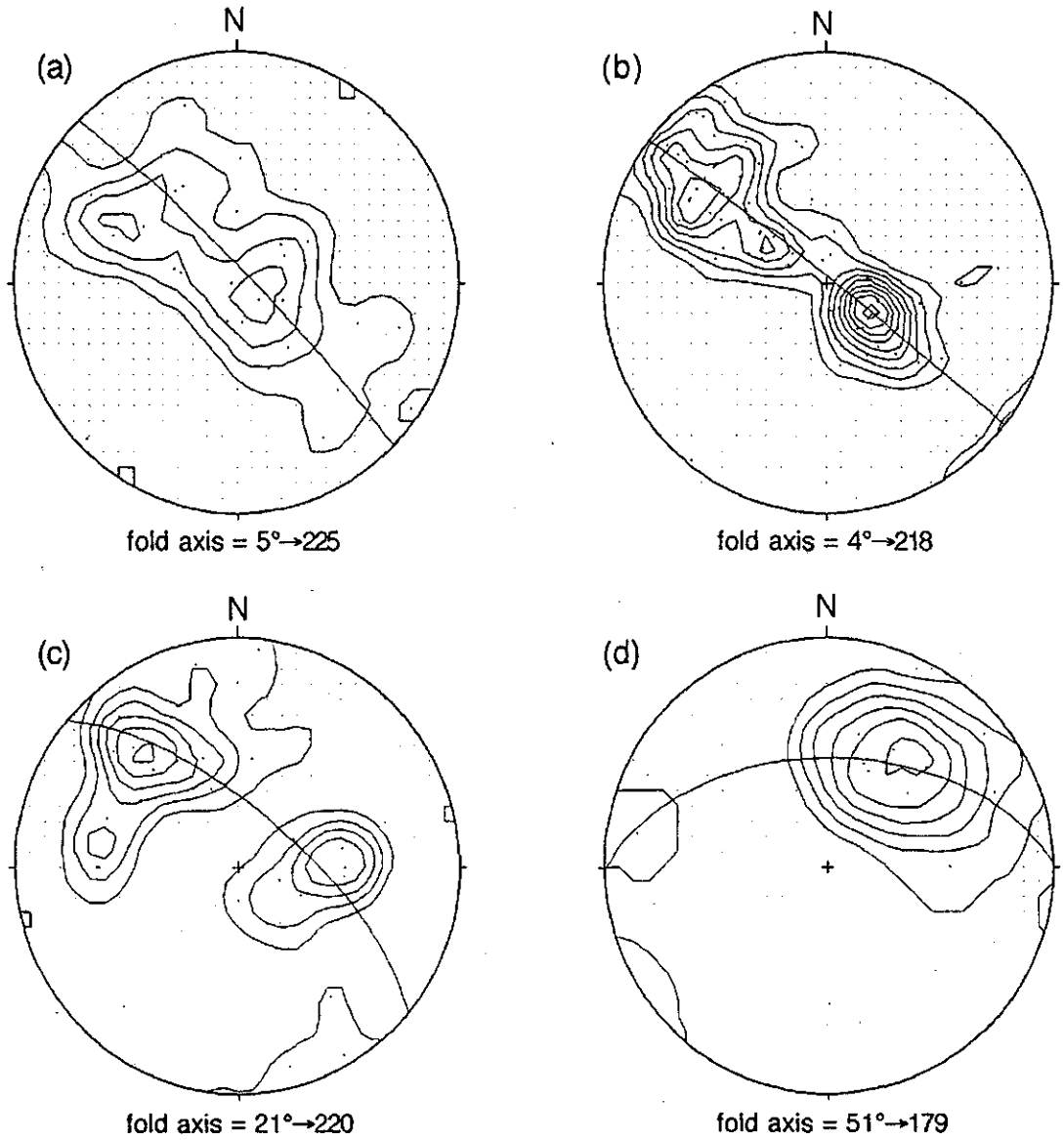


**Figure 5.1** Contoured, equal area stereographic projections showing $F_3$ fold axes for (a) the Yagdlin Phyllite and Mount Adams Quartzite {37 samples}, (b) the Four Mile Creek Gneiss Suite {102 samples}, and Freeling Heights Metasediments in (c) the north {42 samples}, and (d) the south {12 samples} of the mapped area.

### 2.3 $D_4$

$D_4$ is characterised by east-west trending crenulations ($F_4$) within micaceous units in the Four Mile Creek Gneisses and the Freeling Heights Metasediments (plate 4c). Warping of $F_3$ fold axes can also be attributed to $D_4$.

### 2.4 $D_5$

$D_5$ is represented by north-east trending mylonites associated with the Paralana Fault System forming an $S_5$ foliation (plate 4e,f,g). Mylonitisation of Mount Neill Granite Porphyry and various gneisses formed L-S tectonites with a strong, down-dip $L_5$ lineation oriented 40-70° to the north-west and west-side-up vergence. The $S_2$ foliation merges into this shear zone which forms the eastern edge of the Four Mile Creek Gneiss Suite (plate 1b). Strain partitioning in the Mount Neill Granite Porphyry causes localised north-east trending shearing in more micaceous units. Synchronous brittle deformation (faulting, shearing) throughout the area is also associated with $D_5$.

### 2.5 $D_6$

$D_6$ is characterised by chevron-style kink folding of $D_5$ mylonites, the Yagdlin Phyllite and the Mount Adams Quartzite (plate 4a,h). An $S_6$ kink band foliation can be seen in some outcrops.

## 3 Metamorphism

Five discrete phases of metamorphism have been recognised in the Paralana Hot Springs - Mount Adams Valley area. Peak metamorphism in the Four Mile Creek Gneisses occurred during $M_2$. High grade metamorphism of exotic rafts in Mount Adams Valley cannot be correlated with the five main phases and is discussed in §3.5.

### 3.1 $M_1$ and $M_2$

$M_1$ is inferred from the $D_1$ gneissic segregation of the Four Mile Creek

Gneisses and has been overprinted by peak $M_2$ metamorphism (plate 3a).

$M_2$ is characterised by the growth of fibrous sillimanite and K-feldspar parallel to the $S_2$ foliation in the paragneisses (plate 1a,b,c,d). Pelitic interbeds contain peak assemblages of biotite – quartz – ilmenite ± cordierite ± garnet and phlogopite ± corundum – quartz. Calc-silicate interbeds contain peak $M_2$ assemblages of (i) tremolite – anorthite – quartz – ilmenite grading up to clinopyroxene bearing units adjacent to the leucogneiss (plate 1g,h), and (ii) anorthite – Fe-garnet – epidote – sphene. A cordierite – orthoamphibole (– ilmenite – anorthite) rock (plate 1f) may represent a metamorphosed mafic volcanic or metasomatised pelitic sediments [Arnold & Sandiford, 1990; Yardley, 1991] . Aluminous layers containing sillimanite and tourmaline (plate 1c) also reflect $M_2$.

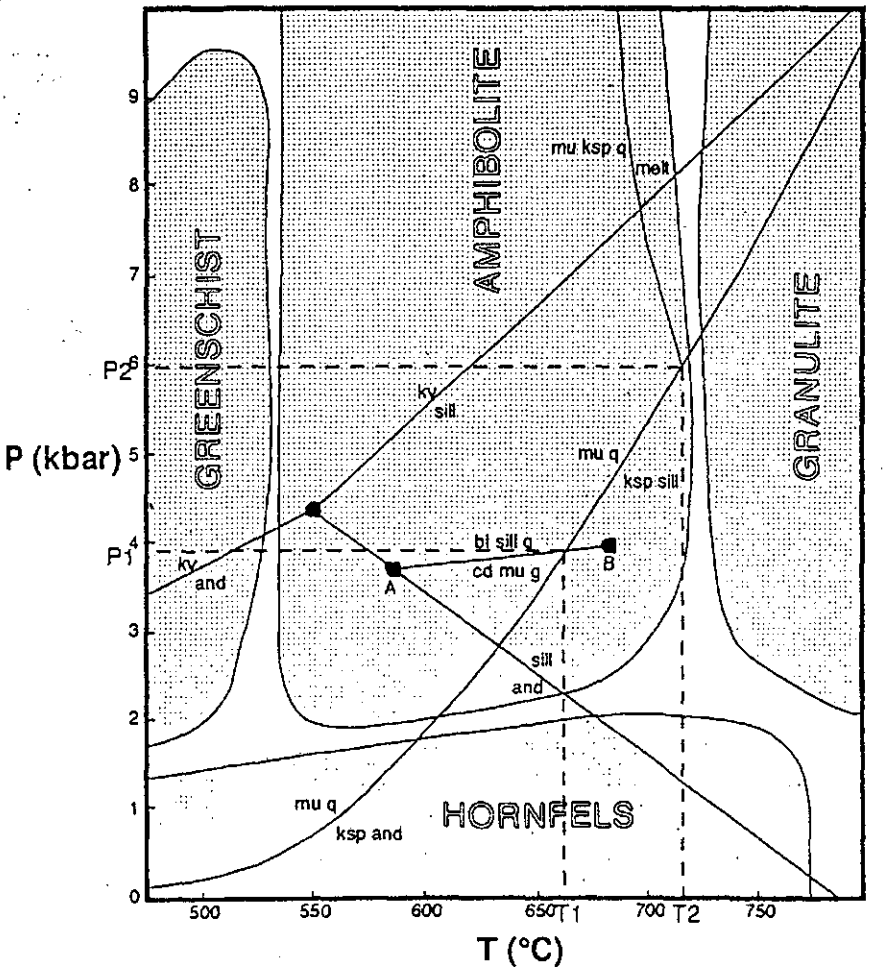


Figure 3.2 Petrogenetic grid for the system KFMASH + $H_2O$ as calculated by Xu et al. [1993] and Yardley [1991]. Pressure-temperature estimates of T1-T2 and P1-P2 were derived from this grid (see text). A and B represent the invariant points in the KFMASH system for biotite-cordierite-muscovite-garnet-staurolite-sillimanite-quart-fluid and biotite-cordierite-muscovite-Kfeldspar-sillimanite-quartz-fluid.

Pressure-Temperature conditions for the Four Mile Creek Gneisses of 665-720°C at 3.9-6.0 kilobars (upper amphibolite facies) were obtained from univariant reactions in the KFMASH system (see figure 3.2). Textural relationships for the reaction muscovite + quartz ↔ K-feldspar + sillimanite are well preserved (plate 1a), constraining PT conditions to the univariant curve shown in figure 3.2. The stability of the biotite – sillimanite – quartz – muscovite assemblage provides a minimum pressure constraint (plate 3b). The slight partial anatexis of the muscovite – K-feldspar – quartz assemblage in granite gneisses suggests temperatures in the upper limits of the specified range. Amphiboles are generally stable implying temperatures less than approximately 750°C, although the transition of cummingtonite to diopside adjacent to the leucogneiss may suggest localised granulite facies metamorphism (plate 1g,h).

## 3.2 $M_3$

$M_3$ is characterised by the primary metamorphism of the deforming Freeling Heights Metasediments, Yagdlin Phyllite and Mount Adams Quartzite, and retrograde metamorphism of the Four Mile Creek Gneisses. Pelitic interbeds in the Freeling Heights Metasediments show peak assemblages of biotite-muscovite ± cordierite ± garnet ± corundum (plate 2a). No sillimanite was found in quartz-muscovite bearing units. Relict andalusite porphyroblasts were found in a muscovite rich unit. $M_3$ metamorphism of the Yagdlin Phyllite was low grade and yielded biotite and manganese-rich garnet forming the axial planar foliation. In the Four Mile Creek Gneisses, $M_3$ retrogression of garnet to epidote, cordierite and corundum to quartz, and tourmaline to various micas occurred within the older paragneissic sequence. Further chloritisation of orthoamphibole in the cordierite-orthoamphibole bearing unit may also be attributed to $M_3$.

A mean temperature of 485°C was obtained for the Freeling Heights Metasediments using the garnet-biotite geothermometer of Holland & Powell [1990]. Relict andalusite constrains pressure to less than ~3.5 kilobars.

## 3.3 $M_4$

$M_4$ comprises a contact metamorphic aureole adjacent to the Mount Neill Granite Porphyry. $M_4$ is characterised by the growth of randomly oriented crystals of phlogopite, biotite, muscovite, prismatic sillimanite, corundum (sapphire), tourmaline, chlorite and cordierite in the Yagdlin Phyllite (plate 3e). Corundum – phlogopite growth in the Freeling Heights Metasediments can be attributed to $M_4$ although subsequent structural juxtaposition with the Mount Neill Granite Porphyry must be considered.

Hence contact metamorphism/metasomatism was of upper hornfels facies with temperatures greater than 550°C causing sillimanite growth. The high alumina content of contact metamorphosed phyllites is due to either (1) silica-undersaturated magmatic fluids causing leeching of silica (i.e. contact metasomatism), or (2) contact metamorphism of highly aluminous sediments (possibly laterites since intrusion was very shallow - sub-aerial).

## 3.4 $M_5$

$M_5$ was a retrograde event which is characterised by the breakdown of cordierite and andalusite to quartz ± mica in the Freeling Heights Metasediments and the Yagdlin Phyllite. Chloritisation and sericitisation associated with fault activity may also be attributed to $M_5$. The prograde formation of clinopyroxene from tremolite adjacent to an undeformed granite within the paragneiss sequence could also be caused by $M_5$.

## 3.5 Metamorphism of Mount Adams Valley rafts

### 3.5.1 Calc-silicates

Wollastonite-bearing calc-silicates suggest a temperature window of ~600-700°C (plate 3c,d), although the $X_{CO2}$ is unconstrained due to the isolated structural setting of these units. The absence of amphiboles supports this temperature constraint.

### 3.5.2 Mafic granulites

Two-pyroxene (enstatite-augite) granulites (plate 2b) yielded a peak temperature of 856°C using the clinopyroxene – orthopyroxene geothermometer of Wells [1977] (see Appendix 5). Clinopyroxene – spinel

symplectites growing from forsterite and anorthite in an olivine – plagioclase – kaersutite (high grade amphibole) gabbro (plate 2c,d) indicate a minimum pressure of 8.5kb* [Green & Hibberson, 1970].

# 4 $D_7$ Faulting

The Lady Buxton Fault# forms major north-east trending thrust fault which dissects the Paralana - Mount Adams Valley area. It dips west at 30-70° and shows evidence for west-side-up brittle thrusting ($D_7$) which has partially reactivated and brecciated $D_6$ mylonites. The Lady Buxton Fault forms the western edge of Mount Adams Valley and the eastern edge of the Four Mile Creek Gneiss Suite. Anastomosing splinter faults associated with the Paralana Fault System further dissect the area. The eastern edge of Mount Adams Valley is defined by a shallow (~30°) west dipping fault; the Mount Adams Fault. The vergence of this fault is unknown but may be normal (see Appendix 5 - Block Diagram).

Hematite- and copper-bearing breccias occur along $D_7$ faults throughout the area, indicating significant fluid flow. Intense drag folding of low grade (Tertiary, Mesozoic) sediments along the eastern edge of the range can also be attributed to $D_7$. The similarity of these deformed sediments with the Mount Adams Valley Mélange must be considered.

* Experimental data shows that the forsterite - anorthite assemblage is stable up to 9.9kb at 1250°C under isothermal compression, before yielding pyroxenes + spinel, while garnets are produced at 14kb [Green & Hibberson, 1970]. Sandiford [pers. comm., 1993] suggests the observed reaction textures are due to the instability of olivine and anorthite in a crystallising (sub-solidus) mafic magma at high pressure.

# The Lady Buxton Fault forms the northerly extension of the Paralana Fault System [Coats & Blissett, 1971].

# Chapter 4

## Tectonic evolution of the Paralana Hot Springs - Mount Adams Valley area

## 1 Introduction

Correlation of geochronological data [Schaefer, 1993; Teale, 1993; in press; Sheard pers. comm., 1993] with observed lithologies, structures and metamorphic assemblages indicates at least three orogenic events have affected the Mount Painter Inlier. This contrasts with the previous assumption that the structural and metamorphic evolution of the Mount Painter Inlier was only due to the lower Palaeozoic Delamerian Orogeny [Coats & Blissett, 1971]. A major finding of this study is the recognition of a stratigraphic break between the Four Mile Creek Gneiss Suite and the Freeling Heights Metasediments (see Chapter 2, §3), implying at least two tectonothermal events prior to the emplacement of the Mount Neill Granite Porphyry and Adelaidean sedimentation.

Schaefer [1993] proposes a major episode of Palaeoproterozoic crustal growth for the Mount Painter Inlier and suggests that peak deformation and metamorphism in the Four Mile Creek Gneiss Suite also occurred during the Palaeoproterozoic. Deformation and metamorphism of the Freeling Heights Metasediments, Yagdlin Phyllite and Mount Adams Quartzite, and synchronous refolding and retrograde metamorphism of the Four Mile Creek Gneisses can be attributed to a Mesoproterozoic* orogenic event.

The post-Proterozoic evolution of the Paralana Hot Springs - Mount Adams Valley area emphasises the ongoing role of the Paralana Fault System in controlling sedimentation, exhumation, fluid flow and deformation. Active seismicity and hydrothermal activity associated with the Paralana Hot Springs indicates the current active state of this system [Sprigg pers. comm., 1993]. I interpret the Delamerian overprint to be minimal and isolated to

* Since the Mount Neill Granite Porphyry is relatively undeformed, deformation of adjacent units must predate its intrusion (dated at 1565±4Ma).

major compressional shearing along the Paralana Fault System and retrograde metamorphism. Major exhumation via thrusting occurred during the Tertiary [Coats & Blissett, 1971].

In this chapter I discuss Proterozoic and post-Proterozoic tectonism separately and outline possible regional correlations with other Australian Proterozoic orogens.

## 2 Proterozoic tectonic history

Schaefer [1993] has identified a period of major crustal growth between approximately 2.4 and 2.0Ga* from the Four Mile Creek orthogneisses, and suggests the Four Mile Creek paragneisses were sourced from these orthogneisses prior to deformation. The notion of a major Palaeoproterozoic orogeny is supported in part by the Rb/Sr resetting age of 1700Ma obtained for the Four Mile Creek Gneiss Suite [Schaefer, 1993]. The first two deformation events, $D_1$ and $D_2$ are attributed to a Palaeoproterozoic orogeny since formation of the gneissic foliation, isoclinal folding and upper amphibolite facies metamorphism are not seen in younger units. $M_1$ and $M_2$ low-pressure–high-temperature metamorphism generally predates orthogneiss intrusion and is synchronous with $D_1$ and $D_2$ deformation. Sandiford [1989a] interprets such recumbent structures in high-temperature metamorphic belts as due to the extensional collapse of overthickened crust.

The resetting age of 1700Ma may actually date crustal extension preceding deposition of the Freeling Heights Metasediments (see below). Hence Palaeoproterozoic tectonism may be correlated with the Nullaginian event recognised in many other Australian Proterozoic orogens around 1.8-1.9Ga (see §3) [Etheridge et al., 1987].

Deformation and mid-amphibolite facies metamorphism of the Freeling Heights Metasediments, Yagdlin Phyllite and Mount Adams Quartzite preceded the intrusion of the Mount Neill Granite Porphyry around 1565Ma. Deposition of the Freeling Heights Metasediments after deformation of the Four Mile Creek Gneisses (~1700Ma) further constrains this Mesoproterozoic event which may correlate with Carpentarian tectonism recognised in many

* A Sm/Nd depleted mantle model age [Schaefer, 1993].

other Australian orogens around 1600Ma [Etheridge et al., 1987].

The Four Mile Creek Gneisses are refolded about an axis perpendicular to $D_1$ and $D_2$ structures. Hence those structures must have been sub-horizontal prior to Mesoproterozoic $F_2$ folding. Two different mechanisms may explain this; (1) $F_2$ isoclinal folds and the $S_2$ foliation formed horizontally due to extension [e.g. Sandiford, 1989a], and (2) $F_2$ isoclinal folds and the $S_2$ foliation were compressional and underwent later extension via simple shear, which rotated them into sub-horizontality. The second mechanism is favoured here since extension must have preceded deposition of the Freeling Heights Metasediments. Hence the resetting age of ~1700Ma for the Four Mile Creek Gneisses may be a manifestation of this extension.

The growth of corundum (sapphire) and other aluminous minerals in mica rich beds of the Freeling Heights Metasediments and the Yagdlin Phyllite occurred as a result of granite emplacement and may represent sub-surface contact metamorphism of laterite horizons due to their anomalous alumina content. The non-aligned nature of metamorphic minerals on the contact aureole suggests $M_3$ metamorphism post-dated all deformation in the Freeling Heights Metasediments and Yagdlin Phyllite, questioning the role of Delamerian deformation in the evolution of the Mount Painter basement (see Chapter 4).

# 3 Proterozoic tectonism in Australia

Two essentially isochronous tectonothermal events have been recognised in the northern Australian Palaeo-Mesoproterozoic record (see figure 5.1) which are characterised by orogenesis of the Nullaginian (Barramundi Orogeny) around 1900-1830Ma and Carpentarian basinal sedimentary cycles around 1600-1500Ma [Etheridge et al., 1987]. The Nullaginian sedimentary cycle in the Hall's Creek and Pine Creek domains corresponds to rift and sag phase clastic sequences followed by a turbiditic ?flysch facies which may have been syn-orogenic [Etheridge et al., 1987]. Subsequent Carpentarian sedimentation and tectonic style seems to vary between terrains [Etheridge et al., 1987]. Other domains in which the Nullaginian and Carpentarian have been recognised include the Arunta Block, the Mount Isa Block, the King Leopold Block and (at least in part) the Gawler Block. Two major Proterozoic

tectonothermal events observed in the Mount Painter Inlier can be related to Nullaginian and Carpentarian tectonism.

Major igneous rock associations correlate remarkably well between domains and show extensive geochemical homogeneity, requiring a widespread homogeneous source[#]; a fact that cannot be easily reconciled with subduction complexes. Syn-sedimentary mafic magmatism is correlated with rifting (as in modern terrains). The geochemistry of syn- and post-orogenic I- and A-type felsic plutonism cannot be associated with modern subduction complexes due to the lack of intermediate-mafic components, the narrow spread of chemical components between and within domains and the high levels of potassium and light rare earth elements [Wyborn, 1985; Etheridge et al., 1987]. Schaefer [1993] has correlated igneous rock associations of the Mount Painter Inlier with geochemical data from other Australian Proterozoic orogens.

Low-pressure–high-temperature (andalusite-sillimanite) metamorphism distinguishes northern Australian Proterozoic terrains from modern collisional orogens. The metamorphic record shows evidence for isobaric cooling rather than adiabatic decompression. [Etheridge et al., 1987; Sandiford, 1989b; Loosveld & Etheridge, 1990]. Upper amphibolite facies metamorphism in the Palaeoproterozoic of the Mount Painter Inlier is consistent with these notions.

The Proterozoic tectonic evolution of the Mount Painter Inlier cannot be correlated with a convergent plate boundary, as illustrated by its present intracratonic setting. Low-pressure metamorphism, 'ensialic' magmatism [Schaefer, 1993] and the absence of oceanic crustal material indicates an alternative tectonic setting. Alternative tectonic scenarios are discussed in Part 2 of this thesis.

# 4 Post-Proterozoic tectonism

The western edge of the Mount Neill Granite Porphyry is defined by a west-dipping mylonite zone with reverse sense possibly indicating Delamerian

[#] This widespread homogeneous source may have accreted by ?plume related underplating at about 2000Ma. Little evidence for recycling of preexisting Archaean crust into the source or the magmas exists. Similar processes have been documented in Scotland, Greenland and Antarctica [Etheridge et al., 1987].

activity ($D_5$) along the Paralana Fault. Lineations trending 70-80°→325 on northeast trending foliations were recorded at the entrance to Mylonite Creek, and kinematic indicators showed a west-side-up reverse vergence. Large outcrops of mylonite at the northern end of Mount Adams Valley showed the same vergence on a similar lineation (40°→300).

Subsequent chevron style, small scale kink folding ($F_4$) of these sediments may also be attributed to $D_5$ Delamerian deformation. The Yagdlin Phyllite and Mount Adams Quartzite also experienced $F_4$, and an $S_5$ kink band foliation may be defined.

An $M_4$ metamorphic event caused retrogression of cordierite and sillimanite in the Yagdlin Phyllite, although the timing of $M_4$ is uncertain and may be related to similar post-Delamerian retrograde metamorphism in Adelaidean sediments further south.

# 5 Tectonic significance of Mount Adams Valley

Major brittle thrusting along the Paralana Fault System is attributed to late-Tertiary exhumation of the Flinders Ranges due to drag folding of Tertiary and Mesozoic sediments along the edge of the range in the south of the area*.

The Mount Adams Valley Fill is interpreted as a post-Delamerian tectonic mélange. Major Tertiary overthrusting may explain many unusual features of Mount Adams Valley. Valley floor sediments may be as young as Tertiary, possibly flysch conglomerates, although Teale [pers. comm., 1993] suggested a pyroclastic diatreme-volcanogenic (possibly carbonatitic) origin. Palynological analysis was negative [SANTOS, 1993], however XRD analysis of small prismatic tourmaline crystals supports a sedimentary origin [Foden pers. comm., 1993]. Various exotic lithologies occurring as rafts in Mount Adams Valley may have been emplaced via thrusting. Rafts of undeformed sediment may be exhumed Adelaidean Wywyana formation#.

The low angle fault bounding the eastern edge of Mount Adams Valley may

* Vertically dipping tertiary conglomerates were found near the entrance to Four Mile Creek.
# Adelaidean sediments east of the Paralana Fault System are flat lying and undeformed [Coats & Blissett, 1971; SADME drilling data]. Tertiary thrusting may have sampled these sediments forming rafts in Mount Adams Valley.

in fact be extensional due to gravitational collapse of the major overthrust [Sears pers. comm., 1993], forming an olistostrome [e.g. Hobbs et al., 1978; Elter & Trevisan, 1973; Kovács, 1989]. This would explain the lack of brecciation along the eastern fault, its inconsistent orientation and discontinuity (see figure 1.2) and implies that the mapped portion of the Mount Neill Granite Porphyry, Yagdlin Phyllite and Mount Adams Quartzite was originally west of the Paralana Fault System. The lack of ductile deformation in the Mount Neill Granite Porphyry is attributed to its shallow emplacement in this area (i.e. above the brittle - ductile transition depth (<15km)).

I suggest that the Mount Painter Inlier is, at least in part, allochthonous. Major Tertiary thrusting emplaced the Mount Painter allochthon. The presence of 'tillites' near Mount Gee, to the south [Sprigg pers. comm., 1993], and other mélanges of socalled Wywyana Formation can be explained in this way. The Mount Painter Inlier forms a gravity 'low'* which suggests that basement rocks overlie less dense material, probably younger sediments.

* Average Bouger gravity readings 20-30 milligal lower than average for the Adelaidean parts of the northern Flinders Ranges cannot be reconciled with dense Precambrian crystalline basement.

# PART TWO

## Tectonics of Proterozoic Orogenic Belts

# Chapter 5

## Orogenic aspects of Proterozoic tectonics

### 1 Introduction

Plate Tectonic theory has dominated geological thinking since its inception in the 1960's [e.g. Condie, 1989], because it offers a powerful framework for understanding the behaviour of the modern earth. This model adequately accounts for many modern (Palaeozoic) tectonic regimes but problems have arisen regarding its application to some Precambrian terrains. This suggests that important secular tectonic changes may have occurred [e.g. Kröner, 1981; 1983; Sandiford, 1989b; Loosveld & Etheridge, 1990] so that many plate tectonic models proposed for such terrains may be inappropriate. The importance of such secular changes is subject to debate. Some workers assume that modern plate tectonic systems have been operating since the earliest crustal formation (uniformitarianism) [e.g. Glikson, 1981; Anderson & Burke, 1983; Hoffman, 1990], while others invoke alternative mechanisms to explain progressive tectonic change since the Archaean [e.g. Etheridge et al., 1987; Ellis, 1992].

One of these potentially important secular changes relates to the thermal evolution of the earth. Since the tectonic behaviour of the lithosphere strongly reflects its thermal state, its thermal evolution may have caused secular changes in tectonic style. Most workers recognise that Archaean (>2.5Ga) tectonic processes reflected a 200-300°C higher mean mantle temperature, resulting in greater convective vigour in the mantle and the proliferation of high-temperature rock types such as komatiites [e.g. Bickle, 1978; McKenzie & Weiss, 1980; Glikson, 1981; Baer, 1983; Christensen, 1985]. In comparison the earth's subsequent cooling history and its impact on tectonic style, especially during the Proterozoic, is much more contentious.

According to plate tectonic theory, convergent deformation and orogenesis is restricted to collisional plate boundaries*. Modern (Palaeozoic) orogens are characterised by major uplift, high-pressure metamorphic belts, calc-alkaline magmatism (andesites), lateral crustal accretion via large scale nappe structures, and obducted oceanic crust (ophiolites) [e.g. Hargraves, 1981; Baer, 1983; Etheridge et al., 1987]. While successful interpretations of some Proterozoic orogens have been made using 'classical' plate tectonic theory [e.g. Anderson & Burke, 1983; Windley, 1981; 1983; Hoffman, 1980; 1990], the distinct absence of 'modern' signatures from many Proterozoic mobile belts may indicate secular tectonic change [e.g. Tarling, 1980]. Ensialic (intracontinental) orogeny has been suggested as an alternative model for orogenesis and crustal growth in the Proterozoic [e.g. Kröner, 1977, 1981, 1983; Etheridge et al., 1987; Loosveld & Etheridge, 1990] and may explain many unusual features including the abundance of high-temperature–low-pressure metamorphism and anorogenic granites. The sialic nature of the underlying crust and palaeomagnetic data# further support this idea.

The abundance of high-temperature–low-pressure metamorphic belts in the Proterozoic record suggest anomalous geothermal gradients and only limited crustal thickening [e.g. Newton, 1987]. Some workers have attempted to explain this in terms of extension [e.g. Sandiford & Powell, 1986], but field evidence generally supports contemporaneous metamorphism and compression [Loosveld & Etheridge, 1990; Sandiford & Powell, 1991]. Metamorphic evidence suggests isobaric cooling (rather than adiabatic decompression) occurred, indicating limited crustal thickening† [e.g. Loosveld & Etheridge, 1990; Sandiford & Powell, 1991].

The behaviour of the mantle lithosphere during convergent deformation is critical to the evolution of an orogen [Houseman et al., 1981]. Several workers have shown that a prerequisite for high-temperature–low-pressure metamorphism is the decoupling of strain between the crust and mantle lithosphere, involving simultaneous crustal thickening and mantle

* Both oceanic and continental plates are currently too rigid to deform internally at feasible driving forces and geothermal gradients, although the continental crust is weaker than the oceanic crust.
# Palaeomagnetic evidence for the Proterozoic suggests the existence of several huge continents whose relative movement was minimal; hence plate boundary collisional orogeny was unlikely and cannot be reconciled with the large number of Proterozoic mobile belts [McElhinny & Embleton, 1976; Hargraves, 1981; Piper, 1991].
† Isobaric cooling indicates negligible post-orogenic uplift via erosion or mountain collapse. Hence convergent deformation did not involve substantial crustal thickening.

lithospheric thinning [Loosveld & Etheridge, 1990; Sandiford & Powell, 1991]. The gravitational instability of a thickened thermal boundary layer at the base of the lithosphere may lead to its detachment; removing part or all of the mantle lithosphere via delamination or some other means [Bird & Baumgardner, 1981; Houseman et al., 1981]. A discussion of possible scenarios for lithosphere delamination and ensialic orogenesis is presented in §2 of this chapter.

While such tectonic scenarios provide intriguing insights into lithospheric evolution, their plausibility and implications have not yet been quantitatively evaluated. In Chapter 6 I outline methods and results employed in my numerical evaluation of possible delamination scenarios. Application of such models to the Proterozoic tectonic record of the Mount Painter Inlier and other Australian orogens is discussed in Chapter 7.

## 2 Delamination mechanics

Lithospheric thinning via mantle lithosphere delamination will involve the rise of hot asthenospheric material (see figure 5.1). Therefore thinning will act (1) to heat the remaining lithosphere, hence weakening it, and (2) to increase its buoyancy. The buoyancy increase will raise the potential energy and elevation of the lithosphere. Gravity will act against these increases, resulting in an extensional force known as the *buoyancy force*.

Lithospheric stability will be maintained if the tectonic driving force *balances* the buoyancy force and the lithospheric strength. If the buoyancy force exceeds the driving force and strength at a given rate, extension will ensue (and vice versa). Hence the mechanical consequences of mantle lithosphere delamination can be investigated by evaluating a simple force balance. A numerical method for achieving this is presented in Chapter 6.

Three basic scenarios involving mantle lithosphere delamination have been developed by different workers to explain the aforementioned features of Proterozoic orogens (see figure 5.2):

(i) Scenario 1: Mantle lithosphere delamination may precede and localise convergent deformation in intracratonic settings. Deformation is

attributed to large scale tectonic driving forces acting on the continental lithosphere [e.g. Loosveld & Etheridge, 1990; Sandiford pers. comm., 1993].

(ii) **Scenario 2**: Mantle lithosphere delamination may occur in response to thermally induced boundary layer instabilities caused by extension [e.g. Kröner 1981; 1983]. Here convergent deformation is caused by the 'slab pull' force of the delaminating lithosphere [e.g. Kröner, 1981; 1983; 1984; Etheridge et al., 1987]. This scenario suggests ensialic orogenesis is self-perpetuating and self-localising .

Workers at the Bureau of Mineral Resources have developed a 'Scenario 2' model for ensialic orogenesis in Australia during the Proterozoic (see figure 5.2). Nullaginian and Carpentarian sedimentation was caused by limited stretching of Archaean continental lithosphere over relatively small polygon-shaped convection cells* in the upper mantle around 2.0-1.87Ga [Kröner et al., 1985; Etheridge et al., 1987]. Massive magmatic underplating accompanied this stretching. Lithospheric delamination ensued, causing convergent deformation via 'slab pull', acting only to restore normal crustal thickness. Note that the difference between this scenario and 'plate tectonic' models (e.g. North America) is 'one of degree rather than kind'. In this case, continental extension did not proceed to the stage of sea-floor spreading, hence subduction did not involve oceanic lithosphere. Orogenesis acted only to restore normal crustal thickness, thus explaining the widespread low-pressure metamorphism in many Proterozoic terrains. [Etheridge et al., 1987]

(iii) **Scenario 3**: Mantle lithosphere delamination may occur in response to boundary layer instabilities caused by lithospheric thickening [Houseman et al., 1981; Sandiford, 1989b; Loosveld & Etheridge, 1990; Sandiford & Powell, 1991]. Here, delamination occurs as a *response* to thickening and may cause extensional collapse [Sandiford, 1989b].

* This turbulent small scale convection is thought to have been caused by the blanketing effect of a very large slow moving continental mass; a notion supported by palaeomagnetic data [Etheridge et al., 1987; Piper, 1991].

**Figure 5.2** Schematic representation of the three delamination scenarios.

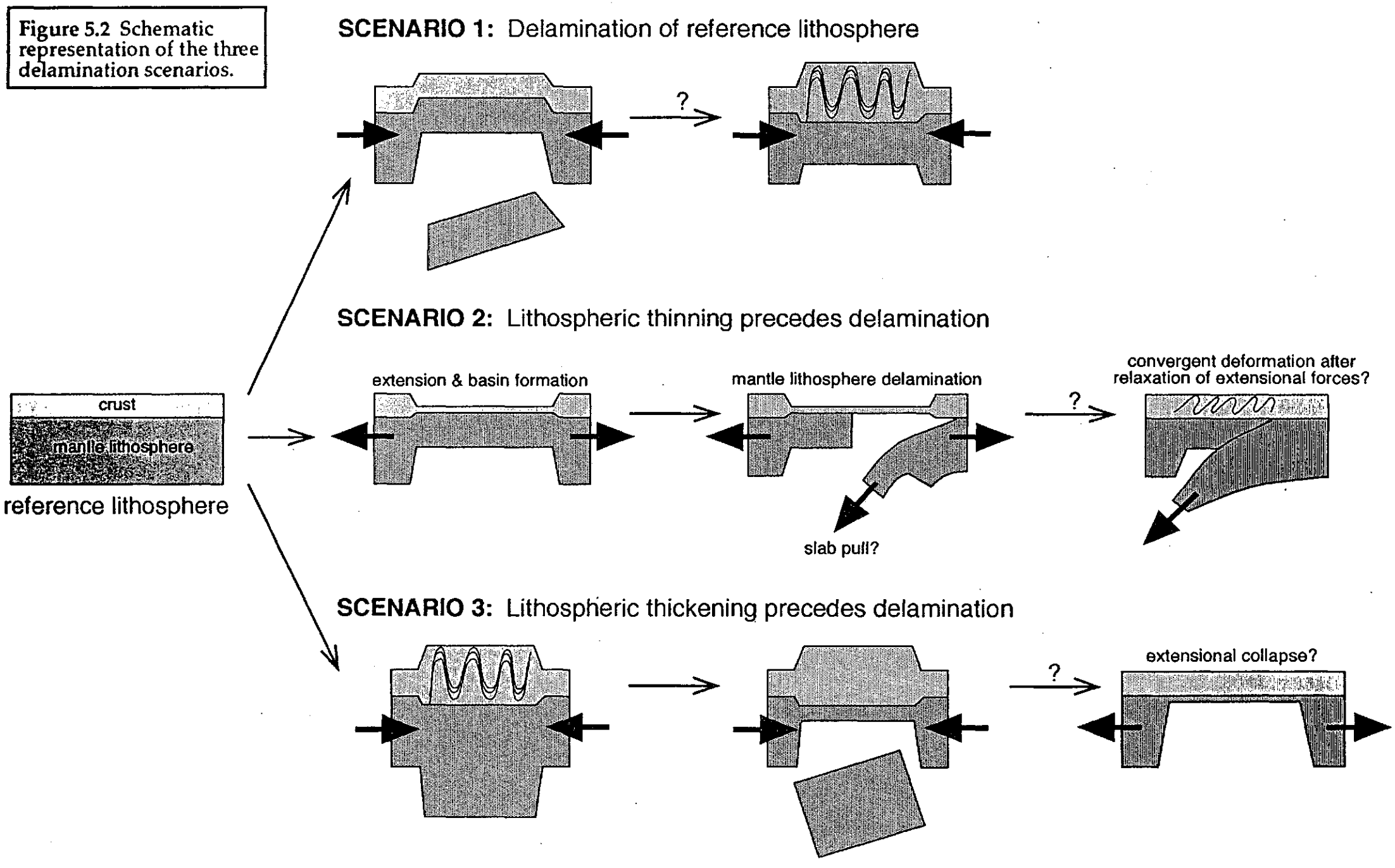

# Chapter 6

## On the mechanical plausibility of ensialic orogenesis

## 1 Introduction

In this chapter I investigate the mechanical plausibility and consequences of mantle lithosphere delamination. This method derives its inspiration from the work of Turcotte & Schubert [1983], Sonder & England [1986] and Zhou & Sandiford [1992].

## 2 The numerical model

The lithospheric response to deformation at long wavelengths may be approximated by using a thin sheet model [e.g. Sonder & England, 1986] which assumes horizontal and vertical strain rates are independent of depth. These simple models have proved remarkably successful in explaining many lithosphere-scale phenomena for horizontal length scales greater than 100km [Sonder & England, 1986]. In this case I consider the effects of thermally induced mechanical changes on a 1-dimensional lithospheric column* (see figure 6.1).

The mechanical plausibility of delamination may be tested by evaluating the force balance on such a lithospheric column (see Chapter 5). The force balance expresses the relationship between the tectonic driving force, $F_d$, the horizontal buoyancy force resulting from potential energy changes caused by deformation, $F_b$, and the lithospheric strength, $F_l$, which is dependent on thermal state and based on a vertically averaged rheology appropriate to a thin viscous sheet [Sonder & England, 1986].

Consider an undeformed lithospheric column subjected to a far-field tectonic driving force, $F_d$, assumed insufficient to deform it at appreciable rates. The

* Since the length scales for convergent deformation greatly exceed the depth, it is reasonable to consider changes in the vertical dimension as a first approximation.

column has strength $F_l$, and density $\rho_z$, which varies with depth.

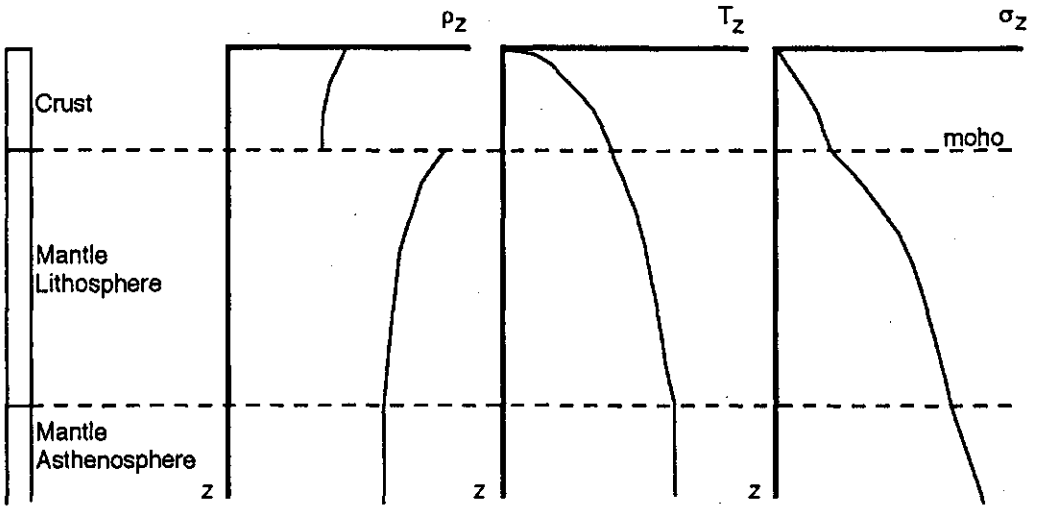


**Figure 6.1** Undeformed lithospheric column with density distribution ($\rho_z$), temperature and vertical stress($\sigma_z$) versus depth graphs.

Now consider this column if part or all of the mantle lithosphere is removed.

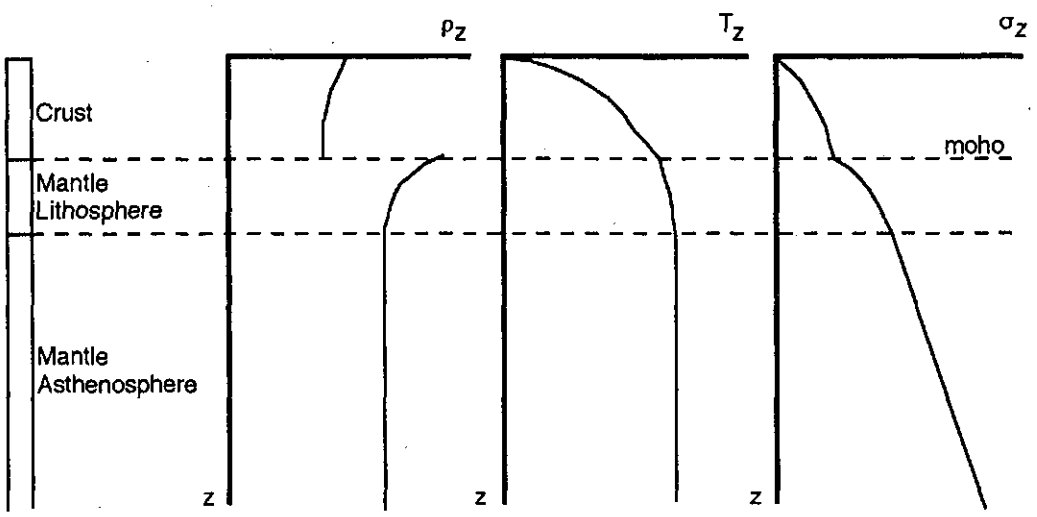


**Figure 6.2** Deformed lithospheric column with attenuated mantle lithosphere.

For deformation of this column, the driving force must exceed the combined buoyancy force and strength for a given strain rate, i.e:

$$F_d > F_b + F_l \tag{6.1}$$

The effects of lithospheric thinning (via delamination) on the force balance are evaluated by delaminating a portion of the mantle lithosphere of thickness $z_{delam}$. This is expressed numerically as a thinning factor, $\beta$:

$$\beta = \frac{z_{l_0}}{z_{l_0} - z_{delam}} \tag{6.2}$$

where $z_{l0}$ is the initial thickness of the lithosphere. Note that $\beta$ is the reciprocal of the thickening factor defined by Sandiford & Powell [1991]. Assuming the potential thermal state (see below), a unique force balance is defined for a given thinning factor and strain rate.

Parameters used in all calculations are listed in table 6.1. Initial boundary conditions appropriate to the three delamination scenarios discussed in Chapter 5 were implemented. A fourth set of boundary conditions appropriate to a thinner, 'hotter' Proterozoic lithosphere were also used. Boundary conditions used are listed below:

(i) a reference lithosphere, with mean crustal and lithospheric thicknesses of 35km and 125km (Scenario 1);
(ii) the reference configuration thinned by a factor of 2 (i.e. $f_l$=0.5; Scenario 2);
(iii) the reference configuration thickened by a factor of 1.5 (Scenario 3);
(iv) a thinner lithosphere corresponding to higher geothermal gradients (hotter mantle temperatures) suggested for the Proterozoic. Reference crustal and lithospheric thicknesses used were 25km and 80km [Zhou pers. comm., 1993].

## 2.1 Calculation of the force balance for given strain rates

### 2.1.1 Horizontal buoyancy force

The horizontal buoyancy force is caused by the change in potential energy between the deformed and undeformed lithosphere. The potential energy of a lithospheric column is given by:

$$E_p = \int_h^{z_l+h} \sigma_{zz}(z)dz = g\iint_{z_l} \rho(\tau)d\tau dz \tag{6.3}$$

where $\sigma_{zz}(z)$ is the vertical stress at depth $z$, $z_l$ is the thickness of the lithosphere, $h$ is the change in elevation (negative since depth is positive), $g$ is gravitational acceleration and $\rho(\tau)$ is the lithospheric density (which is a function of depth). So the buoyancy force per unit length (of orogen), $F_b$ is given by:

$$F_b = E_{p(delaminated)} - E_{p(reference)} - E_{p(excess)} \quad (6.4)$$

where $E_{p(delaminated)}$ is the potential energy of the thinned (delaminated) column, $E_{p(reference)}$ is the potential energy of the reference (undeformed) column and $E_{p(excess)}$ is the potential energy gain due to the absence of lithospheric material between the base of the delaminated column and the depth of isostatic compensation (taken to be the base of the reference lithosphere).

The density structure of the lithosphere is given by (see figure 6.1):

$$\text{crust: } \rho(z) = \rho_c + \rho_c \alpha_c (T_l - T(z)) \quad (6.5)$$

$$\text{mantle lithosphere: } \rho(z) = \rho_l + \rho_l \alpha_m (T_l - T(z)) \quad (6.6)$$

[Turcotte, 1983]

where $\rho_c$ and $\rho_m$ are the densities of the crust and mantle at temperature $T_l$, which is the temperature at the base of the lithosphere of thickness $z_l$, $\alpha$ is the coefficient of thermal expansion and $T(z)$ is the temperature at depth $z$. The simplification $\alpha_c \rho_c = \alpha_m \rho_m$ is assumed [Turcotte, 1983; Sandiford & Powell, 1990; Zhou and Sandiford, 1992].

Buoyancy force estimates are strongly dependent on the geothermal gradient, with differences of up to $8 \times 10^{12}$ $Nm^{-1}$ occurring between 'no internal heat production' gradients and the exponential gradients used here [Zhou & Sandiford, 1992]. Zhou & Sandiford [1992] have shown that numerical values for the buoyancy force are especially sensitive to the value of the thermal expansion coefficient.

The horizontal buoyancy force is proportional to the thinning factor, $\beta$ (see figure 6.3). Any attenuation of the mantle lithosphere results in potential energy increases giving extensional buoyancy forces (see figures 6.3). If the lithosphere is thickened prior to delamination, it will have a positive initial buoyancy force of $2 \times 10^{12}$ $Nm^{-1}$ and an elevation of 2km with respect to an isostatically compensated reference lithosphere [Zhou & Sandiford, 1992]. If the lithosphere is thinned prior to delamination it will have a negative initial buoyancy force of $-0.5 \times 10^{12}$ $Nm^{-1}$ and an elevation of -1500m. A maximum buoyancy forces of $8 \times 10^{12}$ $Nm^{-1}$ occurs when the entire mantle lithosphere is removed from an initially thickened crust (see figure 6.3).

## Table 6.1 Parameter values

| | | | |
|---|---|---|---|
| $A_p$ | preexponential constant for | (i) quartz<br>(ii) olivine | $5 \times 10^{-6}$ MPa$^{-3}$s$^{-1}$<br>$7 \times 10^{4}$ MPa$^{-3}$s$^{-1}$ |
| $b$ | vertical length of descending slab | | ≈100km |
| $D_0$ | length scale for heat source distribution | | 10 km |
| $\dot{\varepsilon}_d$ | strain rate for Dorn creep law | | $3.05 \times 10^{11}$ s$^{-1}$ |
| $g$ | gravitational acceleration | | 9.8 ms$^{-2}$ |
| $\gamma$ | slope of Clapeyron curve | | 4 MPaK$^{-1}$ |
| $H_0$ | surface heat production | | $3.5 \times 10^{-6}$ Wm$^{-3}$ |
| $k$ | thermal conductivity | | 3.0 Wm$^{-1}$K$^{-1}$ |
| $\kappa$ | thermal diffusivity | | 1 mm$^2$s$^{-1}$ |
| $\lambda$ | ratio of pore pressure to $\sigma_n$ in | (i) crust<br>(ii) mantle | 0.4<br>0 |
| $\mu$ | coefficient of friction in | (i) crust<br>(ii) mantle | 0.6<br>0.8 |
| $u_0$ | initial velocity of descending slab | | 5cm yr$^{-1}$ |
| $n$ | exponent for power creep law | | 3 |
| $Q_d$ | activation energy for Dorn creep law (olivine) | | $5.4 \times 10^{5}$ Jmol$^{-1}$ |
| $Q_p$ | activation energy for power creep law | (i) quartz<br>(ii) olivine | $1.9 \times 10^{5}$ Jmol$^{-1}$<br>$5.2 \times 10^{5}$ Jmol$^{-1}$ |
| $\rho_a$ | average asthenosphere density at $T_l$ | | 3300 kgm$^{-3}$ |
| $\rho_c$ | average crustal density at $T_l$ | | 2700 kgm$^{-3}$ |
| $\rho_m$ | average mantle density at $T_l$ | | 3300 kgm$^{-3}$ |
| $\sigma_0$ | cohesion for | (i) crust<br>(ii) mantle | 0 MPa<br>60MPa |
| $\sigma_d$ | threshold stress for Dorn creep law | | 8500 MPa |
| $T_l$ | temperature at base of lithosphere | | 1280° C |
| $T_s$ | temperature at surface of lithosphere | | 0° C |

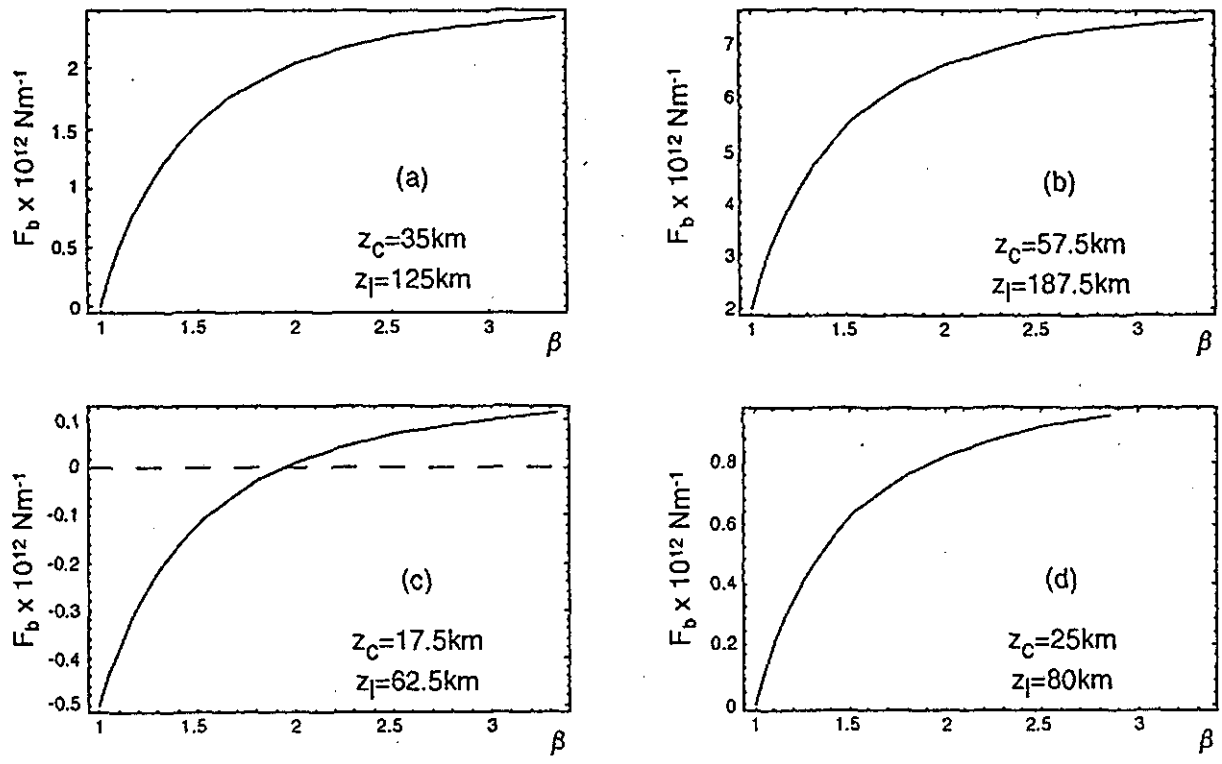


Figure 6.3 The variation in buoyancy force, $F_b$, as a function of the thinning factor, $\beta$, for different thickness parameters. The initial buoyancy force depends on the state of the lithosphere prior to delamination. Since (b) represents a thickened lithosphere and (c) represents a thinned lithosphere, they have initial buoyancy forces of 2 x $10^{12}$ Nm$^{-1}$ and -0.5 x $10^{12}$ Nm$^{-1}$ respectively.

### 2.1.2 Temperature distribution

The temperature distribution in the lithosphere is assumed to vary exponentially with depth due to the concentration of heat-producing radioactive elements in the upper crust. It is expressed by:

$$T(z) = T_0(z) + \frac{H_0 f_c^2 D_0^2}{k}\left[(1 - e^{(-z/f_c D_0)}) - (1 - e^{(-f_l z_l / f_c D_0)})\frac{z}{f_l z_l}\right] \qquad (6.7)$$

where $H_0$ is the surface heat production, $f_c$ is the crustal thickening factor, $D_0$ is the length scale for internal heat production, $k$ is thermal conductivity, $z$ is depth, $f_l$ is the lithospheric thickening factor and $T_s$ is the surface temperature [Zhou & Sandiford, 1992]. $T_0(z)$ is the temperature profile when no lithospheric heat sources are present and is given by:

$$T_0(z) = T_s + (T_l - T_s)\frac{z}{f z_l} \tag{6.8}$$

Values for $H_0$, $h_0$, $z_l$ and $D_0$ are taken from Zhou & Sandiford [1992] and were derived by balancing the potential energy of a reference lithosphere with that at the mid-ocean ridges.

It was assumed that thermal reequilibration following delamination occurred appreciably faster than deformational strain rates and lithospheric underplating. For a typical thermal time constant of 100Ma, vertical strain rates slower than $10^{-14}$ $s^{-1}$ are required when assuming time-independence [Zhou pers. comm., 1993].

Moho temperature is proportional to the thinning factor and depends on the initial thickness of the crust and mantle lithosphere (see figure 6.4). When the entire mantle lithosphere is removed, moho temperature equals that at the base of the lithosphere. Since the temperature at the base of the lithosphere is defined rheologically* for a constant temperature, changes in mean mantle temperature act only to decrease the depth of this transition (i.e. the thickness of the lithosphere).

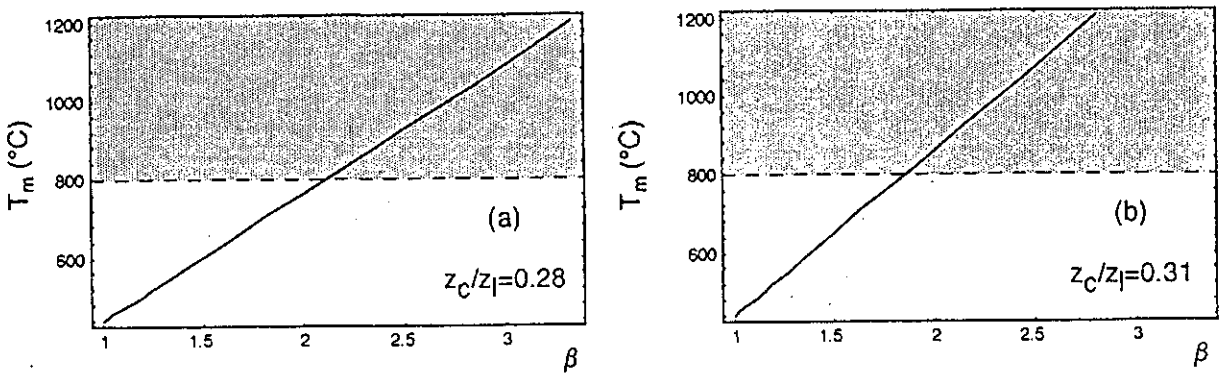


**Figure 6.4** Variation in moho temperature, $T_m$ with the thinning factor, $\beta$. The slope of the line depends on the initial crust:mantle lithosphere ratio. The stippled region indicates temperatures above the average crustal solidus.

It is acknowledged that anatexis is likely to occur in the crust for temperatures above 800°C [e.g. Sandiford et al., 1991; Sandiford et al., 1992], with important implications for melt generation following delamination. Figure 6.4(a) shows that for thinning factors greater than 2.5, moho

* The lithosphere is defined to be that part of the mantle in which heat transfer is *conductive* and the asthenosphere is defined to be that part of the mantle in which heat transfer is *advective*. Hence the boundary layer separating lithosphere and asthenosphere is rheological and is defined at a constant temperature, $T_l$.

temperatures approach or exceed those of the crustal solidus. The rheological effects of granite emplacement can be significant but depend on the location of emplacement (see strength section) [Sandiford et al., 1991], and the temporal evolution of the thermal regime. In all scenarios removal of the entire mantle lithosphere causes temperatures to exceed the solidus in the lower crust.

### 2.1.3 Surface elevation

The isostatically supported surface elevation, $h$, of a deformed lithospheric column appropriate to the exponential temperature distribution is given by:

$$h_e = h_0 + z_l f_l f_c^2 \beta_e \left[ \frac{1 + e^{-f_l z_l / f_c D_0}}{2} - \frac{f_c}{f_l} \psi_1 (1 - e^{-f_l z_l / f_c D_0}) \right] - z_l \beta_e \left[ \frac{1 + e^{-z_l / D_0}}{2} - \psi_1 (1 - e^{-z_l / D_0}) \right] \tag{6.9}$$

where $h_0$ is the elevation appropriate to a 'no heat source' lithosphere and is given by:

$$h_0 = z_l \delta \psi (f_c - 1) + \frac{\alpha (T_l - T_s)}{2} z_l (1 - f_l) \tag{6.10}$$

and;

$$\delta = \frac{\rho_m - \rho_c}{\rho_m};$$

$$\psi = \frac{z_c}{z_l};$$

$$\psi_1 = \frac{D_0}{z_l};$$

$$\beta_e = \frac{\alpha H_0 D_0^2}{k}$$

The reference surface elevation was taken to be 0 (sea level). Figure 6.5 illustrates the increase in surface elevation following delamination. It is noted that delamination does not initiate subsidence under any circumstance. Maximum elevations approach 4.5km for an initially thickened crust.

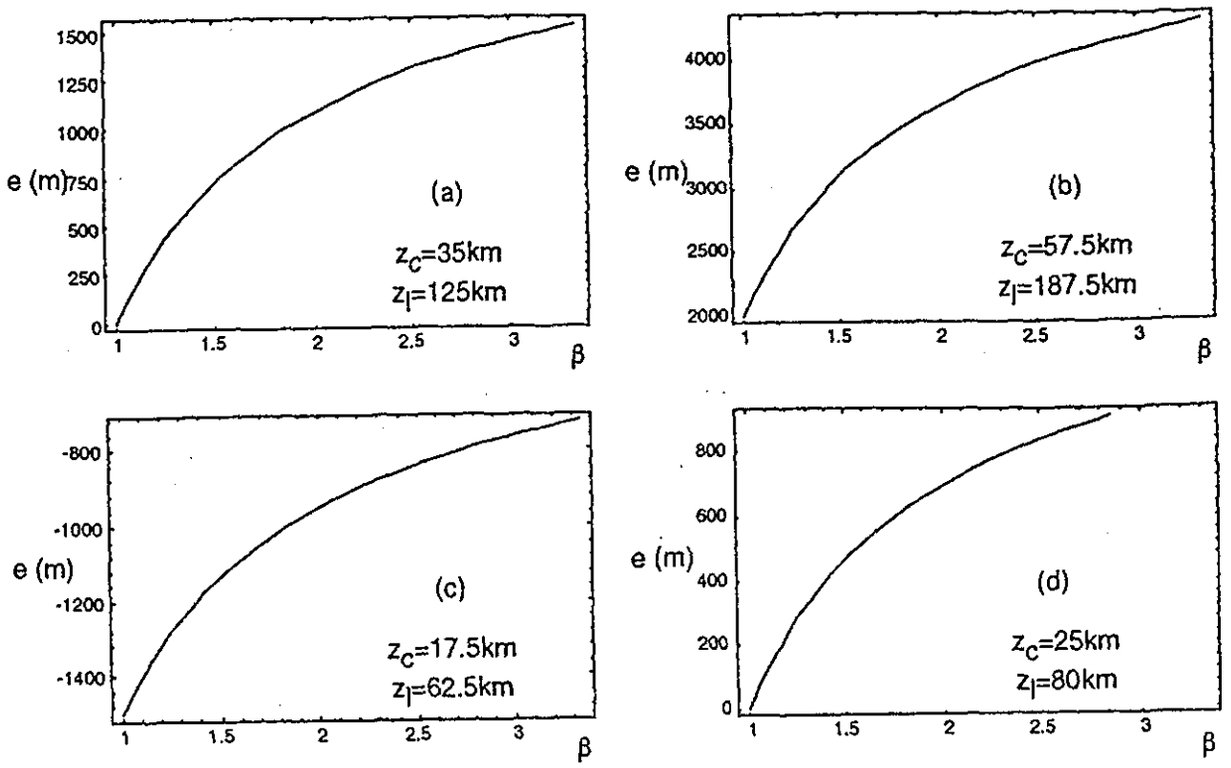


**Figure 6.5** Increase in surface elevation, $e$ with the thinning factor, $\beta$, for different thickness parameters. The initial elevation depends on the state of the lithosphere prior to delamination. Since (b) represents a thickened lithosphere and (c) represents a thinned lithosphere, they have initial elevations of 2km and -1.5km respectively.

### 2.1.2 Lithospheric strength

In order to calculate the integrated strength of the continental lithosphere it is necessary to consider the brittle and ductile parts separately for both the crust and mantle. A detailed description of lithospheric strength calculations is provided in Appendix 1.

The integrated strength of the continental lithosphere, $F_l$, is given by:

$$F_l = \int_h^{z_l} (\sigma_1 - \sigma_3) dz \tag{6.11}$$

where $\sigma_1$ and $\sigma_3$ are the maximum and minimum deviatoric stresses required for failure. $(\sigma_1 - \sigma_3)$ must be evaluated for the brittle and ductile parts of the crust and mantle lithosphere assuming a vertically averaged rheology. The 'Brace-Goetze' rheology is used here, and is described in Appendix 1 [Zhou &

Sandiford, 1992].

Zhou & Sandiford [1992] demonstrate the futility of calculating an *absolute* strength value for the lithosphere due to uncertainties in the rheological parameters*, however strength differences can be estimated successfully.

The strength of the lithosphere is strongly dependent on its thermal state and drops exponentially with increasing moho temperature. Figure 6.6 illustrates lithospheric strength estimates for different strain rates.

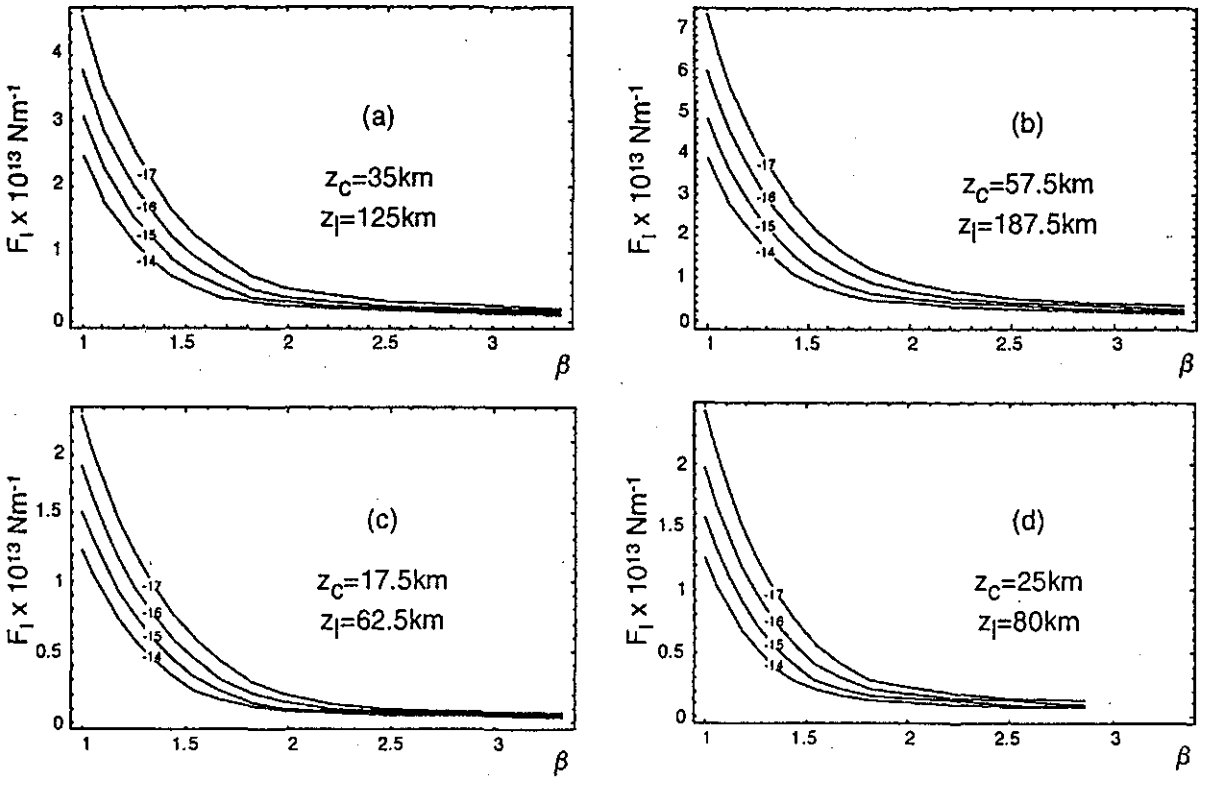


Figure 6.6 Decrease in compressional lithospheric strength, $F_l$ with the thinning factor, $\beta$, for different strain rates, $\dot{\varepsilon}$ (family of 4 curves representing $\dot{\varepsilon}=10^{-17}$, $10^{-16}$, $10^{-15}$ and $10^{-14}s^{-1}$) and initial thickness parameters.

The assumed 'Brace-Goetze' rheology has two distinct deviatoric stress failure maxima (for crust and mantle), the position of which is governed by the brittle-ductile transitions (see figure 6.7). Brittle-ductile transitions in the crust range from 12 to 19km for various strain rates and thermal configurations. Brittle failure in the mantle only occurs under cool conditions

* A 10% uncertainty in creep law activation energy can effect the strength magnitude by an order of 10 [Zhou & Sandiford, 1992]. Estimates for absolute strength of 1-4 x $10^{13}$ Nm$^{-1}$ are obtained from the force balance on a maximally thickened crust (70km), since the horizontal buoyancy force and driving force are well constrained [Zhou & Sandiford, 1992; Molnar, 1992].

at fast strain rates. Mantle lithosphere delamination acts to significantly weaken the remaining material assuming thermal maturation. Lithospheric strength also depends on strain rate (the faster the strain the greater the strength), more so for a thicker lithosphere. The integrated extensional strength of the lithosphere is less than its compressional strength (see figure 6.7).

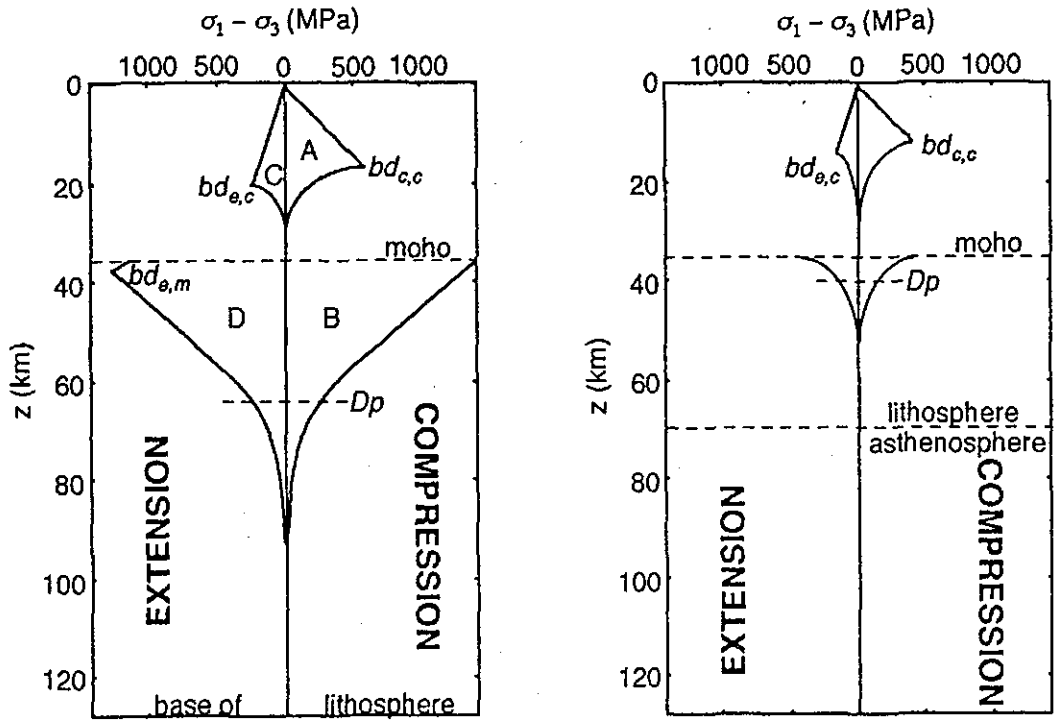


Figure 6.7 Lithospheric strength envelopes for a reference lithosphere, left ($z_c$=35km, $z_l$=125km), and a thinned, 'delaminated' lithosphere, right ($z_c$=35km, $z_l$=35km). Strength is defined as the deviatoric stress required for failure, $\sigma_1 - \sigma_3$. The integrated compressional and extensional strength of the lithosphere is obtained by adding areas A and B, or C and D, respectively. Brittle-ductile transitions are labelled $bd_{c,c}$ (compression of crust), $bd_{e,c}$ (extension of crust) and $bd_{e,m}$ (extension of mantle), and Dorn-power creep transitions, *Dp*.

### 2.1.3 Evaluation of a tectonic driving force

If an external driving force is responsible for deformation, its magnitude is limited by the strength of the reference lithosphere. Feasible driving forces range up to ~2 x $10^{13}$ $Nm^{-1}$, and are attributed to 'slab pull' and 'ridge push' effects. Such driving forces were probably less in the Proterozoic since relative plate movement was minimal [Piper, 1991].

Kröner [1981; 1983] and Etheridge et al. [1987] propose the 'slab pull' force of the delaminating lithosphere is the major convergent driving force. Turcotte & Schubert [1982] define two components of 'slab pull'; the force due to the density defect and the force due to possible phase transitions in the subducting slab (e.g. the gabbro-eclogite transition). Since the density defect is largely due to temperature differences (by definition) this component of slab pull, $F_{\Delta T}$, is:

$$F_{\Delta T} = 2\rho_a g \alpha b (T_l - T_s)\left(\frac{\kappa l}{2\pi u_0}\right)^{\frac{1}{2}} \tag{6.12}$$

where $\rho_a$ is the density of the mantle, $g$ is acceleration due to gravity, $\alpha$ is the coefficient of thermal expansion, $b$ is the vertical length of the descending slab, $T_l$ is the temperature of the mantle, $T_s$ is the surface temperature, $\kappa$ is the diffusivity, $l$ is the horizontal length scale of the slab and $u_0$ is the velocity of the descending slab. Phase changes are considered unlikely for limited subduction of continental lithosphere [Ellis & Maboko, 1992].

# 3 On the mechanical plausibility of ensialic orogenesis

The effects of mantle lithosphere delamination (i.e. thinning) on surface elevation, moho temperature, buoyancy force and lithospheric strength are investigated graphically (see figures 6.8 & 6.9). The aim here is to graphically portray the force balance for a given strain rate. It follows from equation (6.1) that the minimum driving force required to deform the lithosphere at given strain rates, $F_{dmin}$ is:

$$F_{dmin} = \mid F_b + F_{l2} \mid \tag{6.13}$$

where $F_b$ is the horizontal buoyancy force and $F_{l2}$ is the strength of the deformed column. Plots of $F_{dmin}$ versus the thinning factor are given in figure 6.8. For scenarios where buoyancy forces may exceed driving forces, the *effective driving force*, $F_{ed}$ is considered, where;

$$F_{ed} = F_d - F_b \tag{6.14}$$

for a given strain rate. A negative effective driving force is extensional and if

it exceeds the extensional strength of the thinned lithosphere, extension will occur (and vice versa). This is expressed graphically by plotting effective driving force versus lithospheric strength (see figure 6.9). The line:

$$F_{ed} = | F_l | \tag{5}$$

defines the 'failure' envelope. Deformation will occur if the effective driving force - strength curve transects this line (shaded region of figure 6.9).

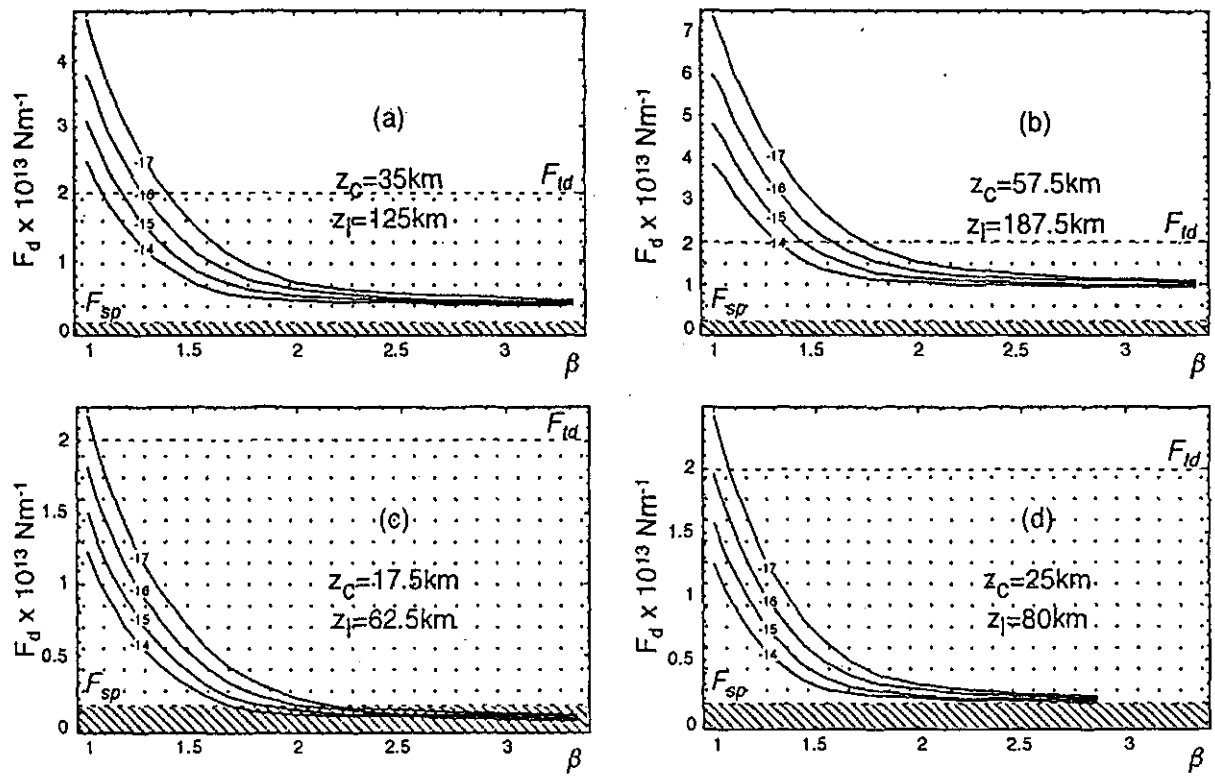


Figure 6.8 Variation in driving force required for deformation $F_d$, with the thinning factor, $\beta$, for different strain rates, $\dot{\varepsilon}$ (family of 4 curves representing $\dot{\varepsilon}=10^{-17}$, $10^{-16}$, $10^{-15}$ and $10^{-14}s^{-1}$), and initial thickness parameters. Estimate for the possible 'slab pull' force, $F_{sp}$, and the maximum tectonic driving force, $F_{td}$, are shown. The lightly shaded region shows parameter range appropriate to convergent deformation due to the maximum driving force. The heavily shaded region shows parameter range appropriate to convergent deformation due to 'slab pull'.

For delamination of an unthickened lithosphere, convergent deformation will occur given a sufficient driving force. This occurs most readily if the entire mantle part of the lithosphere is removed, requiring minimum driving forces in the order of $6 \times 10^{12}$ Nm$^{-1}$ to deform at strain rates between $10^{-17}$ and $10^{-14}s^{-1}$ for an initial configuration of $z_c$=35km and $z_l$=125km. Convergent

deformation will occur for maximum driving forces (~2 x $10^{13}$ $Nm^{-1}$) when crustal thinning factors of 1.1 ($\dot{\varepsilon} = 10^{-14}$ $s^{-1}$) to 1.4 ($\dot{\varepsilon} = 10^{-17}$ $s^{-1}$) arise. For thicker initial configurations, higher buoyancy forces prevent convergent deformation at feasible driving forces (~2 x $10^{13}$ $s^{-1}$), and extension may ensue if buoyancy forces exceed the combined strength and driving force (shaded region in figure 6.9).

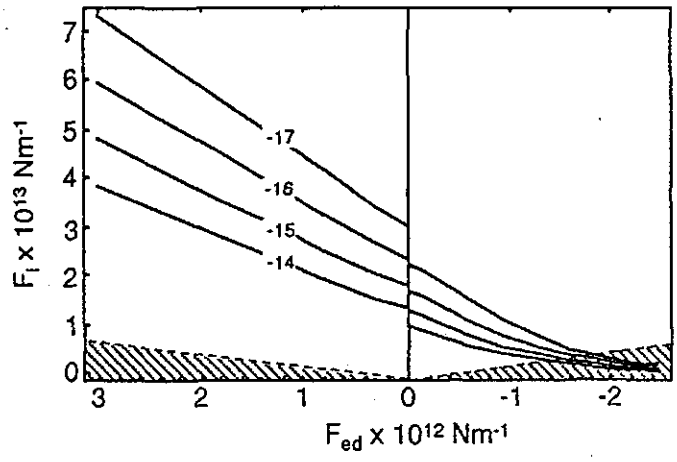


**Figure 6.9** Graph showing changes in lithospheric strength versus the effective driving force (which is a function of the thinning factor) for different strain rates ($\dot{\varepsilon}$=$10^{-17}$ to $10^{-14}$ $s^{-1}$). Negative driving forces are extensional (and vice versa). The shaded areas represent driving forces greater than the strength, allowing deformation at a given strain rate.

# 4 Summary of results

The results of the numerical model are summarised as follows:

(i) Although mantle lithosphere delamination of an undeformed (reference) lithosphere is unlikely [Houseman et al., 1981], it can initiate convergent deformation in the 'delaminated' zone at relatively large driving forces.

(ii) Mantle lithosphere delamination of a thickened lithosphere does not initiate or perpetuate convergent deformation at feasible driving forces. Extensional collapse will ensue if compressional driving forces are relaxed.

(iii) Mantle lithosphere delamination of a thinned lithosphere can initiate convergent deformation if initial extensional driving forces are relaxed. Further extension is possible if extensional driving forces persist. The 'slab pull' force is sufficient to cause convergent deformation at

appreciable rates if more than half of the mantle lithosphere is removed. Compressional buoyancy forces are not overcome by delamination and act to increase the chance of convergent deformation.

(iv) For an initially thinner, 'hotter' lithosphere the likelihood of deformation is enhanced due to its weakness, although buoyancy forces are less.

# Chapter 7

## Discussion and application of tectonic modelling

The numerical model presented in Chapter 6 provides a simple graphical means for investigating the mechanical consequences of ensialic mantle lithosphere delamination. Zhou & Sandiford [1992] have shown that such models are sensitive to the assumed thermal parameters, rendering many absolute calculations futile. However important qualitative insights into the tectonic implications of various delamination scenarios can be made.

The likelihood of deformation at feasible driving forces and strain rates depends on the initial state of the lithosphere (see Chapter 6, §4). I have shown the mechanical consequences of delamination for 4 initial configurations, all of which can explain widespread low-pressure–high-temperature metamorphism and anorogenic magmatism. Further constraints must be obtained from the geological record. In cases where delamination *precedes* convergent deformation, heating (i.e. metamorphism and magmatism) will be pre-syn orogenic resulting in *anticlockwise* pressure-temperature-time paths. If delamination occurs as a *result* of lithospheric thickening, high-temperature metamorphism and magmatism would be syn-post orogenic resulting in *clockwise* pressure-temperature-time paths, with high-temperature assemblages overprinting earlier high(er)-pressure assemblages [e.g. Sandiford, 1989b]. In cases where the lithosphere is initially thinned, sedimentation may cause a thermal blanketing effect (for timescales less than 50Ma[#]) which will weaken the entire lithosphere by reducing surface heat flow [Zhou pers. comm., 1993]. Since timescales for convergent deformation must be less than the timescale for 'sag phase' lithospheric accretion, thermal blanketing effects may play an important supporting role in enabling convergent deformation.

A higher mean mantle temperature during the Proterozoic may have caused a thinner lithosphere to form which was weaker and less buoyant than the modern 'reference' lithosphere [Zhou pers. comm., 1993]. Driving forces

[#] The maximum time required for thermal re-equilibration following fast sedimentation is ~50Ma [Zhou pers. comm., 1993].

required for deformation would be considerably less.

Spontaneous delamination of the mantle lithosphere from a 'reference' lithosphere is unlikely since boundary layer instabilities are unlikely to develop [Houseman et al., 1981], and the density defect between the 'cold' mantle lithosphere and the asthenosphere is insufficient to overcome its tensional strength [Ellis, 1992].

The model presented here shows that delamination of the entire mantle lithosphere raises moho temperatures well above the crustal liquidus potentially resulting in voluminous magmatism, greatly weakening the remaining lithosphere. The rheological effects of magmatism on the lithosphere are discussed by Sandiford et al. [1991].

Geological evidence from the Mount Painter Inlier suggests that peak metamorphism and magmatism was syn- to post-deformational for both major Proterozoic orogenies. Diffusion constraints indicate anticlockwise pressure-temperature-time paths [Stüwe pers. comm., 1993]. Since heating *postdated* crustal thickening, delamination may have *postdated* deformation (assuming deformation is convergent). High grade granulites indicate maximum crustal thickening and moho temperatures in excess of 40km and 850°C (i.e. above reference). Hence the initiating mechanism for deformation may not be explained by mantle lithosphere delamination. Repeated extension – compression cycles (Palaeoproterozoic, Mesoproterozoic, Adelaidean-Delamerian and Tertiary) along a northeasterly axis may indicate a fundamental, localised lithospheric weakness [e.g. Ding et al., 1992], possibly associated with the weakening effects of the concentration of heat-producing (radioactive) elements in the area.

The mechanical consequences of mantle lithosphere delamination strongly depend on the initial state of the lithosphere and the magnitude of the tectonic driving forces. I have shown that mantle lithosphere delamination may localise and initiate ensialic convergent deformation in response to intraplate stresses (i.e. driving forces). The magnitude of such stresses is poorly understood, especially for the Proterozoic, although recent work by Zhou, Sandiford & Hillis [in prep.] will constrain these values. Findings presented here are limited by our poor understanding of the rheological properties of the lithosphere - hence its strength. The remarkable

heterogeneity of the continental lithosphere, which is reflected in the geological record, emphasises the limitations of any tectonic 'quantification'. However, such models have provided unique insights into the fickle nature of tectonic behaviour, so that we can further understand the evolution of our planet, and even predict its future.

# Acknowledgments

I sincerely thank my supervisor, Mike Sandiford, for his inspiration, patience and support through the year, especially in the last few months. This project would have been impossible without him.

My co-worker, Bruce Schaefer, deserves high accolades for putting up with me in the field for 2 months! We both pulled through, however. Thanks, Bruce, for a great year - this thesis wouldn't be the same without your opinions and insights.

Drs Kurt Stüwe and Shaohua Zhou were immensely helpful through the year - many thanks. Drs John Foden, Jim Sears, Pat James and Thomas Flöttmann, and Annette Bingemer were also helpful and their support has been welcome - thanks. Thanks also to the technical staff - namely Sherry (drafting), Geoff and Wayne (sections), and Sophia (management). Huw Rosser, whose help on the microprobe was indispensable, made an otherwise tedious job quite bearable.

Thanks to SADME for generously providing the Landcruiser and RFDS radio for our fieldwork, which wouldn't have been possible otherwise. Thanks also for the 30 thin sections. Malcolm Sheard and Wolfgang Preiss provided helpful ideas during visits to SADME. Thanks to Prue Freeman and Tony Belperio for their help with computing. Thanks to CRA for providing logistical support - the aerial photographs, maps, use of their field camp at Arkaroola, and the helicopter rides were all immensely helpful (and fun!).

I also thank the Sprigg family at Arkaroola for the privilege of being able to explore and map on their spectacular property. The staff at Arkaroola were wonderfully helpful and made our weekly sojourns great fun!

Thanks to the honours students who made this year a great one - especially those from 'the office from hell'!

Finally, thanks to Mum and Dad from their support from afar, and for being so generous with the computer, car etc etc etc...

# References


Anderson, S.L. & Burke, K., 1983, A Wilson Cycle approach to some Proterozoic problems in north-eastern North America. In Medaris, L.G., et al. (eds.), Proterozoic geology: Selected papers from an International Proterozoic Symposium, *The Geological Society of America*, Memoir 161, p75-94.

Arnold, J. & Sandiford, M.A., 1990, Petrogenesis of cordierite-orthoamphibole assemblages from the Springto region, South Australia. In *Contributions to Mineralogy and Petrology*, 106, p100-109.

Baer, A.J., 1983, Proterozoic orogenies and crustal evolution. In Medaris, L.G., et al. (eds.), Proterozoic geology: Selected papers from an International Proterozoic Symposium, *The Geological Society of America*, Memoir 161, p47-58.

Barker, A.J., 1990, *Introduction to Metamorphic Textures and Microstructures*. Blackie, London, 162p.

Bickle, M.J., 1978, Heat loss from the earth: A constraint on Archaean tectonics from the relation between geothermal gradients and the rate of plate production. In *Earth and Planetary Science Letters*, 40, p301-315.

Bird, P. & Baumgardner, J., 1981, Steady propagation of delamination events. In *Journal of Geophysical Research*, 86 (B6), p4891-4903.

Blake, D.H., Stewart, A.J. & Sweet, I.P., 1986, The Proterozoic Hatches Creek Group, an ensialic sandstone-bimodal volcanic association in Central Australia. In *Transactions of the Geological Society of South Africa*, 89, p243-251.

Blight, P.G., 1977, Uraniferous metamorphics and 'younger' granites of the Paralana area, Mount Painter Province, South Australia: A petrographical and geochemical study. Unpublished honours thesis, University of Adelaide.

Brace, W.F. & Kohlstedt, D.L., 1980, Limits on lithospheric stress imposed by laboratory experiments. In *Journal of Geophysical Research*, 85, p6248-6252.

Byerlee, J.D., 1968, Brittle-ductile transition in rocks. In *Journal of Geophysical Research*, 73, p4741-4750.

Christensen, U.R., 1985, Thermal evolution models for the earth. In *Journal of Geophysical Research*, 90(B4), p2995-3007.

Coats, R.P. & Blissett, A.H., 1971, Regional and Economic Geology of the Mount Painter Province, *SADME Bulletin* 43, Government Printer, Adelaide, 426p.

Condie, K.C., 1980, Proterozoic tectonic regimes. In *Abstracts with Programs, Geological Society of America*, 12 (7), p404-405.

Condie, K.C., 1989, *Plate tectonics and crustal evolution*, 3rd edition, Pergamon, Oxford, 366p.

Deer, W.A., Howie, R.A. & Zussman, J., 1992, *An Introduction to the Rock-Forming Minerals*, 2nd ed. Longman, London, 695p.

Ding, P., James, P.R. & Sandiford, M.A., 1992, Late Proterozoic deformation in the Amadeus Basin, central Australia. In *Australian Journal of Earth Sciences*, 39, p495-500.

Ellis, D.J. & Maboko, M.A.H, 1992, Precambrian tectonics and the physicochemical evolution of the continental crust, I. The gabbro-eclogite transition revisited. In *Precambrian Research*, 55, p491-506.

Ellis, D.J., 1992, Precambrian tectonics and the physicochemical evolution of the continental crust, II. Lithosphere delamination and ensialic orogeny. In *Precambrian Research*, 55, p507-524.

Elter, P. & Trevisan, L., 1973, Olistostromes in the tectonic evolution of the Northern Appenines. In De Jong, K.A. & Scholten, R. (eds.), *Gravity and Tectonics*, Wiley, New York.

Etheridge, M.A., Rutland, R.W.R., & Wyborn, L.A.I., 1987, Orogenesis and tectonic process in the early to middle Proterozoic of Northern Australia. In Kröner, A. (ed.), Proterozoic lithospheric evolution, Geodynamic Series, 17, *American Geophysical Union, Geological Society of America.*, p131-147.

Fyfe, W.S., 1976, Heat flow and magmatic activity in the Proterozoic. In Sutton, J. (ed.), A discussion on global tectonics in Proterozoic times, *Philosophical Transactions of the Royal Society of London*, 280 (1298), p655-660.

Glikson, A.Y., 1981, Uniformitarian assumptions, plate tectonics and the Precambrian earth. In Kröner, A. (ed.), *Precambrian Plate Tectonics*. Elsevier, Amsterdam, p91-104.

Grambling, J.A., 1984, Regional metamorphism in central and northern New Mexico, and implications for Proterozoic tectonics. In *Abstracts with Programs Geological Society of America*, 16 (6), p522-523.

Green, D.H. & Hiberson, W., 1970, The instability of plagioclase in peridotite at high pressure. In *Lithos 3*, p209-221.

Hargraves, R.B., 1981, Precambrian tectonic style: a liberal uniformitarian interpretation. In Kröner, A. (ed.), *Precambrian Plate Tectonics*. Elsevier, Amsterdam, p21-56.

Hewens, R.H., 1975, Pyroxene geothermomentry of some granulite facies rocks. In *Contributions to Mineralogy and Petrology*, 50, 205-209.

Hildebrand, R.S., Reichenbach, I.G., Hoffman, P.F., Easton, R., Lalonde, A.E., Bowring, S.A. & Housh, T., 1988, Magmatism at a 1.9Ga Cordilleran-type plate margin. In *Abstracts with Programs Geological Society of America.*, 20 (7), p50.

Hobbs, B.E., Means, W.D. & Williams, P.F., 1976, *An Outline of Structural Geology*. Wiley, New York.

Hoffman, P.F., 1980, Wopmay Orogen: A Wilson Cycle of early Proterozoic age in the northwest of the Canadian Shield. In Strangway, D.W. (ed.), The Continental Crust and its Mineral Deposits, *Geological Association of Canada Special Paper*, 20, p523-549.

Hoffman, P.F., 1988, Early Proterozoic orogens and the assembly of Laurentia. In *Abstracts with Programs Geological Society of America*, 20 (1), p27.

Hoffman, P.F., 1990, Dynamics of the tectonic assembly of northeast Laurentia in geon 18 (1.9-1.8 Ga). In *Geoscience Canada*, 17 (4), p222-226.

Holland & Powell, 1990, An enlarged and updated internally consistent thermodynamic dataset with uncertainties and correlations: the system $K_2O$ - $Na_2O$ - CaO - MgO - FeO - $Fe_2O_3$ - $Al_2O_3$ - $TiO_2$ - $SiO_2$ - C - $H_2$ - $O_2$. In *Journal of Metamorphic Geology*, 8, p89-124.

Houseman, G.A., McKenzie, D.P. & Molnar, P., 1981, Convective instability of a thickened boundary layer and its relevance for the thermal evolution of continental convergent belts, *Journal of Geophysical Research*, 86(B7), p6115-6132.

Kovács, S., 1989, Devonian olistostrome with limestone olistoliths and volcanic matrix from Strázsa Hill, Uppony Mountains, northeastern Hungary. In *Neues Jahrbuch für Geologie und Paläontologie: Monatschefte*, 2, 109-127.

Kröner, A., 1977, Precambrian mobile belts of southern and eastern Africa - ancient sutures or sites of ensialic mobility? A case for crustal evolution towards plate tectonics. In McElhinny, M.W. (ed.), The past distribution of continents, *Tectonophysics*, 40, p101-135.

Kröner, A., 1981, Precambrian plate tectonics. In Kröner, A. (ed.), *Precambrian Plate Tectonics*. Elsevier, Amsterdam, p57-90.

Kröner, A., 1983, Proterozoic mobile belts compatible with the plate tectonic concept. In Medaris, L.G., et al. (eds.), Proterozoic geology: Selected papers from an International Proterozoic Symposium, *The Geological Society of America*, Memoir 161, p59-74.

Kröner, A., 1984, Evolution, growth and stabilization of the Precambrian lithosphere. In Pollack, H.N. & Murthy, V.R., Structure and evolution of the continental lithosphere, *Physics and Chemistry of the Earth*, 15, p69-106.

Kröner, A., Hoffman, P.F., Burg, J.F. & Caby, R., 1985, Are the Proterozoic fold belts of Australia ensialic? In *Episodes*, 8 (4), p265-266.

Loosveld, R.J.H. & Etheridge, M.A., 1990, A model for low-pressure facies metamorphism during crustal thickening. In *Journal of Metamorphic Geology*, 1990(8), p257-267.

Marshak, S. & Mitra, G., 1988, *Basic Methods of Structural Geology*, Prentice Hall, New Jersey, 446p.

McElhinny, M.W. & Embleton, B.J.J., 1976, Precambrian and early Palaeozoic palaeomagnetism in Australia. In Sutton, J. (ed.), A discussion on global tectonics in Proterozoic times, *Philosophical Transactions of the Royal Society of London*, 280 (1298), p417-431.

McKenzie, D. & Weiss, N., 1980, The thermal history of the Earth. In Strangway, D.W. (ed.), The Continental Crust and its Mineral Deposits, *Geological Association of Canada Special Paper*, 20, p575-590.

Myers, J.S., 1990, Precambrian tectonic evolution of part of Gondwana, southwestern Australia. In *Geology*, 18, p537-540.

Newton, R.C., 1987, Petrologic aspects of Precambrian granulite facies terrains bearing on their origins. In Kröner, A. (ed.), Proterozoic lithospheric evolution, Geodynamic Series, 17, *American Geophysical Union, Geological Society of America*, p11-26.

Passchier, C.W., Myers, J.S. & Kröner, A., 1990, *Field Geology of High-Grade Gneiss Terrains*. Springer-Verlag, Berlin, 150p.

Piper, J.D.A., 1991, The quasi-rigid premise in Precambrian tectonics. In *Earth and Planetary Science Letters*, 107, p559-569.

Plumb, K.A., 1985a, Central Australian Orogeny - and Himalayan comparisons. In *Tectonics and Geochemistry of Early to Middle Proterozoic Fold Belts*, IGCP Conference program and abstracts.

Plumb, K.A., 1985b, Proterozoic orogeny worldwide - diachronous, random, or episodic? In *Tectonics and Geochemistry of Early to Middle Proterozoic Fold Belts*, IGCP Conference program and abstracts.

Rossiter, A.G. & Ferguson, J., 1980, A Proterozoic tectonic model for northern Australia and its economic implications. In Ferguson, J. & Goleby, A.B. (eds.), *Uranium in the Pine Creek*

*Geosyncline*, IAEA, Vienna, p209-232.

Sandiford, M.A. & Powell, R., 1986, Deep crustal metamorphism during continental extension: modern and ancient examples. In *Earth and Planetary Science Letters*, 79, p151-158.

Sandiford, M.A., 1989a, Horizontal structures in granulite terrains: A record of mountain building or mountain collapse? In *Geology*, 17, p449-452.

Sandiford, M.A., 1989b, Secular trends in the thermal evolution of metamorphic terrains. In *Earth and Planetary Science Letters*, 95, p85-96.

Sandiford, M.A. & Powell, R., 1990, Some isostatic and thermal consequences of the vertical strain geometry in convergent orogens. In *Earth and Planetary Science Letters*, 98, p154-165.

Sandiford, M.A. & Powell, R., 1991, Some remarks of high-temperature–low-pressure metamorphism in convergent orogens. In *Journal of Metamorphic Geology*, 1991(9), p333-340.

Sandiford, M.A., Martin, N., Zhou, S. & Fraser, G., 1991, Mechanical consequences of granite emplacement during high-*T*, low-*P* metamorphism and the origin of "anticlockwise" *PT* paths. In *Earth and Planetary Science Letters*, 107, p164-172.

Sandiford, M.A. & Foden, J.F., 1992, *Third year tectonics notes*, unpublished.

Sandiford, M.A., Foden, J., Zhou, S. & Turner, S., 1992, Granite genesis and the mechanics of convergent orogenic belts with application to the Southern Adelaide Fold Belt. In *Transactions of the Royal Society of Edinburgh: Earth Sciences*, 83, p.

Schaefer, B.F., 1993, Isotopic and geochemical constraints on Proterozoic crustal growth from the Mount Painter Inlier. Unpublished honours thesis, University of Adelaide.

Sivell, W., 1988, Eastern Arunta orthogneiss suites - implications for a repeated transition from rift to subduction-related magmatism during successive Proterozoic ensialic orogenies. In *Geological Society of Australia Abstracts*, 21, p370-371.

Sonder, L.J. & England, P., 1986, Vertical averages of rheology of the continental lithosphere: relation to thin sheet parameters. In *Earth and Planetary Science Letters*, 77, p81-90.

Tarling, T.H., 1980, Lithosphere evolution and changing tectonic regimes. In *Journal of the Geological Society of London*, 137, p459-467.

Teale, G.S., 1993, Geology of the Mount Painter and Mount Babbage Inliers. In *Geology of South Australia*, SADME, in press.

Turcotte, D.L. & Schubert, G., 1982, *Geodynamics. Applications of Continuum Physics to Geological Problems*, Wiley, New York, 450p.

Turcotte, D.L., 1987, Implications of lithosphere delamination on Venus. In *EOS, Transactions of the American Geophysical Union*, 68 (44), p1338-1339.

Vivallo, W. & Rickard, D., 1984, Early Proterozoic ensialic spreading-subsidence: Evidence from the Garpenberg Enclave, Central Sweden. In *Precambrian Research*, 26, p203-221.

Wells, P.R.A., 1977, Pyroxene thermometry in simple and complex systems. In *Contributions to Mineralogy and Petrology*, 62, p129-139.

Windley, B.F., 1981, Precambrian rocks in the light of the plate tectonic concept. In Kröner, A. (ed.), *Precambrian Plate Tectonics*. Elsevier, Amsterdam, p1-20.

Windley, B.F., 1983, A tectonic review of the Proterozoic. In Medaris, L.G., et al. (eds.), Proterozoic geology: Selected papers from an International Proterozoic Symposium, *The Geological Society of America*, Memoir 161, p1-10.

Wolfram, S., 1992, *Mathematica™: A System for Doing Mathematics by Computer*. Addison-Wesley, Sydney.

Wyborn, L.A.I., 1985, Geochemistry and origin of a major early Proterozoic felsic igneous event of northern Australia and evidence for substantial vertical accretion of the crust. In *Tectonics and Geochemistry of Early to Middle Proterozoic Fold Belts*, IGCP Conference program and abstracts.

Wynne-Edwards, H.R., 1976, Proterozoic ensialic orogenesis: The millipede model of plate tectonics. In *American Journal of Science*, 276, p927-953.

Xu, G., Will, T.M. & Powell, R., 1993, A calculated petrogenetic grid for the system $K_2O$ - FeO - MgO - $Al_2O_3$ - $SiO_2$ - $H_2O$, with particular reference to contact metamorphosed pelites. In press.

Yardley, B.W.D., 1989, *An Introduction to Metamorphic Petrology*, Longman, New York, 248p.

Zhou, S. & Sandiford, M.A., 1992, Mafic magmatic underplating as a possible initialising mechanism of extensional basin formation. Unpublished.

Zhou, S. & Sandiford, M.A., 1992, On the stability of isostatically compensated mountain belts. In *Journal of Geophysical Research*, 97(B10), p14207-14221.

# Appendix 1

## Lithospheric strength calculations

## 1 Introduction

For strength calculations I assume a 'Brace-Goetze' rheology which is derived from Jaeger & Cook [1969], Brace & Kohlstedt [1980], Sonder & England [1986] and Zhou & Sandiford [1992].

## 2 Derivation of the brittle failure envelope

Brittle failure via frictional sliding in the lithosphere occurs at low temperatures and high strain rates. The Navier-Coulomb criterion for brittle fracture along a plane is:

$$|\tau| = \sigma_0 + \mu\sigma_n \tag{1}$$

where $\tau$ is the shear stress along the plane, $\sigma_n$ is the normal stress on the plane, $\sigma_0$ is the cohesion of the material and $\mu$ is the coefficient of internal friction of the material (see figure A1.1) [Byerlee, 1968; Jaeger & Cook, 1969]. This can be expressed diagrammatically [Jaeger & Cook, 1969]:

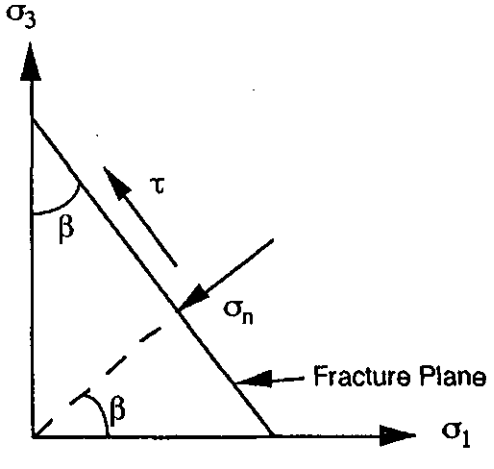


Figure A1.1 Diagrammatic portrayal of shear and normal stresses acting on a plane where $\sigma_1$ and $\sigma_3$ are the maximum and minimum deviatoric stresses required for failure [Jaeger & Cook, 1969].

Using trigonometric algebra, it can be shown that [Jaeger & Cook, 1969]:

$$\sigma_n = \frac{1}{2}(\sigma_1 + \sigma_3) + \frac{1}{2}(\sigma_1 - \sigma_3)\cos 2\beta \tag{2}$$

$$\tau = -\frac{1}{2}(\sigma_1 - \sigma_3)\sin 2\beta \tag{3}$$

where $\sigma_1$ and $\sigma_3$ are the maximum and minimum deviatoric stresses. Substituting these values in equation (1) gives:

$$\left|-\frac{1}{2}(\sigma_1 - \sigma_3)\sin 2\beta\right| = \sigma_0 + \frac{1}{2}\mu(\sigma_1 + \sigma_3) + \frac{1}{2}\mu(\sigma_1 - \sigma_3)\cos 2\beta \tag{4}$$

$$\therefore \sigma_0 = \frac{1}{2}(\sigma_1 - \sigma_3)[\sin 2\beta - \cos 2\beta] - \frac{1}{2}\mu(\sigma_1 - \sigma_3) \tag{5}$$

Now $\sigma_0$ is maximum when:

$$\tan 2\beta = -\frac{1}{\mu} \tag{6}$$

So;

$$\sin 2\beta = \frac{1}{\sqrt{\mu^2 + 1}}; \quad \cos 2\beta = \frac{-\mu}{\sqrt{\mu^2 + 1}} \tag{7}$$

and;

$$\sigma_0 = \frac{1}{2}(\sigma_1 - \sigma_3)\left[\frac{1}{\sqrt{\mu^2 + 1}} + \frac{\mu^2}{\sqrt{\mu^2 + 1}}\right] - \frac{\mu}{2}(\sigma_1 - \sigma_3);$$

$$2\sigma_0 = (\sigma_1 - \sigma_3)\sqrt{\mu^2 + 1} - \mu(\sigma_1 - \sigma_3); \tag{8}$$

$$2\sigma_0 = \sigma_1(\sqrt{\mu^2 + 1} - \mu) - \sigma_3(\sqrt{\mu^2 + 1} + \mu)$$

For compression, $\sigma_3 = \sigma_z$ (the vertical stress), so, from (8);

$$\sigma_1 = \frac{2\sigma_0}{\sqrt{\mu^2 + 1} - \mu} + \frac{\sigma_z(\sqrt{\mu^2 + 1} + \mu)}{\sqrt{\mu^2 + 1} - \mu} \tag{9}$$

and subtracting $\sigma_3$ from both sides gives:

$$\sigma_1 - \sigma_3 = \frac{2\sigma_0}{\sqrt{\mu^2+1}-\mu} + \sigma_z\left[\frac{\sqrt{\mu^2+1}+\mu}{\sqrt{\mu^2+1}-\mu} - 1\right] \tag{10}$$

So;

$$\sigma_1 - \sigma_3 = \frac{2(\sigma_0 + \mu\sigma_z)}{\sqrt{\mu^2+1}-\mu} \tag{11}$$

For extension, $\sigma_1 = \sigma_3$, so, from (8);

$$\sigma_3 = \frac{\sigma_z(\sqrt{\mu^2+1}-\mu)}{\sqrt{\mu^2+1}+\mu} - \frac{2\sigma_0}{\sqrt{\mu^2+1}+\mu} \tag{12}$$

and subtracting $\sigma_3$ from both sides gives:

$$\sigma_1 - \sigma_3 = \frac{2\sigma_0}{\sqrt{\mu^2+1}+\mu} + \sigma_z\left[1 - \frac{\sqrt{\mu^2+1}-\mu}{\sqrt{\mu^2+1}+\mu}\right] \tag{13}$$

So;

$$\sigma_1 - \sigma_3 = \frac{2(\sigma_0 + \mu\sigma_z)}{\sqrt{\mu^2+1}+\mu} \tag{14}$$

Hence equations (11) and (14) describe a brittle failure criterion for compression and extension. Note that sign conventions differ from previous publications [e.g. Sonder & England, 1986]. For numerical modelling of the crust, fluid pore pressure, $\lambda$, is taken into account, so for compression:.

$$\sigma_1 - \sigma_3 = \frac{2(\sigma_0 + \mu\sigma_z(1-\lambda))}{\sqrt{\mu^2+1}-\mu} \tag{15}$$

and for extension:

$$\sigma_1 - \sigma_3 = \frac{2(\sigma_0 + \mu\sigma_z(1-\lambda))}{\sqrt{\mu^2+1}+\mu} \tag{16}$$

## 3 Ductile strength envelope

Ductile failure in the crust for all $\sigma_1 - \sigma_3$ and in the mantle for $\sigma_1 - \sigma_3 < 200$MPa is described by the *Power Creep Law* [Brace & Kohlstedt, 1980]:

$$\sigma_1 - \sigma_3 = \left(\frac{\dot{\varepsilon}}{A_p}\right)^{\frac{1}{n}} \exp\left(\frac{Q_p}{nRT}\right) \tag{17}$$

where $\dot{\varepsilon}$ is the strain rate, $n$ is the power law exponent, $Q_p$ is the activation energy, $A_p$ is a material constant, $R$ is the universal gas constant and $T$ is the temperature at depth z.

For the upper ductile part of the mantle lithosphere, the *Dorn Creep Law* applies when $\sigma_1-\sigma_3 > 200$MPa [Brace & Kohlstedt, 1980].

$$\sigma_1 - \sigma_3 = \sigma_d \left[1 - \sqrt{\frac{RT}{Q_d} \ln\left(\frac{\dot{\varepsilon}_d}{\dot{\varepsilon}}\right)}\right] \tag{18}$$

where $\sigma_d$, $Q_d$ and $\dot{\varepsilon}_d$ are the threshold stress, activation energy and strain rate for the Dorn creep law. $\dot{\varepsilon}_d$ must be calculated to enable a smooth transition between two creep laws when $\sigma_1-\sigma_3 = 200$MPa.

## 2 Brittle-ductile and Power-Dorn creep transitions

The brittle-ductile transition depth occurs when the ductile strength of the lithosphere becomes less than its brittle strength (defined in the above sections). Hence the lithosphere has two distinct strength maxima corresponding to the brittle-ductile transitions in the crust and mantle lithosphere. Brittle ductile transition depths are calculated by evaluating:

$$\frac{2(\sigma_0 - \mu\rho g Z_{bd}(1-\lambda))}{\sqrt{\mu^2+1}-\mu} = \left(\frac{\dot{\varepsilon}}{A_p}\right)^{\frac{1}{n}} \exp\left(\frac{Q_p}{nRT_{bd}}\right) \tag{19}$$

where $\sigma_o$ is the cohesion, $\mu$ is the coefficient of thermal expansion, $\rho$ is the density, $\lambda$ is the fluid pore pressure, $\dot{\varepsilon}$ is the strain rate, $n$ is the power law exponent, $Q_p$ is the activation energy, $A_p$ is a preexponential constant, $R$ is the universal gas constant and $Z_{bd}$ and $T_{bd}$ are the depth and temperature of the brittle-ductile transition. This expression must be evaluated independently for the crust and mantle.

The Power-Dorn creep transition in the mantle lithosphere occurs when the deviatoric stress required for failure is 200MPa (i.e. $\sigma_1-\sigma_3$ = 200MPa). The

temperature at the transition depth is first calculated by solving the following equation for $T$:

$$\left(\frac{\dot{\varepsilon}}{A_p}\right)^{\frac{1}{n}} \exp\left(\frac{Q_p}{nRT}\right) = 200\text{MPa} \tag{20}$$

The strain rate for the Dorn creep law, $\dot{\varepsilon}_d$ is then calculated to facilitate a smooth transition at the calculated temperature by solving the following equation for $\varepsilon_d$:

$$\sigma_d\left[1-\sqrt{\frac{RT}{Q_d}\ln\left(\frac{\dot{\varepsilon}_d}{\dot{\varepsilon}}\right)}\right] = 200\text{MPa} \tag{21}$$

where $Q_d$ and $\sigma_d$ are the activation energy and threshold stress for the Dorn creep law. The transition depth is then calculated by evaluating equation (17) for arbitrary $T(z)$. If the moho temperature is higher than a critical value, there will be no brittle failure in the mantle lithosphere and possibly no Dorn creep law failure. [Zhou & Sandiford, 1992]

## 3 Numerical calculation of the lithospheric strength components according to Zhou & Sandiford [1992]

Based on the previously described 'Brace-Goetze' lithosphere, Zhou & Sandiford [1992] have derived the following numerical methods for calculating the lithospheric strength components.

The vertically integrated strength of the crust can be approximated by:

$$F_c = \left(\frac{\dot{\varepsilon}}{A_p}\right)^{\frac{1}{n}} \exp\left(\frac{Q_p}{nRT_{bd}}\right)\left[\frac{1}{2}Z_{bd} + \frac{Q_p}{nR\tau_c}(y_1 - \exp(x_2 - x_1)y_2)\right] \tag{22}$$

where:

$$x_1 = \frac{Q_p}{nRT_{bd}};$$

$$x_2 = \frac{Q_p}{nRT_m};$$

$$y_1 = \frac{1}{x_1^2} + \frac{2}{x_1^3} + \frac{6}{x_1^4};$$

$$y_2 = \frac{1}{x_2^2} + \frac{2}{x_2^3} + \frac{6}{x_2^4};$$

$$\tau_c = \frac{T_m - T_{bd}}{z_c - z_{bd}}$$

and $Z_{bd}$ and $T_{bd}$ are the depth and temperature of the brittle-ductile transition, $T_m$ is the moho temperature and $\tau_c$ is the geothermal gradient in the lower crust.

The vertically integrated strength of the mantle lithosphere is given by adding the brittle, Power creep and Dorn creep components, and can be approximated by:

$$F_m^b = (Z_{bd} - z_c)\left[\left\{\frac{2(\sigma_0 - \mu\rho_c g z_c(1-\lambda_c)}{\sqrt{\mu^2+1}-\mu}\right\}_{crust} + \left\{\frac{(\sigma_0 - \mu\rho_m g(Z_{bd} - z_c)(1-\lambda_m))}{\sqrt{\mu^2+1}-\mu}\right\}_{mantle}\right]$$

$$F_m^D = \sigma_d(Z_t - Z_{bd}) - \frac{2\sigma_d}{3\tau_m}\left[T_t\sqrt{\frac{RT_t}{Q_d}\ln\left(\frac{\dot{\varepsilon}_d}{\dot{\varepsilon}}\right)} - T_{bd}\sqrt{\frac{RT_{bd}}{Q_d}\ln\left(\frac{\dot{\varepsilon}_d}{\dot{\varepsilon}}\right)}\right] \qquad (23)$$

$$F_m^P = \left(\frac{\dot{\varepsilon}}{A_p}\right)^{\frac{1}{n}} \exp\left(\frac{Q_p}{nRT_t}\right)\frac{Q_p}{nR\tau_m}(y_3 - \exp(x_4 - x_3)y_4)$$

where:

$$x_3 = \frac{Q_d}{nRT_t};$$

$$x_4 = \frac{Q_d}{nRT_l};$$

$$y_3 = \frac{1}{x_3^2} + \frac{2}{x_3^3} + \frac{6}{x_3^4};$$

$$y_4 = \frac{1}{x_4^2} + \frac{2}{x_4^3} + \frac{6}{x_4^4};$$

$$\tau_m = \frac{T_l - T_m}{z_l - z_c}$$

It must be noted that the above equations are purely simple geometric approximations of otherwise complicated integrations. They enable relatively quick computing .

# Appendix 2

## *Mathematica*™ code

The *Delamination* program was written using *Mathematica*™ on a Sun Sparc 2 computer.

```
(*-------------------------------------------------------------------
        DELAMINATION PROGRAM
-------------------------------------------------------------------

        By Jon Teasdale, September, 1993.

        This program investigates the plausibility of ensialic
        orogenesis by evaluating the force balance on a 1D litho-
        spheric column for various parameter ranges.

        It derives its inspiration from the work of
        Zhou & Sandiford [1993].

        The following parameter set is loaded first:
        This set contains all parameters necessary is this model.
        The following parameters are constants, general to the entire
        model.
===================================================================*)


<<X11.m

<<Graphics`MultipleListPlot`

$DefaultFont={"Helvetica",7}

g = 9.8                                 (* gravitational acceleration   *)

tl=1280                                 (* temp at base of lithosphere  *)

zl0=125000                              (* initial thickness of lith    *)

zc0=35000                               (* initial thickness of crust   *)

fbi=0                                   (* initial buoyancy force       *)

ei=0                                    (* initial elevation            *)

roc := 2700                             (* average crustal density      *)

roml := 3300                            (* average mantle density       *)

alpha := 3/10^5                         (* coeff of thermal expansion   *)

r=8.314                                 (* Universal Gas Constant       *)

z=.;zz=.;                               (* Miscellaneous                *)
zc=zc0
zcd=zc0
zc2=zc0



(*===================================================================
        The following set of substitutions contains all the temperature
        related information appropriate for the reference lithosphere.
-------------------------------------------------------------------*)

tconds1:={      ts->0,                  (* surface temp                 *)
```

```
                fl->1,                  (* thickening/thinning factor    *)
                h->0,                   (* surface elevation             *)
                zl->zl0,                (* thickness of lithosphere      *)
                zc->zc0,                (* thickness of crust            *)
                h0->3.5*10^-6,          (* surface heat production       *)
                d0->10000,              (* length scale of heat prod.    *)
                k->3,                   (* thermal conductivity const.   *)
                fc->1}                  (* crustal thickening factor     *)

(*=============================================================
      The folowing set of substitutions contains all information
      appropriate for the reference crust.
-------------------------------------------------------------*)

crustref:={     sigma0->0,              (* cohesion                      *)
                mu->0.6,                (* coeff of internal friction    *)
                lambda->0.4,            (* fluid pore pressure           *)
                ap->5*10^-6,            (* preexponential constant       *)
                qp->1.9*10^5,           (* power law activation energy   *)
                ro->2700,               (* average density               *)
                zc->zc0,                (* crustal thickness             *)
                zl->zl0,                (* lithospheric thickness        *)
                n->3,                   (* power law exponent            *)
                h->0,                   (* elevation                     *)
                fc->1,                  (* crustal thickening factor     *)
                fl->1,                  (* thickening/thinning factor    *)
                tl->1280,               (* temp at base of lithosphere   *)
                tm->te /. tconds1 /. {z->zc0}, (* moho temperature       *)
                t->te /. tconds1}       (* temperature distribution      *)

(*=============================================================
      The following set of substitutions contains all information
      appropriate for the reference mantle lithosphere.
-------------------------------------------------------------*)

mantleref:={    sigma0->60*10^6,
                mu->0.8,
                ro->3300,
                lambda->0,
                ap->7*10^4,
                qp->5.2*10^5,
                n->3,
                h->0,
                fl->1,
                zl->zl0,
                zc->zc0,
                sigmad->8500*10^6,      (* Dorn law threshold stress     *)
                qd->5.4*10^5,           (* Dorn law activation energy    *)
                tl->1280,
                tm->te /. tconds1 /. {z->zc0},
                t->te /. tconds1}

(*=============================================================
      The following set of substitutions contains all the temperature
      related information appropriate for the deformed lithosphere.
-------------------------------------------------------------*)

tconds2:={      zc->zc2,
                zl->zl0*fld,
                fc->zcd/zc0,
                fl->fld,
                d0->10000,
                h0->3.5*10^-6,
                k->3,
                ts->0}

(*=============================================================
      The following set of substitutions contains all information
      appropriate for the deformed crust.
-------------------------------------------------------------*)

crustdef:={     sigma0->0,
                mu->0.6,
                ro->2700,
                fl->fld,
                lambda->0.4,
                h->N[-elev /. tconds2],
                qp->1.9*10^5,
```

```
                ap->5*10^-6,
                tm->te /. tconds2 /. {z->zc0},
                n->3,
                zl->zl0*fld,
                zc->zc2,
                t->te /. tconds2,
                fc->zcd/zc0}

(*=============================================================
        The following set of substitutions contains all information
        appropriate for the deformed mantle lithosphere.
-------------------------------------------------------------------*)

mantledef:={    sigma0->60*10^6,
                mu->0.8,
                ro->3300,
                lambda->0,
                h->N[-elev /. tconds2],
                ap->7*10^4,
                qp->5.2*10^5,
                zc->zc2,
                tl->1280,
                n->3,
                fl->fld,
                fc->zcd/zc0,
                zl->zl0*fld,
                sigmad->8500*10^6,
                qd->5.4*10^5,
                tm->te /. tconds2 /. {z->zc0},
                t->te /. tconds2}


(*=============================================================
        The following routines calculate the temperature distributions
        in the lithosphere.

        Here, t0 is the temp profile for no lithospheric heat sources;
              tL is the temp profile for constant heat source;
              te is the temp profile for an exponentially varying heat
                 source with depth.
        tLc & tLm are conditional statements used when calculating tL.
-------------------------------------------------------------------*)


t0 := ts + ((tl - ts)*z)/(fl*zl0)

(*tc := t0 + tL

tL := (h0*fl*zl*z*((2*fc*zc)/(fl*zl) - (fc*zc)^2/(fl*zl)^2 - z/(fl*zl)))/
        (2*k)

        tLc := (h0*fl*zl*z*((2*fc*zc)/(fl*zl) - (fc*zc)^2/(fl*zl)^2-
                z/(fl*zl)))/(2*k);
        tLm := (h0*fc^2*zc^2*(1 - z/(fl*zl)))/(2*k)*)

te := t0 + ((h0*fc^2*d0^2)/k)*((1-E^(-z/(fc*d0)))-(1-E^((-fl*zl0)/(fc*d0)))
        *(z/(fl*zl0)))


(*=============================================================
        The following line defines the temperature distribution in
        the lithosphere according to the above routines.
-------------------------------------------------------------------*)

t:=te


(*=============================================================
        This routine calculates the density distribution within the
        continental lithosphere for a given temperature profile, t.

        rhoc is the density distribution in the crust;
        rhom is the density distribution in the mantle lithosphere.
-------------------------------------------------------------------*)

rhoc = roc + roml*alpha*(tl-t)

rhom = roml + roml*alpha*(tl-t)


(*=============================================================
```

```
        This routine calculates the elevation (elev) above the reference
        height, h0, according to an exponential heat production
        regime.
-------------------------------------------------------------------------*)

elev0:=zl0*(delta*psi*(fc-1)+alpha*(tl-ts)*(1-fl)/2)

        delta:=(roml-roc)/roml;
        psi:=zc0/zl0;
        psi1:=d0/zl0;
        betae:=(alpha*h0*d0^2)/k

elev:=elev0+zl0*fl*fc^2*betae*(((1+Exp[-fl*zl0/(fc*d0)])/2)-(fc/fl)*psi1*
        (1-Exp[-fl*zl0/(fc*d0)]))-zl0*betae*(((1+Exp[-zl0/d0])/2)-psi1*
        (1-Exp[-zl0/d0]))


(*=========================================================================
        This routine calculates the potential energy of a lithospheric
        column by integrating the vertical stress {sigma} within that
        column, given a particular density distribution.

        It then calculates the buoyancy force caused by the
        potential energy contrast between the deformed and
        reference lithospheric columns.

        sigmazl is the vertical stress at the base of the reference lith;
        p5 is the excess potential energy (see text).

        fbuoyancyt calculates the buoyancy force for a thickened
        lithosphere.
-------------------------------------------------------------------------*)
        sigmac := g*Integrate[rhoc, z]
        sigmaml:= g*Integrate[rhoc,{z,h,zc+h}]+g*Integrate[rhom,z]-
                        g*Integrate[rhom, {z,h,zc+h}]

fbuoyancy:=
        NModule[{},
                sigmacc:=N[sigmac /. {z->zz} /. tconds1 /. crustref];
                sigmamlm:=N[sigmaml /. {z->zz} /. tconds1 /. crustref];
                sigmacd:=N[sigmac /. {z->zz-h} /. tconds2 /. crustdef];
                sigmamld:=N[sigmaml /. {z->zz-h} /. tconds2 /. mantledef];
                p1=N[Integrate[sigmacd,{zz,h,0}] /. {h->-elev /. tconds2}];
                p2=N[Integrate[sigmacd,{zz,0,zc+h}]-
                        Integrate[sigmacc,{zz,0,zc+h}] /. {zc->zc0,
                        h->-elev /. tconds2}];
                p3=N[Integrate[sigmamld,{zz,zc+h,zc}]-
                        Integrate[sigmacc,{zz,zc+h,zc}] /.
                        {zc->zc0, h->-elev /. tconds2}];
                p4=N[Integrate[sigmamld,{zz,zc,zl+h}]-
                        Integrate[sigmamlm,{zz,zc,zl+h}] /.
                        {zc->zc0,zl->zl0-zdelam, h->-elev /. tconds2}];
                sigmazl:=sigmamlm /. {zz->zl0};
                sigmazld:=sigmaml /. tconds2 /. mantledef /.
                        {z->zl0-zdelam};
                        jj:=N[(zdelam-h) /. crustdef];
                        term1:=N[jj*sigmazl];
                        term2:=N[0.5*(sigmazl-sigmazld)*jj];
                        term3:=N[Integrate[sigmamlm,{zz,zl+h,zl0}]
                                /. {h->-elev /. tconds2,zl->zl0-zdelam}];
                p5=N[term1-term2-term3];
                fbuoy = N[p1+p2+p3+p4+p5],
        6]


fbuoyancyt:=
        NModule[{},
                sigmazc1:=N[g*Integrate[rhoc,{z,0,zc0}] /. tconds1 /.
                        crustref];
                sigmazc2:=N[g*Integrate[rhoc,{z,0,zc2}] /. tconds2 /.
                        crustdef];
                sigmamlt1:=N[sigmazc1+
                        g*Integrate[rhom,z]-sigmazc1];
                sigmamlt2:=N[sigmazc2+
                        g*Integrate[rhom,z]-sigmazc2];
                sigmacc:=N[sigmac /. {z->zz} /. tconds1 /. crustref];
                sigmamlm:=N[sigmamlt1 /. {z->zz} /. tconds1 /. crustref];
                sigmacd:=N[sigmac /. {z->zz-h} /. tconds2 /. crustdef];
                sigmamld:=N[sigmamlt2 /. {z->zz-h} /. tconds2 /. mantledef];
                p1=N[Integrate[sigmacd,{zz,h,0}] /. {h->-elev /. tconds2}];
                p2t=N[Integrate[sigmacd,{zz,0,zc0}]-
                        Integrate[sigmacc,{zz,0,zc0}] /. {zc->zc2,
```

```
                h->-elev /. tconds2}];
        p3t=N[Integrate[sigmacd,{zz,zc0,zc2+h}]-
                Integrate[sigmamlm,{zz,zc0,zc2+h}] /. {zc->zc2,
                h->-elev /. tconds2}];
        p4t=N[Integrate[sigmamld,{zz,zc2+h,zl0}]-
                Integrate[sigmamlm,{zz,zc2+h,zl0}] /.
                {zc->zc2,h->-elev /. tconds2}];
        sigmazl:=sigmamlm /. {zz->zl0};
        sigmazldt:=sigmamlt2 /. {z->zl2} /. tconds2 /. mantledef;
        p5t=N[Integrate[sigmamld,{zz,zl0,zl2+h}]-
                sigmazl*(zl2-h-zl0)-0.5*(sigmazldt-sigmazl)*
                (zl2-h-zl0) /. {h->-elev /. tconds2}];
        fbuoy = N[p1+p2t+p3t+p4t+p5t],
    6]


(*=====================================================================
    These relationships define the brittle, ductile and plastic
    maximum deviatoric stress envelopes in the lithosphere.

    dsbrittle defines the brittle stress envelope according to
            Byerlee's law;
    dsductile1 defines the ductile stress envelope according to
            the Power Creep Law (for s1-s3<200MPa);
    dsducitle2 defines the plastic stress envelope according to
            the Dorn Creep Law (for s1-s3>200MPa).
---------------------------------------------------------------------*)

dsbrittle := 2*(sigma0*10^6+mu*sigmaz*(1-lambda))/(Sqrt[mu^2+1]-mu)

dsductile1 := 10^6*((epsdot/ap)^(1/n))*E^(qp/(n*r*(t+273))) /. {epsdot->eee}

dsductile2 := sigmad*(1 - Sqrt[(r*(t+273)*Log[epsdotd/epsdot])/qd])

dsbrittlex := 2*(sigma0*10^6+mu*sigmaz*(1-lambda))/(Sqrt[mu^2+1]+mu)


(*=====================================================================
    This routine calculates the brittle-ductile transition depth,
    {zbdc}, and the strength of the undeformed (reference) crust.
    {cstrengthref} calculates the compressional strength of the crust.
    {cstrengthrefx} calculates the extensional strength of the crust.

    strcrust is the strength of the crust;
    tbdc is the temperature at the brittle-ductile transition;
    tm is the temnperature at the moho;
    x1, x2, y1, y2 & tauc are all calulation parameters.
---------------------------------------------------------------------*)

cstrengthref:=
    NModule[{i,j,diff,diff2,x1,x2,y1,y2},
            z=.;
            dcbrit=dsbrittle /. crustref /. {sigmaz->sigmac /.
                    tconds1 /. crustref};
            dcduct=dsductile1 /. crustref /. tconds1;
            For[i=5000; diff=N[dcduct-dcbrit /. {z->i}], diff>0,
                    i += 500, diff=N[dcduct-dcbrit /. {z->i}]];
            For[j=i-1000; diff2=N[dcduct-dcbrit /. {z->i-1000}], diff2>0,
                    j += 2, diff2=N[dcduct-dcbrit /. {z->j}]];
            zbdc=j;
            x1:=qp/(n*r*(tbdc+273)) /. crustref;
            x2:=qp/(n*r*(tm+273)) /. crustref;
            y1:=(1/(x1^2))+(2/(x1^3))+(6/(x1^4));
            y2:=(1/(x2^2))+(2/(x2^3))+(6/(x2^4));
            tauc:=(tm-tbdc)/(zc-zbdc) /. crustref /. tconds1;
            tbdc:=te /. {z->zbdc} /. tconds1;
            strcrust=N[10^6*((epsdot/ap)^(1/n))*
                    Exp[qp/(n*r*(tbdc+273))]*(0.5*zbdc+(qp/(n*r*tauc))*
                    (y1-y2*Exp[x2-x1])) /. crustref /. {z->zbdc}],
    6]


cstrengthrefx:=
    NModule[{i,j,diff,diff2,taum,x1,x2,y1,y2,tauc},
            z=.;
            dcbritx=dsbrittlex /. crustref /.
                    {sigmaz->sigmac /. tconds1 /. crustref};
            dcductx=dsductile1 /. crustref /. tconds1;
            For[i=5000; diff=N[dcductx-dcbritx /. {z->i}],
                    diff>0, i += 500, diff=N[dcductx-dcbritx
                    /. {z->i}]];
            For[j=i-1000; diff2=N[dcductx-dcbritx /. {z->i-1000}],
```

```
                diff2>0, j += 2, diff2=N[dcductx-dcbritx
                /. {z->j}]];
        zbdcx=j;
                x1:=qp/(n*r*(tbdcx+273)) /. crustref;
                x2:=qp/(n*r*(tm+273)) /. crustref;
                y1:=(1/(x1^2))+(2/(x1^3))+(6/(x1^4));
                y2:=(1/(x2^2))+(2/(x2^3))+(6/(x2^4));
                tauc:=(tm-tbdcx)/(zc-zbdcx) /. crustref
                        /. tconds1;
                tbdcx:=te /. {z->zbdcx} /. tconds1;
        strcrustx=N[10^6*((epsdot/ap)^(1/n))*
                Exp[qp/(n*r*(tbdcx+273))]*(0.5*zbdcx+
                (qp/(n*r*tauc))*(y1-y2*Exp[x2-x1]))
                /. crustref /. {z->zbdcx}],
6]


(*=============================================================
        This routine calculates the depth to the brittle-ductile
        transition in the undeformed mantle lithosphere, {zbdm},
        and the depth to the Power-Dorn creep transition.

        tbdm is the temperature at the brittle-ductile transition;
        ztrans is the depth to the Power-Dorn creep transition;
        transition {ztrans} in the undeformed mantle lithosphere;
        epsdotd is calculated to make the Power-Dorn transition smooth;
        ttrans is the temperature at the Power-Dorn transition.
-------------------------------------------------------------------*)

mtransref:=
        NModule[{i,j,k,diff,max,max2},
                z=.;
                dmbrit=Z*(sigma0+mu*g*(Integrate[rhoc,{z,h,zc0+h}]+
                        Integrate[rhom,{z,zc0+h,z}])*(1-lambda))/
                        (Sqrt[mu^2+1]-mu) /. tconds1 /. mantleref;
                dmduct=dsductile1 /. mantleref /. tconds1;
                dmductd=dsductile2 /. mantleref /. tconds1;
                ttrans=N[qp/(n*r*Log[200/((epsdot/ap)^(1/n))]) /.
                        mantleref];
                epsdotd=N[epsdot*Exp[qd*(1-(2/85))^2/(r*ttrans)] /.
                        mantleref];
                For[i=zc0; diff=N[dmductd-dmbrit /. {z->i}], diff>0,
                        i += 2, diff=N[dmductd-dmbrit /. {z->i}]];
                zbdm=i;
                tbdm:=N[te /. tconds1 /. {z->zbdm}];
                For[j=zbdm; max=N[dmduct /. {z->j}], max>200*10^6,
                        j += 500, max=N[dmduct /. {z->j}]];
                For[k=j-1500; max2=N[dmduct /. {z->j-1500}], max2>200*10^6,
                        k += 2, max2=N[dmduct /. {z->k}]];
                ztrans=k,
        6]


mtransrefx:=
        NModule[{i,diff,j,k,max},
                z=.; epsdotd=.;
                dmbritx=dsbrittlex /. tconds1 /. mantleref;
                dmductx=dsductile1 /. mantleref /. tconds1;
                dmductdx=dsductile2 /. mantleref /. tconds1;
                ttransx=N[qp/(n*r*Log[200/((epsdot/ap)^(1/n))])
                        /. mantleref];
                epsdotd=N[epsdot*Exp[qd*(1-2/85)^2/(r*ttransx)]
                        /. mantleref];
                For[i=zc0; diff=N[dmductdx-dmbritx /. {z->i}],
                        diff>0, i += 2, diff=N[dmductdx-dmbritx /.
                        {z->i}]];
                zbdmx=i;
                tbdmx=N[te /. tconds1 /. {z->zbdmx}];
                For[j=zbdmx; max=N[dmductx /. {z->j}], max>200*10^6,
                        j += 2, max=N[dmductx /. {z->j}]];
                ztransx=j,
        6]


(*=============================================================
        These routines calculate the integrated strength of the
        mantle lithosphere, {mlstrength}.

        f1 is the strength of the brittle part of the mantle lith;
        f2 is the strength of the ductile part of the mantle lith
           calculated using the Dorn Creep Law;
        f3 is the strength of the ductile part of the lower mantle
```

```
          lith calculated using the Power Creep Law;
        taum, x3, x4, y3 & y4 are calculation parameters.
-------------------------------------------------------------------------*)

mstrengthref:=
        NModule[{taum,x3,x4,y3,y4},
                Evaluate[mtransref];
                f1:=N[NIntegrate[dmbrit /. mantleref, {z,zc0,zbdm}]];
                f2:=N[NIntegrate[dmductd /. mantleref,{z,zbdm,ztrans}]];
                f3:=N[NIntegrate[dmduct /. mantleref,{z,ztrans,zl0}]];
                (*taum:=N[(tl-tm)/(zl0-zc) /. mantleref /. tconds1];
                f2:=N[sigmad*(ztrans-zbdm)-(2*sigmad/(3*taum))*(ttrans*
                        Sqrt[r*ttrans*Log[epsdotd/epsdot]/qd]-(tbdm+273)
                        *Sqrt[r*(tbdm+273)*Log[epsdotd/epsdot]/qd])
                        /. mantleref];
                x3:=qp/(n*r*ttrans) /. mantleref;
                x4:=qp/(n*r*(tl+273)) /. mantleref;
                y3:=(1/x3^2)+(2/x3^3)+(6/x3^4);
                y4:=(1/x4^2)+(2/x4^3)+(6/x4^4);
                f3:=N[10^6*(epsdot/ap)^(1/n)*Exp[qp/(n*r*ttrans)]*
                        (qd/(n*r*taum))*(y3-Exp[x4-x3]*y4) /. mantleref];*)
                mlstrength=N[f1+f2+f3],
        6]


mstrengthrefx:=
        NModule[{x2,x4,y3,y4,taum},
                Evaluate[mtransrefx];
                f1x:=N[NIntegrate[dmbritx /. mantleref,
                        {z,zc0,zbdmx}]];
                        taum:=(tl-tm)/(zl0-zc0) /. mantleref /. tconds1;
                f2x:=NIntegrate[dmductdx,{z,zbdmx,ztransx}];
                        zl=zl0-zdelam;
                f3x:=NIntegrate[dmductx,{z,ztransx,zl}];
                mlstrengthx=N[f1x+f2x+f3x],
        6]


(*=========================================================================
        The following routine evaluates the total strength of the
        reference lithosphere.
-------------------------------------------------------------------------*)

comp1:=
        NModule[{},
                Evaluate[cstrengthref];
                Evaluate[mstrengthref];
                lstrength=N[mlstrength+strcrust],
        6]


(*=========================================================================
        The following routine evaluates the brittle-ductile trans-
        ition depth and the strength of the deformed (delaminated)
        crust.

        NOTE that the parameters relevant to this calculation have
        been calculated for the scenario where the crust has been
        heated by the elevated mantle material (ie. the geothermal
        gradient has reached a new steady state).

        Here,   zbdcd is the depth to brit-duct transition;
                tbdcd is the temperature at zbdcd;
                tmd is the temperature at the moho;
                x1,x2,y1,y2 & tauc are calculational parameters;
                strcrustd is the strength of the 'deformed' crust.
-------------------------------------------------------------------------*)

cstrengthdef:=
        NModule[{i,j,diff,diff2,taum,x1,x2,y1,y2,tauc},
                z=.;
                dcbritdef=dsbrittle /. crustdef /.
                        {sigmaz->sigmac /. tconds2 /. crustdef};
                dcductdef=dsductile1 /. crustdef /. tconds2;
                For[i=5000; diff=N[dcductdef-dcbritdef /. {z->i}],
                        diff>0, i += 500, diff=N[dcductdef-dcbritdef
                        /. {z->i}]];
                For[j=i-1000; diff2=N[dcductdef-dcbritdef /. {z->i-1000}],
                        diff2>0, j += 2, diff2=N[dcductdef-dcbritdef
                        /. {z->j}]];
                zbdcdef=j;
                        x1:=qp/(n*r*(tbdcdef+273)) /. crustdef;
```

```
                        x2:=qp/(n*r*(tm+273)) /. crustdef;
                        y1:=(1/(x1^2))+(2/(x1^3))+(6/(x1^4));
                        y2:=(1/(x2^2))+(2/(x2^3))+(6/(x2^4));
                        tauc:=(tm-tbdcdef)/(zc-zbdcdef) /. crustdef
                                /. tconds2;
                        tbdcdef:=te /. {z->zbdcdef} /. tconds2;
                strcrustdef=N[10^6*((epsdot/ap)^(1/n))*
                        Exp[qp/(n*r*(tbdcdef+273))]*(0.5*zbdcdef+
                        (qp/(n*r*tauc))*(y1-y2*Exp[x2-x1]))
                        /. crustdef /. {z->zbdcdef}],
        6]


(*=================================================================
        This routine evalutes the depths to the brittle-ductile
        and Power-Dorn transition in the deformed mantle
        lithosphere {zbdmdef, ztransdef}.
-----------------------------------------------------------------*)

mtransdef:=
        NModule[{i,diff,j,k,max,max2},
                z=.; epsdotd=.;
                dmbritdef=2*(sigma0+mu*g*(Integrate[rhoc,{z,h,zc0+h}]+
                        Integrate[rhom,{z,zc0+h,z}])*(1-lambda))/
                        (Sqrt[mu^2+1]-mu) /. tconds2 /. mantledef;
                dmductdef=dsductile1 /. mantledef /. tconds2;
                dmductddef=dsductile2 /. mantledef /. tconds2;
                ttransdef=N[qp/(n*r*Log[200/((epsdot/ap)^(1/n))])
                        /. mantledef];
                epsdotd=N[epsdot*Exp[qd*(1-2/85)^2/(r*ttransdef)]
                        /. mantledef];
                For[i=zc0; diff=N[dmductddef-dmbritdef /. {z->i}],
                        diff>0, i += 2, diff=N[dmductddef-dmbritdef /.
                        {z->i}]];
                zbdmdef=i;
                tbdmdef=N[te /. tconds2 /. {z->zbdmdef}];
                For[j=zbdmdef; max=N[dmductdef /. {z->j}], max>200*10^6,
                        j += 2, max=N[dmductdef /. {z->j}]];
                ztransdef=j,
        6]


(*=================================================================
        These routines calculate the integrated strength of the
        deformed mantle lithosphere, {mlstrengthdef}.

        f1d is the strength of the brittle part of the mantle lith;
        f2d is the strength of the ductile part of the mantle lith
            calculated using the Dorn Creep Law;
        f3d is the strength of the ductile part of the lower mantle
            lith calculated using the Power Creep Law;
        taum, x3, x4, y3 & y4 are calculation parameters.
-----------------------------------------------------------------*)

mstrengthdef:=
        NModule[{x2,x4,y3,y4,taum},
                Evaluate[mtransdef];
                f1d:=N[NIntegrate[dmbritdef /. mantledef,
                        {z,zc0,zbdmdef}]];
                        taum:=(tl-tm)/(zl0-zc0) /. mantledef /. tconds2;
                f2d:=NIntegrate[dmductddef,{z,zbdmdef,ztransdef}];
                        zl=zl0-zdelam;
                f3d:=NIntegrate[dmductdef,{z,ztransdef,zl}];
                mlstrengthdef=N[f1d+f2d+f3d],
        6]


(*=================================================================
        This routine calculates the extensional strength of the deformed
        crust.
-----------------------------------------------------------------*)

cstrengthdefx:=
        NModule[{i,j,diff,diff2,taum,x1,x2,y1,y2,tauc},
                z=.;
                dcbritdefx=dsbrittlex /. crustdef /.
                        {sigmaz->sigmac /. tconds2 /. crustdef};
                dcductdefx=dsductile1 /. crustdef /. tconds2;
                For[i=5000; diff=N[dcductdefx-dcbritdefx /. {z->i}],
                        diff>0, i += 500, diff=N[dcductdefx-dcbritdefx
                        /. {z->i}]];
                For[j=i-1000; diff2=N[dcductdefx-dcbritdefx /. {z->i-1000}],
```

```
                diff2>0, j += 2, diff2=N[dcductdefx-dcbritdefx
                /. {z->j}]];
        zbdcdefx=j;
                x1:=qp/(n*r*(tbdcdefx+273)) /. crustdef;
                x2:=qp/(n*r*(tm+273)) /. crustdef;
                y1:=(1/(x1^2))+(2/(x1^3))+(6/(x1^4));
                y2:=(1/(x2^2))+(2/(x2^3))+(6/(x2^4));
                tauc:=(tm-tbdcdefx)/(zc-zbdcdefx) /. crustdef
                        /. tconds2;
                tbdcdefx:=te /. {z->zbdcdefx} /. tconds2;
        strcrustdefx=N[10^6*((epsdot/ap)^(1/n))*
                Exp[qp/(n*r*(tbdcdefx+273))]*(0.5*zbdcdefx+
                (qp/(n*r*tauc))*(y1-y2*Exp[x2-x1]))
                /. crustdef /. {z->zbdcdefx}],
    6]


(*=============================================================
    This routine calculates the various transitions appropriate to
    the extensional strength calculations of the mantle lithosphere.
-------------------------------------------------------------------*)

mtransdefx:=
    NModule[{i,diff,j,k,max},
        z=.; epsdotd=.;
        dmbritdefx=2*(sigma0+mu*g*(Integrate[rhoc,{z,h,zc0+h}]+
            Integrate[rhom,{z,zc0+h,z}])*(1-lambda))/
            (Sqrt[mu^2+1]+mu) /. tconds2 /. mantledef;
        dmductdefx=dsductile1 /. mantledef /. tconds2;
        dmductddefx=dsductile2 /. mantledef /. tconds2;
        ttransdefx=N[qp/(n*r*Log[200/((epsdot/ap)^(1/n))])
            /. mantledef];
        epsdotd=N[epsdot*Exp[qd*(1-2/85)^2/(r*ttransdefx)]
            /. mantledef];
        For[i=zc0; diff=N[dmductddefx-dmbritdefx /. {z->i}],
            diff>0, i += 2, diff=N[dmductddefx-dmbritdefx /.
            {z->i}]];
        zbdmdefx=i;
        tbdmdefx=N[te /. tconds2 /. {z->zbdmdefx}];
        For[j=zbdmdefx; max=N[dmductdefx /. {z->j}], max>200*10^6,
            j += 2, max=N[dmductdefx /. {z->j}]];
        ztransdefx=j,
    6]


(*=============================================================
    This routine calculates the extensional strength of the
    deformed mantle lithosphere.
-------------------------------------------------------------------*)

mstrengthdefx:=
    NModule[{x2,x4,y3,y4,taum},
        Evaluate[mtransdefx];
        f1dx:=N[NIntegrate[dmbritdefx /. mantledef,
            {z,zc0,zbdmdefx}]];
            taum:=(tl-tm)/(zl0-zc0) /. mantledef /. tconds2;
        f2dx:=NIntegrate[dmductddefx,{z,zbdmdefx,ztransdefx}];
            zl=zl0-zdelam;
        f3dx:=NIntegrate[dmductdefx,{z,ztransdefx,zl}];
        mlstrengthdefx=N[f1dx+f2dx+f3dx],
    6]

(*=============================================================
    These routines evaulate the compressional and extensional
    strengths of the deformed lithosphere.
-------------------------------------------------------------------*)

comp2:=
    NModule[{},
        Evaluate[cstrengthdef];
        Evaluate[mstrengthdef],
    6]


comp2x:=
    NModule[{},
        Evaluate[cstrengthdefx];
        Evaluate[mstrengthdefx],
    6]


(*=============================================================
```

```
        This routine calculates the possible force caused by a
        density defect between the cold, dense delaminating slab
        and the hot asthenosphere.  It is derived from Turcotte &
        Schubert [1983].

        fspull is the net slab-pull force;
        kappa is the diffusivity;
        bv is the vertical length of the subducting slab;
        bh is the horizontal length of the subducting slab;
        mu0 is the mean horizontal velocity of the system.
-------------------------------------------------------------------------*)

fspull:=2*roml*g*alpha*bv*(tl-ts)*Sqrt[kappa*bh/(2*Pi*mu0)] /. mantleref /.
                {bv->700000,
                 kappa->1*10^-9,
                 mu0->50*10^-3/(365*24*60*60),
                 bh->4000000} /. tconds1


(*=========================================================================
        DATA COMPILATION ROUTINE

        This routine calculates the net effective driving force, fed,
        and compares it with the strength of the deformed lithosphere,
        lstrengthdef.

        zdelam is the thickness of the delaminated slab;
        tmoho is the moho temperature;
        drivingforce is an assumed value less than the reference
                strength of the lithosphere.
-------------------------------------------------------------------------*)

comp3:=
        NModule[{},
                Evaluate[comp1];
                zstep=9375;
                drivingforce=5*10^12 (* has to be less than lstrength *);
                For[zd=0;
                        fld=1.0;
                                fb[fld]=drivingforce-fbi;
                                        lstrengthdef[fld]=
                                                N[strcrust+mlstrength];
                                        tmoho[fld]=N[te /.
                                                {z->zc0,fl->1} /. tconds2];
                                        flsum[fld]=N[strcrust+mlstrength];
                                        elevation[fld]=ei;
                                        zdelam=zd+zstep;
                                        fld=N[(zl0-(zd+zstep))/zl0],
                        zd<zl0-zc0+1,
                        zd += zstep,
                                Evaluate[fbuoyancy];
                                fb[fld]=drivingforce-(fbuoy+fbi);
                                If[fb[fld]<0,
                                        Evaluate[comp2x /. {fl->fld}];
                                        lstrengthdef[fld]=
                                                strcrustdefx+mlstrengthdefx,
                                        Evaluate[comp2 /. {fl->fld}];
                                        lstrengthdef[fld]=
                                                strcrustdef+mlstrengthdef];
                                tmoho[fld]=N[te /. {z->zc0; fl->fld} /.
                                        tconds2];
                                flsum[fld]=fb[fld]+lstrengthdef[fld];
                                elevation[fld]=N[ei+elev /. tconds2 /.
                                        {fl->fld}];
                                fld=N[(zl0-(zd+zstep))/zl0];
                                zdelam=zd+zstep];
                        w=fb[u];
                        x=tmoho[u] /. {z->zc0};
                        y=N[lstrengthdef[u]];
                        s=flsum[u];
                        e=elevation[u];
                Do[ged[1/u]=fb[u],{u,0.3,1,0.05}];
                Do[gtmoho[1/u]=tmoho[u] /. {z->zc0},{u,0.3,1,0.05}];
                Do[gls[1/u]=N[lstrengthdef[u]],{u,0.3,1,0.05}];
                Do[gsum[1/u]=flsum[u],{u,0.3,1,0.05}];
                Do[el[1/u]=elevation[u],{u,0.3,1,0.05}];
                        gw=ged[1/u];
                        gx=gtmoho[1/u];
                        gy=gls[1/u];
                        gyw=gsum[1/u];
                        gel=el[1/u];
                gwlist=Table[{1/u,gw},{u,0.3,1,0.05}];
```

```
        gelist=Table[{1/u,gel},{u,0.3,1,0.05}];
        gxlist=Table[{1/u,gx},{u,0.3,1,0.05}];
        gylist=Table[{1/u,gy},{u,0.3,1,0.05}];
        gywlist=Table[{1/u,gyw},{u,0.3,1,0.05}];
        epslist[epsdot]=Table[{1/u,gyw},{u,0.15,0.6,0.15}];
        wwlist[epsdot]=Table[gw,{u,0.3,1,0.05}];
        yylist[epsdot]=Table[gy,{u,0.3,1,0.05}];
        graphy[epsdot]=ListPlot[gylist,
                PlotJoined->True,
                PlotStyle->Thickness[0.0005],
                DisplayFunction->Identity];
        graphyw[epsdot]=ListPlot[gywlist,
                PlotJoined->True,
                DisplayFunction->Identity,
                PlotStyle->Thickness[0.0005]];
        listcombined[epsdot]=Transpose[{wwlist[epsdot],
                yylist[epsdot]}],
        6]


(*=============================================================================
        This routine calculates lithospheric strength for different
        moho temperatures.
-----------------------------------------------------------------------------*)

comp5:=
        NModule[{},
                tl=.;epsdot=3.16 10^-16;eee=epsdot;
                For[q=1000,
                        q<1501,
                                q += 50,
                        tl=q;
                        tmo[q]=N[te /. tconds1 /. {z->zc0}];
                        Evaluate[cstrengthref];
                        Evaluate[mstrengthref];
                        ls[q]=N[strcrust+mlstrength]];
                ll=ls[qq];
                mm=tmo[qq];
                lllist=Table[ll,{qq,1050,1500,50}];
                mmlist=Table[mm,{qq,1050,1500,50}];
                lmtrans=Transpose[{mmlist,lllist}];
                tempgraph=ListPlot[lmtrans,
                        PlotJoined->True,
                        DisplayFunction->$DisplayFunction,
                        Frame->True,
                        AxesOrigin={375,2 10^13},
                        PlotStyle->Thickness[0.001],
                        PlotLabel->
                        FontForm["Lithospheric strength vs moho temperature",
                                {"Helvetica-Bold",12}]],
        6]


(*=============================================================================
        This routine evaluates the various force balances for different
        strain rates.
-----------------------------------------------------------------------------*)

(*comp7:=
        NModule[{},
                epsdot=10^-17;
                eee=epsdot;
                Evaluate[comp3];
                epsdot=10^-16;
                eee=epsdot;
                Evaluate[comp3];
                epsdot=10^-15;
                eee=epsdot;
                Evaluate[comp3];
                epsdot=10^-14;
                eee=epsdot;
                Evaluate[comp3],
        6]*)


 (*=============================================================================
        This is the FINAL plotting routine.
-----------------------------------------------------------------------------*)

comp9:=
        NModule[{},
                plotdot=RegularPolygon[2,0.00001];
```

```
$DotShapes={MakeSymbol[plotdot]};
plotcombined=MultipleListPlot[
        listcombined[1/1000000000000000000],
        listcombined[1/100000000000000000],
        listcombined[1/10000000000000000],
        listcombined[1/1000000000000000],
        listcombined[1/100000000000000],
        DisplayFunction->Identity,
        PlotJoined->True,
        AxesOrigin->{0,0},
        Frame->True,
        LineStyles->{ {Thickness[0.001]} }];
Evaluate[comp6];
fdvfb=Show[plotcombined,fdcontours,
        DisplayFunction->Identity,
        AxesOrigin->{0,0},
        PlotLabel->
        FontForm["Lithospheric strength vs buoyancy force";
                "(contoured for driving force)",
                {"Helvetica-Bold",12}]];
tmohocombined=ListPlot[gxlist,
        DisplayFunction->Identity,
        PlotJoined->True,
        Frame->True,
        AxesOrigin->{1,400},
        PlotStyle->{ {Thickness[0.001]} },
        PlotLabel->
        FontForm["Moho temperature vs thinning factor",
                {"Helvetica-Bold",12}]];
strengthcombined=Show[graphy[10^-17],
        graphy[10^-16],graphy[10^-15],graphy[10^-14],
        DisplayFunction->Identity,
        Frame->True,
        PlotLabel->
        FontForm["Lithospheric strength vs thinning factor",
                {"Helvetica-Bold",12}]];
elevationcombined=ListPlot[gelist,
        DisplayFunction->Identity,
        PlotJoined->True,
        Frame->True,
        PlotStyle->{ {Thickness[0.001]} },
        PlotLabel->
        FontForm["Surface elevation vs thinning factor",
                {"Helvetica-Bold",12}]];
fbuoycombined=ListPlot[gwlist,
        DisplayFunction->Identity,
        PlotJoined->True,
        Frame->True,
        PlotStyle->{ {Thickness[0.001]} },
        PlotLabel->
        FontForm["Buoyancy force vs thinning factor",
                {"Helvetica-Bold",12}]];
fdcombined=Show[graphyw[10^-17],
        graphyw[10^-16],graphyw[10^-15],
        graphyw[10^-14],
        DisplayFunction->Identity,
        Frame->True,
        PlotLabel->
        FontForm["Driving force required for deformation vs thinning factor",
                {"Helvetica-Bold",12}]];
(*Evaluate[comp8];
epsdotcombined=MultipleListPlot[epslist1,epslist2,
        epslist3,epslist4,
        DisplayFunction->$DisplayFunction,
        PlotJoined->True,
        Frame->True,
        LineStyles->{ {Thickness[0.001]} },
        FrameLabel->{"strain rate","driving force",
                " "," "},
        PlotLabel->
        FontForm["Driving force required for deformation vs strain rate",
                {"Helvetica-Bold",12}]];*)
figure1=Show[GraphicsArray[{{elevationcombined},
                        {tmohocombined},
                        {fbuoycombined}}],
                        DisplayFunction->$DisplayFunction];
figure2=Show[GraphicsArray[{{strengthcombined},
                        {fdvfb},
                        {fdcombined}}],
                        DislpayFunction->$DisplayFunction],
```

```
(*-------------------------------------------------------------------------
        STRENGTH ENVELOPE PLOTTING ROUTINE
-------------------------------------------------------------------------*)

strengthenv:=
        NModule[{},
                p1=Plot[dcbrit,{z,0,zbdc},DisplayFunction->Identity];
                p2=Plot[-dcbritx,{z,0,zbdcx},DisplayFunction->Identity];
                p3=Plot[dcduct,{z,zbdc,zc0},DisplayFunction->Identity];
                p4=Plot[-dcductx,{z,zbdcx,zc0},DisplayFunction->Identity];
                p5=Plot[dmbrit,{z,zc0,zbdm},DisplayFunction->Identity];
                p6=Plot[-dmbritx,{z,zc0,zbdmx},DisplayFunction->Identity];
                p7=Plot[dmductd,{z,zbdm,ztrans},DisplayFunction->Identity];
                p8=Plot[-dmductdx,{z,zbdmx,ztransx},DisplayFunction->Identity];
                p9=Plot[dmduct,{z,ztrans,zl0},DisplayFunction->Identity];
                p10=Plot[-dmductx,{z,ztransx,zl0},DisplayFunction->Identity];
                Show[p1,p2,p3,p4,p5,p6,p7,p8,p9,p10,
                                Frame->True,
                                AxesOrigin->{0,0},
                                DisplayFunction->$DisplayFunction,
                                PlotRange->{-1.43*10^9,1.43*10^9}],
        4]
```

# Appendix 3

## Ion microprobe data and geothermometry

## 1 Ion microprobe data

Analysis was carried out using a Jeol 733 Ion Microprobe and a KEVEX 7000 Series Analyser at CEMMSA, University of Adelaide. Results were recalculated using RECALC, a simple computer program that calculates molar weight and mineral proportions from raw microprobe data [Powell & Holland, 1990].

Probe data included for samples:A1017-JPT010, 033, 078, 081, 084, 092, 096, 108, 115.

A1017-JPT010 GARNET-BIOTITE SCHIST
Freeling Heights Metasediments
Not recalculated: quartz
garnet: almandine

| | SiO2 | TiO2 | Al2O3 | FeO | MnO | MgO | CaO |
|---|---|---|---|---|---|---|---|
| | 36.54 | 0.09 | 21.82 | 24.24 | 13.24 | 2.95 | 2.17 |
| sd | 0.42 | 0.05 | 0.27 | 0.29 | 0.18 | 0.08 | 0.07 |

| | K2O | Total |
|---|---|---|
| | 0.08 | 101.13 |
| sd | 0.05 | 0.61 |

| | Si | Ti | Al | Fe2 | Mn | Mg | Ca |
|---|---|---|---|---|---|---|---|
| | 2.92 | 0.01 | 2.06 | 1.62 | 0.90 | 0.35 | 0.19 |
| sd | 0.02 | 0.00 | 0.02 | 0.02 | 0.01 | 0.01 | 0.01 |

| | K |
|---|---|
| | 0.01 |
| sd | 0.01 |

| | x(Si,T1) | x(Al,M1) |
|---|---|---|
| | 0.974 | 1.000 |
| sd | 0.007 | 0 |

| | x(Ca,M2) | x(Fe2,M2) | x(Mg,M2) |
|---|---|---|---|
| | 0.062 | 0.540 | 0.117 |
| sd | 0.002 | 0.007 | 0.003 |

| | x | sd(x) | % |
|---|---|---|---|
| x(gr) | 0.000219 | 0.0000217 | 9.9 |
| x(py) | 0.00149 | 0.000118 | 7.9 |
| x(alm) | 0.146 | 0.00491 | 3.4 |

biotite

| | SiO2 | TiO2 | Al2O3 | Fe2O3 | FeO | MnO | MgO | NiO | CaO |
|---|---|---|---|---|---|---|---|---|---|
| | 35.43 | 1.87 | 18.22 | 2.54 | 12.97 | 0.18 | 12.65 | 0.05 | 0.09 |
| sd | 0.40 | 0.07 | 0.23 | 1.70 | 1.54 | 0.05 | 0.18 | 0.05 | 0.05 |

| | K2O | H2O | Total |
|---|---|---|---|
| | 9.66 | 3.95 | 97.60 |
| sd | 0.15 | 0.03 | 0.62 |

| | Si | Ti | Al | Fe3 | Fe2 | Mn | Mg | Ni | Ca |
|---|---|---|---|---|---|---|---|---|---|
| | 2.69 | 0.11 | 1.63 | 0.15 | 0.82 | 0.01 | 1.43 | 0.00 | 0.01 |
| sd | 0.02 | 0.00 | 0.02 | 0.10 | 0.10 | 0.00 | 0.02 | 0.00 | 0.00 |

| | K | OH |
|---|---|---|
| | 0.94 | 2.00 |
| sd | 0.02 | 0 |

| | x(Si,T1) | x(Al,T1) | x(Si,T2) | x(Al,M1) | x(Fe2,M1) | x(Mg,M1) | x(Fe3,M1) |
|---|---|---|---|---|---|---|---|
| | 0.345 | 0.655 | 1.000 | 0.160 | 0.259 | 0.449 | 0.073 |
| sd | 0.011 | 0.011 | 0 | 0.012 | 0.033 | 0.008 | 0.048 |

| | x(Fe2,M2) | x(Mg,M2) | x(v,M2) | x(Ca,A) | x(K,A) |
|---|---|---|---|---|---|
| | 0.306 | 0.532 | 0.162 | 0.007 | 0.936 |
| sd | 0.035 | 0.010 | 0.033 | 0.004 | 0.016 |

| | x | sd(x) | % |
|---|---|---|---|
| x(phl) | 0.0908 | 0.00446 | 4.9 |
| x(ann) | 0.0173 | 0.00664 | 38.3 |
| x(east) | 0.0616 | 0.00413 | 6.7 |

muscovite (late growth - ?retrograde)

| | SiO2 | Al2O3 | Fe2O3 | FeO | MnO | CaO |
|---|---|---|---|---|---|---|
| | 43.58 | 33.87 | 1.02 | 0.61 | 0.04 | 0.11 |
| sd | 0.49 | 0.39 | 0.34 | 0.31 | 0.05 | 0.05 |

| | Na2O | K2O | H2O | Total |
|---|---|---|---|---|
| | 0.11 | 10.77 | 4.25 | 94.36 |
| sd | 0.05 | 0.16 | 0.03 | 0.68 |

| | Si | Al | Fe3 | Fe2 | Mn | Ca |
|---|---|---|---|---|---|---|
| | 3.08 | 2.82 | 0.05 | 0.04 | 0.00 | 0.01 |
| sd | 0.02 | 0.03 | 0.02 | 0.02 | 0.00 | 0.00 |

| | Na | K | OH |
|---|---|---|---|
| | 0.01 | 0.97 | 2.00 |
| sd | 0.01 | 0.02 | 0 |

| | x(Si,T1) | x(Al,T1) | x(Si,T2) | x(Al,M1) | x(Fe2,M1) | x(Fe3,M1) |
|---|---|---|---|---|---|---|
| | 0.538 | 0.462 | 1.000 | 0.947 | 0.018 | 0.027 |
| sd | 0.010 | 0.010 | 0 | 0.005 | 0.009 | 0.009 |

| | x(v,M2) | x(Ca,A) | x(Na,A) | x(K,A) |
|---|---|---|---|---|
| | 0.998 | 0.008 | 0.015 | 0.969 |
| sd | 0.003 | 0.004 | 0.007 | 0.015 |

| | x | sd(x) | % |
|---|---|---|---|
| x(mu) | 0.863 | 0.0157 | 1.8 |
| x(pa) | 0.0132 | 0.00619 | 47.0 |
| x(ma) | 0.00153 | 0.000742 | 48.4 |

ilmenite

| | SiO2 | TiO2 | Al2O3 | FeO | MnO | MgO | CaO |
|---|---|---|---|---|---|---|---|
| | 0.63 | 51.89 | 0.24 | 40.85 | 2.38 | 0.15 | 0.02 |
| sd | 0.06 | 0.57 | 0.05 | 0.46 | 0.07 | 0.05 | 0.05 |

| | Na2O | Total |
|---|---|---|
| | 0.09 | 96.25 |
| sd | 0.05 | 0.74 |

| | Si | Ti | Al | Fe2 | Mn | Mg | Ca |
|---|---|---|---|---|---|---|---|
| | 0.02 | 1.01 | 0.01 | 0.88 | 0.05 | 0.01 | 0.00 |
| sd | 0.00 | 0.01 | 0.00 | 0.01 | 0.00 | 0.00 | 0.00 |

| | Na |
|---|---|
| | 0.00 |
| sd | 0.00 |

## A1017-JPT033 OLIVINE GRANULITE

## Mt Adams Valley Mélange

## Olivine - forsterite (symplectite reactant)

| | SiO2 | TiO2 | FeO | MnO | MgO |
|---|---|---|---|---|---|
| | 38.72 | 0.17 | 17.61 | 0.30 | 42.45 |
| sd | 0.44 | 0.05 | 0.23 | 0.05 | 0.47 |

| | Total |
|---|---|
| | 99.26 |
| sd | 0.69 |

| | Si | Ti | Fe2 | Mn | Mg |
|---|---|---|---|---|---|
| | 0.99 | 0.00 | 0.38 | 0.01 | 1.62 |
| sd | 0.01 | 0.00 | 0.01 | 0.00 | 0.01 |

| | x(Si,T1) | x(Fe2,M1) | x(Mg,M1) |
|---|---|---|---|
| | 0.993 | 0.189 | 0.811 |
| sd | 0.007 | 0.003 | 0.003 |

| | x(Fe2,M2) | x(Mg,M2) |
|---|---|---|
| | 0.189 | 0.812 |
| sd | 0.003 | 0.013 |

| | x | sd(x) | % |
|---|---|---|---|
| x(fo) | 0.658 | 0.0116 | 1.8 |
| x(fa) | 0.0357 | 0.000976 | 2.7 |

## feldspar: anorthite (symplectite reactant)

| | SiO2 | TiO2 | Cr2O3 | Al2O3 | Fe2O3 | MgO | CaO |
|---|---|---|---|---|---|---|---|
| | 48.20 | 0.05 | 0.23 | 30.90 | 0.16 | 0.01 | 14.38 |
| sd | 0.53 | 0.05 | 0.05 | 0.36 | 0.06 | 0.05 | 0.19 |

| | Na2O | Total |
|---|---|---|
| | 3.21 | 97.13 |
| sd | 0.08 | 0.68 |

| | Si | Ti | Cr | Al | Fe3 | Mg | Ca |
|---|---|---|---|---|---|---|---|
| | 2.27 | 0.00 | 0.01 | 1.71 | 0.01 | 0.00 | 0.72 |
| sd | 0.01 | 0.00 | 0.00 | 0.02 | 0.00 | 0.00 | 0.01 |

| | Na |
|---|---|
| | 0.29 |
| sd | 0.01 |

| | x(Si,T1) | x(Al,T1) |
|---|---|---|
| | 0.567 | 0.428 |
| sd | 0.004 | 0.004 |

| | x(Ca,A) | x(Na,A) |
|---|---|---|
| | 0.725 | 0.292 |
| sd | 0.010 | 0.008 |

| | x | sd(x) | % |
|---|---|---|---|
| x(an) | 0.713 | 0.00592 | 0.8 |
| x(ab) | 0.287 | 0.00592 | 2.1 |

## amphibole: kaersutite

| | SiO2 | TiO2 | Cr2O3 | Al2O3 | Fe2O3 | FeO | MnO | MgO | CaO |
|---|---|---|---|---|---|---|---|---|---|
| | 39.04 | 4.20 | 0.22 | 14.59 | 1.35 | 6.89 | 0.03 | 13.28 | 11.91 |
| sd | 0.44 | 0.09 | 0.05 | 0.20 | 0.90 | 0.82 | 0.05 | 0.18 | 0.17 |

| | Na2O | K2O | H2O | Total |
|---|---|---|---|---|
| | 2.05 | 1.95 | 2.00 | 97.52 |
| sd | 0.07 | 0.07 | 0.01 | 0.60 |

| | Si | Ti | Cr | Al | Fe3 | Fe2 | Mn | Mg | Ca |
|---|---|---|---|---|---|---|---|---|---|
| | 5.85 | 0.47 | 0.03 | 2.58 | 0.15 | 0.86 | 0.00 | 2.96 | 1.91 |
| sd | 0.04 | 0.01 | 0.01 | 0.03 | 0.10 | 0.10 | 0.01 | 0.04 | 0.03 |

| | Na | K | OH |
|---|---|---|---|
| | 0.60 | 0.37 | 2.00 |
| sd | 0.02 | 0.01 | 0 |

| | x(Si,T1) | x(Al,T1) | x(Si,T2) | x(Al,M1) | x(Fe2,M1) | x(Mg,M1) |
|---|---|---|---|---|---|---|
| | 0.462 | 0.538 | 1.000 | 0.212 | 0.093 | 0.320 |
| sd | 0.010 | 0.010 | 0 | 0.018 | 0.021 | 0.038 |

| | x(Ca,M2) | x(Na,M2) | x(Fe2,M3) | x(Mg,M3) | x(Na,A) | x(v,A) |
|---|---|---|---|---|---|---|
| | 0.956 | 0.044 | 0.226 | 0.774 | 0.508 | 0.120 |
| sd | 0.014 | 0.014 | 0.021 | 0.021 | 0.035 | 0.039 |

| | x | sd(x) | % |
|---|---|---|---|
| x(tr) | 0.000239 | 0.0000850 | 35.6 |
| x(ftr) | 0.000000500 | 0.000000388 | 77.6 |
| x(hb) | 0.00697 | 0.00247 | 35.5 |
| x(parg) | 0.0578 | 0.00651 | 11.3 |
| x(ed) | 0.0111 | 0.00230 | 20.7 |
| x(gl) | 0.000000223 | 0.000000230 | 103.3 |
| x(fgl) | 5.501108e-9 | 5.800346e-9 | 105.4 |

spinel (symplectite product)

| | Cr2O3 | Al2O3 | Fe2O3 | FeO | MnO | MgO | CaO |
|---|---|---|---|---|---|---|---|
| | 0.03 | 64.17 | 1.88 | 16.05 | 0.08 | 16.74 | 0.11 |
| sd | 0.05 | 0.69 | 0.50 | 0.43 | 0.05 | 0.22 | 0.05 |

| | K2O | Total |
|---|---|---|
| | 0.05 | 99.10 |
| sd | 0.05 | 0.74 |

| | Cr | Al | Fe3 | Fe2 | Mn | Mg | Ca |
|---|---|---|---|---|---|---|---|
| | 0.00 | 1.96 | 0.04 | 0.35 | 0.00 | 0.65 | 0.00 |
| sd | 0.00 | 0.01 | 0.01 | 0.01 | 0.00 | 0.01 | 0.00 |

| | K |
|---|---|
| | 0.00 |
| sd | 0.00 |

clinopyroxene: diopside (symplectite product)

| | SiO2 | TiO2 | Cr2O3 | Al2O3 | Fe2O3 | MgO | CaO |
|---|---|---|---|---|---|---|---|
| | 47.81 | 1.07 | 0.53 | 6.60 | 4.82 | 13.69 | 22.21 |
| sd | 0.53 | 0.06 | 0.06 | 0.12 | 0.10 | 0.19 | 0.27 |

| | Na2O | Total |
|---|---|---|
| | 1.27 | 98.00 |
| sd | 0.06 | 0.65 |

| | Si | Ti | Cr | Al | Fe3 | Mg | Ca |
|---|---|---|---|---|---|---|---|
| | 1.79 | 0.03 | 0.02 | 0.29 | 0.14 | 0.76 | 0.89 |
| sd | 0.01 | 0.00 | 0.00 | 0.01 | 0.00 | 0.01 | 0.01 |

| | Na |
|---|---|
| | 0.09 |
| sd | 0.00 |

| | x(Si,T1) | x(Al,T1) | x(Al,M1) | x(Mg,M1) |
|---|---|---|---|---|
| | 0.894 | 0.106 | 0.079 | 0.755 |
| sd | 0.005 | 0.005 | 0.009 | 0.008 |

| | x(Ca,M2) | x(Na,M2) | x(Mg,M2) |
|---|---|---|---|
| | 0.890 | 0.092 | 0.008 |
| sd | 0.011 | 0.005 | 0.008 |

| | x | sd(x) | % |
|---|---|---|---|
| x(di) | 0.672 | 0.0144 | 2.2 |
| x(cats) | 0.0707 | 0.00713 | 10.1 |

## A1017-JPT078 CALC-SILICATE

Four Mile Creek Gneisses (contact metamorphosed version of A1017-JPT081)

Not recalculated: ilmenite

clinopyroxene: diopside

| | SiO2 | TiO2 | Cr2O3 | Al2O3 | FeO | MnO | MgO | CaO |
|---|---|---|---|---|---|---|---|---|
| | 50.01 | 0.33 | 0.32 | 4.22 | 9.90 | 0.65 | 17.21 | 12.33 |
| sd | 0.55 | 0.05 | 0.05 | 0.09 | 0.15 | 0.06 | 0.22 | 0.17 |

| | K2O | Total |
|---|---|---|
| | 0.14 | 95.10 |
| sd | 0.05 | 0.65 |

| | Si | Ti | Cr | Al | Fe2 | Mn | Mg | Ca |
|---|---|---|---|---|---|---|---|---|
| | 1.92 | 0.01 | 0.01 | 0.19 | 0.32 | 0.02 | 0.99 | 0.51 |
| sd | 0.01 | 0.00 | 0.00 | 0.00 | 0.01 | 0.00 | 0.01 | 0.01 |

| | K |
|---|---|
| | 0.01 |

```
sd   0.00

    x(Si,T1)  x(Al,T1)  x(Al,M1) x(Fe2,M1)  x(Mg,M1)
       0.961     0.039     0.113     0.214     0.663
sd     0.005     0.005     0.009     0.003     0.008

    x(Ca,M2) x(Fe2,M2)  x(Mg,M2)
       0.508     0.104     0.322
sd     0.008     0.002     0.007

                      x       sd(x)       %
        x(di)       0.337     0.00755     2.2
       x(hed)       0.109     0.00279     2.6
      x(cats)      0.0574     0.00401     7.0
```

feldspar: anorthite

```
     SiO2   TiO2  Cr2O3  Al2O3  Fe2O3    MgO    CaO
    42.43   0.23   0.15  35.02   0.15   0.15  19.84
sd   0.47   0.05   0.05   0.40   0.06   0.05   0.25

     Na2O  Total
     0.45  98.43
sd   0.05   0.68

       Si     Ti     Cr     Al    Fe3     Mg     Ca
     2.00   0.01   0.01   1.95   0.01   0.01   1.00
sd   0.01   0.00   0.00   0.02   0.00   0.00   0.01

       Na
     0.04
sd   0.00

    x(Si,T1)  x(Al,T1)
       0.501     0.487
sd     0.004     0.005

     x(Ca,A)   x(Na,A)
       1.000     0.041
sd          0     0.005

                      x       sd(x)       %
        x(an)       0.960     0.00461     0.5
        x(ab)      0.0396     0.00460    11.6
```

A1017-JPT081 CALC-SILICATE

Four Mile Creek Gneisses

Not recalculated: ilmenite

amphibole: cummingtonite

```
     SiO2   TiO2  Cr2O3  Al2O3  Fe2O3    FeO    MnO    MgO    CaO
    53.85   0.05   0.09   0.96   2.92  14.87   1.58  21.75   0.69
sd   0.59   0.05   0.05   0.06   1.94   1.76   0.07   0.27   0.06

      K2O    H2O  Total
     0.01   2.08  98.84
sd   0.05   0.02   0.74

       Si     Ti     Cr     Al    Fe3    Fe2     Mn     Mg     Ca
     7.75   0.01   0.01   0.16   0.32   1.79   0.19   4.67   0.11
sd   0.05   0.01   0.01   0.01   0.21   0.22   0.01   0.06   0.01

        K     OH
     0.00   2.00
sd   0.01      0

    x(Si,T1)  x(Al,T1)  x(Si,T2) x(Fe2,M1)  x(Mg,M1)
       0.938     0.041     1.000     0.233     0.607
sd     0.013     0.003         0     0.049     0.056

    x(Ca,M2) x(Fe2,M2)  x(Mg,M2) x(Fe2,M3)  x(Mg,M3)    x(v,A)
       0.053     0.246     0.642     0.277     0.723     0.998
sd     0.004     0.027     0.027     0.024     0.024     0.009

                      x       sd(x)       %
        x(tr)    0.000300  0.0000644    21.5
       x(ftr)  0.00000249  0.00000185   74.4
```

| | x | sd(x) | % |
|---|---|---|---|
| x(cumm) | 0.0442 | 0.00509 | 11.5 |
| x(grun) | 0.0000540 | 0.0000498 | 92.3 |

feldspar: anorthite

| | SiO2 | TiO2 | Cr2O3 | Al2O3 | Fe2O3 | MgO | CaO |
|---|---|---|---|---|---|---|---|
| | 42.43 | 0.23 | 0.15 | 35.02 | 0.15 | 0.15 | 19.84 |
| sd | 0.47 | 0.05 | 0.05 | 0.40 | 0.06 | 0.05 | 0.25 |

| | Na2O | Total |
|---|---|---|
| | 0.45 | 98.43 |
| sd | 0.05 | 0.68 |

| | Si | Ti | Cr | Al | Fe3 | Mg | Ca |
|---|---|---|---|---|---|---|---|
| | 2.00 | 0.01 | 0.01 | 1.95 | 0.01 | 0.01 | 1.00 |
| sd | 0.01 | 0.00 | 0.00 | 0.02 | 0.00 | 0.00 | 0.01 |

| | Na |
|---|---|
| | 0.04 |
| sd | 0.00 |

| | x(Si,T1) | x(Al,T1) |
|---|---|---|
| | 0.501 | 0.487 |
| sd | 0.004 | 0.005 |

| | x(Ca,A) | x(Na,A) |
|---|---|---|
| | 1.000 | 0.041 |
| sd | 0 | 0.005 |

| | x | sd(x) | % |
|---|---|---|---|
| x(an) | 0.960 | 0.00461 | 0.5 |
| x(ab) | 0.0396 | 0.00460 | 11.6 |

## A1017-JPT084 CALC-SILICATE

Mt Adams Valley Mélange

Not recalculated: sphene, retrograde chlorite and scapolite

feldspar: oligoclase

| | SiO2 | Cr2O3 | Al2O3 | Fe2O3 | MgO | CaO |
|---|---|---|---|---|---|---|
| | 51.44 | 0.14 | 23.08 | 0.10 | 0.09 | 10.10 |
| sd | 0.56 | 0.05 | 0.28 | 0.06 | 0.05 | 0.15 |

| | Na2O | K2O | Total |
|---|---|---|---|
| | 7.49 | 0.58 | 93.03 |
| sd | 0.12 | 0.06 | 0.66 |

| | Si | Cr | Al | Fe3 | Mg | Ca |
|---|---|---|---|---|---|---|
| | 2.53 | 0.01 | 1.34 | 0.00 | 0.01 | 0.53 |
| sd | 0.01 | 0.00 | 0.02 | 0.00 | 0.00 | 0.01 |

| | Na | K |
|---|---|---|
| | 0.71 | 0.04 |
| sd | 0.01 | 0.00 |

| | x(Si,T1) | x(Al,T1) |
|---|---|---|
| | 0.633 | 0.335 |
| sd | 0.003 | 0.004 |

| | x(Ca,A) | x(Na,A) | x(K,A) |
|---|---|---|---|
| | 0.533 | 0.715 | 0.036 |
| sd | 0.008 | 0.013 | 0.004 |

| | x | sd(x) | % |
|---|---|---|---|
| x(an) | 0.415 | 0.00541 | 1.3 |
| x(ab) | 0.557 | 0.00558 | 1.0 |
| x(or) | 0.0284 | 0.00267 | 9.4 |

feldspar: albite

| | SiO2 | TiO2 | Cr2O3 | Al2O3 | Fe2O3 | MnO | MgO | CaO |
|---|---|---|---|---|---|---|---|---|
| | 60.75 | 0.10 | 0.09 | 22.24 | 0.30 | 0.10 | 0.02 | 4.01 |
| sd | 0.66 | 0.05 | 0.05 | 0.27 | 0.06 | 0.05 | 0.05 | 0.09 |

| | Na2O | K2O | Total |
|---|---|---|---|
| | 8.83 | 0.20 | 96.63 |
| sd | 0.14 | 0.05 | 0.74 |

| | Si | Ti | Cr | Al | Fe3 | Mn | Mg | Ca |
|---|---|---|---|---|---|---|---|---|
| | 2.78 | 0.00 | 0.00 | 1.20 | 0.01 | 0.00 | 0.00 | 0.20 |
| sd | 0.01 | 0.00 | 0.00 | 0.01 | 0.00 | 0.00 | 0.00 | 0.00 |

| | Na | K |
|---|---|---|
| | 0.78 | 0.01 |
| sd | 0.01 | 0.00 |

| | x(Si,T1) | x(Al,T1) |
|---|---|---|
| | 0.696 | 0.300 |
| sd | 0.003 | 0.004 |

| | x(Ca,A) | x(Na,A) | x(K,A) |
|---|---|---|---|
| | 0.197 | 0.785 | 0.012 |
| sd | 0.005 | 0.013 | 0.003 |

| | x | sd(x) | % |
|---|---|---|---|
| x(an) | 0.198 | 0.00437 | 2.2 |
| x(ab) | 0.790 | 0.00500 | 0.6 |
| x(or) | 0.0120 | 0.00303 | 25.2 |

## feldspar: orthoclase

| | SiO2 | TiO2 | Cr2O3 | Al2O3 | CaO |
|---|---|---|---|---|---|
| | 60.79 | 0.29 | 0.01 | 18.01 | 0.27 |
| sd | 0.66 | 0.05 | 0.05 | 0.23 | 0.05 |

| | Na2O | K2O | Total |
|---|---|---|---|
| | 0.98 | 14.63 | 94.99 |
| sd | 0.06 | 0.20 | 0.73 |

| | Si | Ti | Cr | Al | Ca |
|---|---|---|---|---|---|
| | 2.96 | 0.01 | 0.00 | 1.03 | 0.01 |
| sd | 0.01 | 0.00 | 0.00 | 0.01 | 0.00 |

| | Na | K |
|---|---|---|
| | 0.09 | 0.91 |
| sd | 0.01 | 0.01 |

| | x(Si,T1) | x(Al,T1) |
|---|---|---|
| | 0.739 | 0.258 |
| sd | 0.003 | 0.003 |

| | x(Ca,A) | x(Na,A) | x(K,A) |
|---|---|---|---|
| | 0.014 | 0.093 | 0.908 |
| sd | 0.003 | 0.006 | 0.014 |

| | x | sd(x) | % |
|---|---|---|---|
| x(an) | 0.0141 | 0.00268 | 19.0 |
| x(ab) | 0.0913 | 0.00517 | 5.7 |
| x(or) | 0.895 | 0.00568 | 0.6 |

## garnet: andradite

| | SiO2 | TiO2 | Cr2O3 | Al2O3 | Fe2O3 | FeO | MnO | MgO | CaO |
|---|---|---|---|---|---|---|---|---|---|
| | 34.32 | 0.73 | 0.58 | 2.84 | 26.20 | 1.47 | 0.51 | 0.24 | 31.63 |
| sd | 0.39 | 0.06 | 0.06 | 0.08 | 0.25 | 0.33 | 0.06 | 0.05 | 0.37 |

| | Na2O | Total |
|---|---|---|
| | 0.21 | 98.73 |
| sd | 0.05 | 0.65 |

| | Si | Ti | Cr | Al | Fe3 | Fe2 | Mn | Mg | Ca |
|---|---|---|---|---|---|---|---|---|---|
| | 2.92 | 0.05 | 0.04 | 0.28 | 1.68 | 0.10 | 0.04 | 0.03 | 2.88 |
| sd | 0.02 | 0.00 | 0.00 | 0.01 | 0.01 | 0.02 | 0.00 | 0.01 | 0.03 |

| | Na |
|---|---|
| | 0.03 |
| sd | 0.01 |

| | x(Si,T1) | x(Al,M1) | x(Fe3,M1) |
|---|---|---|---|
| | 0.973 | 0.142 | 0.838 |
| sd | 0.006 | 0.004 | 0.004 |

| | x(Ca,M2) | x(Fe2,M2) | x(Mg,M2) |
|---|---|---|---|
| | 0.961 | 0.035 | 0.010 |
| sd | 0.010 | 0.008 | 0.002 |

| | x | sd(x) | % |
|---|---|---|---|
| x(gr) | 0.0166 | 0.000918 | 5.5 |

| | | | |
|---|---|---|---|
| x(andr) | 0.573 | 0.0150 | 2.6 |

clinopyroxene: diopside

| | SiO2 | Cr2O3 | Al2O3 | Fe2O3 | FeO | MnO | MgO | CaO |
|---|---|---|---|---|---|---|---|---|
| | 49.28 | 0.36 | 1.57 | 8.45 | 4.24 | 0.16 | 10.63 | 21.57 |
| sd | 0.54 | 0.05 | 0.07 | 0.96 | 0.85 | 0.05 | 0.16 | 0.27 |

| | Na2O | Total |
|---|---|---|
| | 1.72 | 97.97 |
| sd | 0.07 | 0.64 |

| | Si | Cr | Al | Fe3 | Fe2 | Mn | Mg | Ca |
|---|---|---|---|---|---|---|---|---|
| | 1.90 | 0.01 | 0.07 | 0.25 | 0.14 | 0.01 | 0.61 | 0.89 |
| sd | 0.01 | 0.00 | 0.00 | 0.03 | 0.03 | 0.00 | 0.01 | 0.01 |

| | Na |
|---|---|
| | 0.13 |
| sd | 0.00 |

| | x(Si,T1) | x(Al,T1) | x(Fe2,M1) | x(Mg,M1) |
|---|---|---|---|---|
| | 0.950 | 0.036 | 0.137 | 0.611 |
| sd | 0.007 | 0.001 | 0.027 | 0.009 |

| | x(Ca,M2) | x(Na,M2) |
|---|---|---|
| | 0.891 | 0.128 |
| sd | 0.010 | 0.005 |

| | x | sd(x) | % |
|---|---|---|---|
| x(di) | 0.544 | 0.00907 | 1.7 |
| x(hed) | 0.122 | 0.0233 | 19.1 |

## A1017-JPT092 CALC-SILICATE

Mt Adams Valley Mélange

Not recalculated: sphene, wollastonite, calcite

clinopyroxene: diopside

| | SiO2 | TiO2 | Cr2O3 | Al2O3 | Fe2O3 | FeO | MnO | MgO | CaO |
|---|---|---|---|---|---|---|---|---|---|
| | 50.15 | 0.02 | 0.32 | 1.56 | 3.34 | 7.74 | 0.88 | 9.86 | 23.46 |
| sd | 0.55 | 0.05 | 0.05 | 0.07 | 0.96 | 0.85 | 0.06 | 0.15 | 0.28 |

| | Na2O | Total |
|---|---|---|
| | 0.81 | 98.14 |
| sd | 0.06 | 0.64 |

| | Si | Ti | Cr | Al | Fe3 | Fe2 | Mn | Mg | Ca |
|---|---|---|---|---|---|---|---|---|---|
| | 1.94 | 0.00 | 0.01 | 0.07 | 0.10 | 0.25 | 0.03 | 0.57 | 0.97 |
| sd | 0.01 | 0.00 | 0.00 | 0.00 | 0.03 | 0.03 | 0.00 | 0.01 | 0.01 |

| | Na |
|---|---|
| | 0.06 |
| sd | 0.00 |

| | x(Si,T1) | x(Al,T1) | x(Al,M1) | x(Fe2,M1) | x(Mg,M1) |
|---|---|---|---|---|---|
| | 0.970 | 0.030 | 0.012 | 0.251 | 0.568 |
| sd | 0.007 | 0.007 | 0.013 | 0.027 | 0.008 |

| | x(Ca,M2) | x(Na,M2) |
|---|---|---|
| | 0.973 | 0.060 |
| sd | 0.011 | 0.004 |

| | x | sd(x) | % |
|---|---|---|---|
| x(di) | 0.553 | 0.00931 | 1.7 |
| x(hed) | 0.244 | 0.0246 | 10.1 |
| x(cats) | 0.0114 | 0.0128 | 112.4 |

garnet: grossular-andradite

| | SiO2 | TiO2 | Cr2O3 | Al2O3 | Fe2O3 | MnO | MgO | CaO |
|---|---|---|---|---|---|---|---|---|
| | 36.40 | 1.63 | 0.31 | 12.48 | 13.32 | 0.49 | 0.21 | 34.34 |
| sd | 0.41 | 0.07 | 0.05 | 0.17 | 0.19 | 0.05 | 0.05 | 0.39 |

| | Total |
|---|---|
| | 99.18 |
| sd | 0.64 |

| | Si | Ti | Cr | Al | Fe3 | Mn | Mg | Ca |
|---|---|---|---|---|---|---|---|---|
| | 2.91 | 0.10 | 0.02 | 1.17 | 0.80 | 0.03 | 0.02 | 2.94 |
| sd | 0.02 | 0.00 | 0.00 | 0.02 | 0.01 | 0.00 | 0.01 | 0.03 |

| | x(Si,T1) | x(Al,M1) | x(Fe3,M1) |
|---|---|---|---|
| | 0.969 | 0.587 | 0.400 |
| sd | 0.007 | 0.008 | 0.006 |

| | x(Ca,M2) | x(Mg,M2) |
|---|---|---|
| | 0.980 | 0.008 |
| sd | 0.010 | 0.002 |

| | x | sd(x) | % |
|---|---|---|---|
| x(gr) | 0.295 | 0.00705 | 2.4 |
| x(andr) | 0.137 | 0.00404 | 2.9 |

## feldspar: oligoclase

| | SiO2 | Cr2O3 | Al2O3 | CaO |
|---|---|---|---|---|
| | 53.16 | 0.04 | 22.42 | 8.25 |
| sd | 0.58 | 0.05 | 0.27 | 0.13 |

| | Na2O | K2O | Total |
|---|---|---|---|
| | 7.97 | 1.02 | 92.85 |
| sd | 0.13 | 0.06 | 0.67 |

| | Si | Cr | Al | Ca |
|---|---|---|---|---|
| | 2.61 | 0.00 | 1.30 | 0.43 |
| sd | 0.01 | 0.00 | 0.02 | 0.01 |

| | Na | K |
|---|---|---|
| | 0.76 | 0.06 |
| sd | 0.01 | 0.00 |

| | x(Si,T1) | x(Al,T1) |
|---|---|---|
| | 0.651 | 0.324 |
| sd | 0.003 | 0.004 |

| | x(Ca,A) | x(Na,A) | x(K,A) |
|---|---|---|---|
| | 0.433 | 0.758 | 0.064 |
| sd | 0.007 | 0.013 | 0.004 |

| | x | sd(x) | % |
|---|---|---|---|
| x(an) | 0.345 | 0.00507 | 1.5 |
| x(ab) | 0.604 | 0.00544 | 0.9 |
| x(or) | 0.0507 | 0.00290 | 5.7 |

## feldspar: orthoclase

| | SiO2 | TiO2 | Al2O3 | CaO |
|---|---|---|---|---|
| | 61.30 | 0.53 | 17.79 | 0.24 |
| sd | 0.66 | 0.06 | 0.23 | 0.05 |

| | Na2O | K2O | Total |
|---|---|---|---|
| | 1.15 | 14.38 | 95.39 |
| sd | 0.06 | 0.19 | 0.73 |

| | Si | Ti | Al | Ca |
|---|---|---|---|---|
| | 2.96 | 0.02 | 1.01 | 0.01 |
| sd | 0.01 | 0.00 | 0.01 | 0.00 |

| | Na | K |
|---|---|---|
| | 0.11 | 0.89 |
| sd | 0.01 | 0.01 |

| | x(Si,T1) | x(Al,T1) |
|---|---|---|
| | 0.741 | 0.254 |
| sd | 0.003 | 0.003 |

| | x(Ca,A) | x(Na,A) | x(K,A) |
|---|---|---|---|
| | 0.012 | 0.108 | 0.887 |
| sd | 0.003 | 0.006 | 0.014 |

| | x | sd(x) | % |
|---|---|---|---|
| x(an) | 0.0123 | 0.00266 | 21.7 |
| x(ab) | 0.107 | 0.00527 | 4.9 |
| x(or) | 0.881 | 0.00574 | 0.7 |

Four Mile Creek Gneisses

Not recalculated: quartz

epidote

| | SiO2 | TiO2 | Cr2O3 | Al2O3 | Fe2O3 | MnO | MgO | CaO |
|---|---|---|---|---|---|---|---|---|
| | 36.26 | 0.04 | 0.10 | 21.32 | 15.72 | 0.09 | 0.16 | 22.90 |
| sd | 0.41 | 0.05 | 0.05 | 0.26 | 0.21 | 0.05 | 0.05 | 0.28 |

| | Na2O | H2O | Total |
|---|---|---|---|
| | 0.24 | 1.84 | 98.66 |
| sd | 0.05 | 0.01 | 0.62 |

| | Si | Ti | Cr | Al | Fe3 | Mn | Mg | Ca |
|---|---|---|---|---|---|---|---|---|
| | 2.96 | 0.00 | 0.01 | 2.05 | 0.97 | 0.01 | 0.02 | 2.00 |
| sd | 0.02 | 0.00 | 0.00 | 0.02 | 0.01 | 0.00 | 0.01 | 0.02 |

| | Na | OH |
|---|---|---|
| | 0.04 | 1.00 |
| sd | 0.01 | 0 |

| | x(Si,T1) | x(Al,M1) | x(Fe3,M1) |
|---|---|---|---|
| | 0.986 | 0.035 | 0.965 |
| sd | 0.007 | 0.013 | 0.013 |

| | x(Ca,M2) |
|---|---|
| | 1.000 |
| sd | 0 |

| | x | sd(x) | % |
|---|---|---|---|
| x(cz) | 0.0347 | 0.0133 | 38.3 |
| x(ep) | 0.965 | 0.0132 | 1.4 |

feldspar: anorthite

| | SiO2 | TiO2 | Cr2O3 | Al2O3 | Fe2O3 | MgO | CaO |
|---|---|---|---|---|---|---|---|
| | 42.55 | 0.03 | 0.21 | 34.88 | 0.48 | 0.18 | 19.88 |
| sd | 0.48 | 0.05 | 0.05 | 0.40 | 0.06 | 0.05 | 0.25 |

| | Na2O | K2O | Total |
|---|---|---|---|
| | 0.19 | 0.14 | 98.53 |
| sd | 0.05 | 0.05 | 0.68 |

| | Si | Ti | Cr | Al | Fe3 | Mg | Ca |
|---|---|---|---|---|---|---|---|
| | 2.01 | 0.00 | 0.01 | 1.94 | 0.02 | 0.01 | 1.01 |
| sd | 0.01 | 0.00 | 0.00 | 0.02 | 0.00 | 0.00 | 0.01 |

| | Na | K |
|---|---|---|
| | 0.02 | 0.01 |
| sd | 0.00 | 0.00 |

| | x(Si,T1) | x(Al,T1) |
|---|---|---|
| | 0.502 | 0.485 |
| sd | 0.004 | 0.005 |

| | x(Ca,A) | x(Na,A) | x(K,A) |
|---|---|---|---|
| | 1.000 | 0.017 | 0.008 |
| sd | 0 | 0.005 | 0.003 |

| | x | sd(x) | % |
|---|---|---|---|
| x(an) | 0.975 | 0.00538 | 0.6 |
| x(ab) | 0.0167 | 0.00455 | 27.2 |

A1017-JPT108 2-PYROXENE GRANULITE

Mt Adams Valley Mélange

orthopyroxene: enstatite

| | SiO2 | TiO2 | Cr2O3 | Al2O3 | Fe2O3 | FeO | MnO | MgO | CaO |
|---|---|---|---|---|---|---|---|---|---|
| | 49.65 | 0.23 | 0.17 | 1.17 | 3.90 | 21.61 | 0.61 | 20.47 | 0.43 |
| sd | 0.55 | 0.05 | 0.05 | 0.06 | 0.97 | 0.82 | 0.06 | 0.25 | 0.05 |

| | K2O | Total |
|---|---|---|
| | 0.10 | 98.35 |
| sd | 0.05 | 0.67 |

| | Si | Ti | Cr | Al | Fe3 | Fe2 | Mn | Mg | Ca |
|---|---|---|---|---|---|---|---|---|---|

| | | | | | | | | | |
|---|---|---|---|---|---|---|---|---|---|
| | 1.91 | 0.01 | 0.01 | 0.05 | 0.11 | 0.70 | 0.02 | 1.17 | 0.02 |
| sd | 0.01 | 0.00 | 0.00 | 0.00 | 0.03 | 0.03 | 0.00 | 0.01 | 0.00 |

| | K |
|---|---|
| | 0.00 |
| sd | 0.00 |

| | x(Si,T1) | x(Al,T1) | x(Fe2,M1) | x(Mg,M1) |
|---|---|---|---|---|
| | 0.955 | 0.027 | 0.327 | 0.553 |
| sd | 0.007 | 0.001 | 0.019 | 0.010 |

| | x(Ca,M2) | x(Fe2,M2) | x(Mg,M2) |
|---|---|---|---|
| | 0.018 | 0.368 | 0.621 |
| sd | 0.002 | 0.007 | 0.019 |

| | x | sd(x) | % |
|---|---|---|---|
| x(en) | 0.343 | 0.00665 | 1.9 |
| x(fs) | 0.120 | 0.00907 | 7.5 |

## clinopyroxene: diopside

| | SiO2 | TiO2 | Cr2O3 | Al2O3 | Fe2O3 | FeO | MnO | MgO | CaO |
|---|---|---|---|---|---|---|---|---|---|
| | 49.56 | 0.17 | 0.58 | 2.14 | 3.26 | 7.86 | 0.38 | 12.35 | 21.82 |
| sd | 0.55 | 0.05 | 0.06 | 0.07 | 0.97 | 0.85 | 0.05 | 0.17 | 0.27 |

| | Na2O | K2O | Total |
|---|---|---|---|
| | 0.22 | 0.06 | 98.39 |
| sd | 0.05 | 0.05 | 0.64 |

| | Si | Ti | Cr | Al | Fe3 | Fe2 | Mn | Mg | Ca |
|---|---|---|---|---|---|---|---|---|---|
| | 1.90 | 0.00 | 0.02 | 0.10 | 0.09 | 0.25 | 0.01 | 0.71 | 0.90 |
| sd | 0.01 | 0.00 | 0.00 | 0.00 | 0.03 | 0.03 | 0.00 | 0.01 | 0.01 |

| | Na | K |
|---|---|---|
| | 0.02 | 0.00 |
| sd | 0.00 | 0.00 |

| | x(Si,T1) | x(Al,T1) | x(Fe2,M1) | x(Mg,M1) |
|---|---|---|---|---|
| | 0.950 | 0.048 | 0.237 | 0.664 |
| sd | 0.007 | 0.002 | 0.027 | 0.005 |

| | x(Ca,M2) | x(Na,M2) | x(Fe2,M2) | x(Mg,M2) |
|---|---|---|---|---|
| | 0.897 | 0.017 | 0.015 | 0.042 |
| sd | 0.010 | 0.004 | 0.002 | 0.008 |

| | x | sd(x) | % |
|---|---|---|---|
| x(di) | 0.595 | 0.00722 | 1.2 |
| x(hed) | 0.213 | 0.0232 | 10.9 |

## ilmenite

| | SiO2 | TiO2 | Cr2O3 | Al2O3 | Fe2O3 | FeO | MnO | MgO | CaO |
|---|---|---|---|---|---|---|---|---|---|
| | 0.01 | 48.79 | 0.03 | 0.05 | 7.02 | 42.28 | 1.08 | 0.25 | 0.06 |
| sd | 0.05 | 0.54 | 0.05 | 0.05 | 0.82 | 0.50 | 0.06 | 0.05 | 0.05 |

| | Na2O | K2O | Total |
|---|---|---|---|
| | 0.15 | 0.03 | 99.78 |
| sd | 0.05 | 0.05 | 0.78 |

| | Si | Ti | Cr | Al | Fe3 | Fe2 | Mn | Mg | Ca |
|---|---|---|---|---|---|---|---|---|---|
| | 0.00 | 0.93 | 0.00 | 0.00 | 0.13 | 0.90 | 0.02 | 0.01 | 0.00 |
| sd | 0.00 | 0.01 | 0.00 | 0.00 | 0.02 | 0.01 | 0.00 | 0.00 | 0.00 |

| | Na | K |
|---|---|---|
| | 0.01 | 0.00 |
| sd | 0.00 | 0.00 |

## feldspar: oligoclase

| | SiO2 | TiO2 | Cr2O3 | Al2O3 | Fe2O3 | MnO | CaO |
|---|---|---|---|---|---|---|---|
| | 51.49 | 0.01 | 0.11 | 28.44 | 0.32 | 0.18 | 11.83 |
| sd | 0.56 | 0.05 | 0.05 | 0.33 | 0.06 | 0.05 | 0.17 |

| | Na2O | K2O | Total |
|---|---|---|---|
| | 4.45 | 0.09 | 96.92 |
| sd | 0.09 | 0.05 | 0.69 |

| | Si | Ti | Cr | Al | Fe3 | Mn | Ca |
|---|---|---|---|---|---|---|---|
| | 2.41 | 0.00 | 0.00 | 1.57 | 0.01 | 0.01 | 0.59 |

| | | | | | | | |
|---|---|---|---|---|---|---|---|
| sd | 0.01 | 0.00 | 0.00 | 0.02 | 0.00 | 0.00 | 0.01 |

| Na | K |
|---|---|
| 0.40 | 0.01 |
| 0.01 | 0.00 |

| x(Si,T1) | x(Al,T1) |
|---|---|
| 0.602 | 0.392 |
| 0.003 | 0.004 |

| x(Ca,A) | x(Na,A) | x(K,A) |
|---|---|---|
| 0.593 | 0.404 | 0.005 |
| 0.009 | 0.009 | 0.003 |

| | x | sd(x) | % |
|---|---|---|---|
| x(an) | 0.592 | 0.00639 | 1.1 |
| x(ab) | 0.403 | 0.00625 | 1.6 |

## feldspar: orthoclase

| | SiO2 | TiO2 | Cr2O3 | Al2O3 | CaO |
|---|---|---|---|---|---|
| | 61.31 | 0.24 | 0.11 | 19.99 | 0.50 |
| sd | 0.66 | 0.05 | 0.05 | 0.25 | 0.05 |

| Na2O | K2O | Total |
|---|---|---|
| 0.69 | 14.77 | 97.60 |
| 0.06 | 0.20 | 0.74 |

| Si | Ti | Cr | Al | Ca |
|---|---|---|---|---|
| 2.90 | 0.01 | 0.00 | 1.12 | 0.03 |
| 0.01 | 0.00 | 0.00 | 0.01 | 0.00 |

| Na | K |
|---|---|
| 0.06 | 0.89 |
| 0.01 | 0.01 |

| x(Si,T1) | x(Al,T1) |
|---|---|
| 0.725 | 0.275 |
| 0.003 | 0.003 |

| x(Ca,A) | x(Na,A) | x(K,A) |
|---|---|---|
| 0.025 | 0.063 | 0.891 |
| 0.003 | 0.005 | 0.013 |

| | x | sd(x) | % |
|---|---|---|---|
| x(an) | 0.0257 | 0.00279 | 10.9 |
| x(ab) | 0.0648 | 0.00505 | 7.8 |
| x(or) | 0.910 | 0.00561 | 0.6 |

## amphibole: hornblende (retrograde)

| | SiO2 | TiO2 | Cr2O3 | Al2O3 | Fe2O3 | FeO | MnO | MgO | CaO |
|---|---|---|---|---|---|---|---|---|---|
| | 35.92 | 1.02 | 0.13 | 12.50 | 3.59 | 18.30 | 0.06 | 6.79 | 11.22 |
| sd | 0.41 | 0.06 | 0.05 | 0.18 | 2.39 | 2.17 | 0.05 | 0.12 | 0.16 |

| Na2O | K2O | H2O | Total |
|---|---|---|---|
| 1.09 | 2.93 | 1.83 | 95.37 |
| 0.06 | 0.08 | 0.02 | 0.64 |

| Si | Ti | Cr | Al | Fe3 | Fe2 | Mn | Mg | Ca |
|---|---|---|---|---|---|---|---|---|
| 5.90 | 0.13 | 0.02 | 2.42 | 0.44 | 2.51 | 0.01 | 1.66 | 1.97 |
| 0.05 | 0.01 | 0.01 | 0.04 | 0.29 | 0.31 | 0.01 | 0.03 | 0.03 |

| Na | K | OH |
|---|---|---|
| 0.35 | 0.61 | 2.00 |
| 0.02 | 0.02 | 0 |

| x(Si,T1) | x(Al,T1) | x(Si,T2) | x(Al,M1) | x(Fe2,M1) | x(Mg,M1) |
|---|---|---|---|---|---|
| 0.474 | 0.526 | 1.000 | 0.158 | 0.335 | 0.222 |
| 0.014 | 0.014 | 0 | 0.031 | 0.088 | 0.032 |

| x(Ca,M2) | x(Fe2,M2) | x(Mg,M2) | x(Fe2,M3) | x(Mg,M3) | x(v,A) |
|---|---|---|---|---|---|
| 0.986 | 0.018 | 0.012 | 0.602 | 0.398 | 0.387 |
| 0.016 | 0.028 | 0.017 | 0.029 | 0.029 | 0.017 |

| | x | sd(x) | % |
|---|---|---|---|
| x(tr) | 0.0000588 | 0.0000113 | 19.2 |
| x(ftr) | 0.000467 | 0.000350 | 75.1 |
| x(hb) | 0.00176 | 0.000341 | 19.4 |
| x(cumm) | 8.436436e-9 | 0.0000000254 | 300.6 |

| | | | |
|---|---|---|---|
| x(grun) | 0.000000153 | 0.000000582 | 379.2 |

## A1017-JPT115 ORTHOAMPHIBOLE-CORDIERITE ROCK

Four Mile Creek Gneisses

### amphibole: anthophyllite

| | SiO2 | TiO2 | Cr2O3 | Al2O3 | Fe2O3 | FeO | MnO | MgO | CaO |
|---|---|---|---|---|---|---|---|---|---|
| | 52.47 | 0.05 | 0.10 | 1.66 | 3.26 | 16.60 | 0.72 | 19.91 | 0.21 |
| sd | 0.57 | 0.05 | 0.05 | 0.07 | 2.17 | 1.96 | 0.06 | 0.25 | 0.05 |

| | H2O | Total |
|---|---|---|
| | 2.04 | 97.02 |
| sd | 0.02 | 0.74 |

| | Si | Ti | Cr | Al | Fe3 | Fe2 | Mn | Mg | Ca |
|---|---|---|---|---|---|---|---|---|---|
| | 7.73 | 0.01 | 0.01 | 0.29 | 0.36 | 2.05 | 0.09 | 4.37 | 0.03 |
| sd | 0.05 | 0.01 | 0.01 | 0.01 | 0.24 | 0.25 | 0.01 | 0.06 | 0.01 |

| | OH |
|---|---|
| | 2.00 |
| sd | 0 |

| | x(Si,T1) | x(Al,T1) | x(Si,T2) | x(Al,M1) | x(Fe2,M1) | x(Mg,M1) |
|---|---|---|---|---|---|---|
| | 0.932 | 0.068 | 1.000 | 0.009 | 0.258 | 0.550 |
| sd | 0.014 | 0.014 | 0 | 0.027 | 0.052 | 0.048 |

| | x(Ca,M2) | x(Fe2,M2) | x(Mg,M2) | x(Fe2,M3) | x(Mg,M3) | x(v,A) |
|---|---|---|---|---|---|---|
| | 0.016 | 0.287 | 0.613 | 0.319 | 0.681 | 1.000 |
| sd | 0.004 | 0.036 | 0.013 | 0.026 | 0.026 | 0 |

| | x | sd(x) | % |
|---|---|---|---|
| x(tr) | 0.0000191 | 0.00000991 | 51.8 |
| x(ftr) | 0.000000429 | 0.000000371 | 86.4 |
| x(hb) | 0.000000869 | 0.00000246 | 282.6 |
| x(cumm) | 0.0272 | 0.00351 | 12.9 |
| x(grun) | 0.000134 | 0.000125 | 93.7 |

### cordierite

| | SiO2 | TiO2 | Cr2O3 | Al2O3 | Fe2O3 | FeO | MnO | MgO | CaO |
|---|---|---|---|---|---|---|---|---|---|
| | 48.04 | 0.01 | 0.16 | 32.90 | 0.17 | 4.59 | 0.03 | 10.10 | 0.17 |
| sd | 0.53 | 0.05 | 0.05 | 0.38 | 0.69 | 0.60 | 0.05 | 0.15 | 0.05 |

| | Total |
|---|---|
| | 96.17 |
| sd | 0.66 |

| | Si | Ti | Cr | Al | Fe3 | Fe2 | Mn | Mg | Ca |
|---|---|---|---|---|---|---|---|---|---|
| | 4.98 | 0.00 | 0.01 | 4.02 | 0.01 | 0.40 | 0.00 | 1.56 | 0.02 |
| sd | 0.04 | 0.00 | 0.00 | 0.04 | 0.05 | 0.05 | 0.00 | 0.02 | 0.01 |

| | x(Fe2,M1) | x(Mg,M1) |
|---|---|---|
| | 0.199 | 0.779 |
| sd | 0.026 | 0.011 |

| | x | sd(x) | % |
|---|---|---|---|
| x(crd) | 0.607 | 0.0175 | 2.9 |
| x(fcrd) | 0.0395 | 0.0103 | 26.1 |

### feldspar: anorthite

| | SiO2 | Cr2O3 | Al2O3 | Fe2O3 | MgO | CaO |
|---|---|---|---|---|---|---|
| | 44.97 | 0.39 | 33.18 | 0.12 | 0.18 | 17.08 |
| sd | 0.50 | 0.05 | 0.38 | 0.06 | 0.05 | 0.22 |

| | Na2O | Total |
|---|---|---|
| | 2.01 | 97.93 |
| sd | 0.07 | 0.68 |

| | Si | Cr | Al | Fe3 | Mg | Ca |
|---|---|---|---|---|---|---|
| | 2.12 | 0.01 | 1.84 | 0.00 | 0.01 | 0.86 |
| sd | 0.01 | 0.00 | 0.02 | 0.00 | 0.00 | 0.01 |

| | Na |
|---|---|
| | 0.18 |
| sd | 0.01 |

| | x(Si,T1) | x(Al,T1) |
|---|---|---|
| | 0.530 | 0.461 |
| sd | 0.004 | 0.004 |

| | x(Ca,A) | x(Na,A) |
|---|---|---|
| | 0.863 | 0.183 |
| sd | 0.012 | 0.006 |

| | x | sd(x) | % |
|---|---|---|---|
| x(an) | 0.825 | 0.00538 | 0.7 |
| x(ab) | 0.175 | 0.00538 | 3.1 |

ilmenite

| | SiO2 | TiO2 | Cr2O3 | Al2O3 | Fe2O3 | FeO | MnO | MgO |
|---|---|---|---|---|---|---|---|---|
| | 0.14 | 47.38 | 0.15 | 0.26 | 8.44 | 41.08 | 0.54 | 0.65 |
| sd | 0.05 | 0.52 | 0.05 | 0.05 | 0.81 | 0.49 | 0.06 | 0.06 |

| | Total |
|---|---|
| | 98.62 |
| sd | 0.77 |

| | Si | Ti | Cr | Al | Fe3 | Fe2 | Mn | Mg |
|---|---|---|---|---|---|---|---|---|
| | 0.00 | 0.91 | 0.00 | 0.01 | 0.16 | 0.88 | 0.01 | 0.02 |
| sd | 0.00 | 0.01 | 0.00 | 0.00 | 0.02 | 0.01 | 0.00 | 0.00 |

## 2 Geothermometry

The garnet-biotite geothermometer of Powell & Holland [1990] is expressed as follows:

$$T = \frac{44.97}{0.01456 + 3R \ln K_D}$$

where $T$ is the maximum metamorphic temperature, $R$ is the gas constant (in $kJmol^{-1}K^{-1}$) and $K_D$ is the distribution coefficient and is given by:

$$K_D = \frac{1 - X_{Mg}^{garnet}}{X_{Mg}^{garnet}} \frac{X_{Mg}^{biotite}}{1 - X_{Mg}^{biotite}}$$

Values for $X_{Mg}$ (the molar proportion of magnesium) are obtained from the above RECALC results.

The clinopyroxene-orthopyroxene geothermometer of Wells[1977] is expressed as follows:

$$T = \frac{7341}{3.355 + 2.44 X_{Fe}^{opx} - \ln K_D}$$

where $T$ is the closure temperature and $K_D$ is the distribution coefficient which is given by:

$$K_D = \frac{a_{Mg_2Si_2O_6}^{cpx}}{a_{Mg_2Si_2O_6}^{opx}}$$

Here the approximation $a_{Mg_2Si_2O_6} = X_{Mg_2Si_2O_6}$ was used. Values for $X_{Mg}$ and $X_{Fe}$ were taken from the above RECALC data.

# Appendix 4

## Sample data

Key: TS=Thin section cut [s=by SADME, •=by department], P=Probed.

| Sample No. | TS | P | Unit | Description |
|---|---|---|---|---|
| A1017-JPT001 | s | - | Yagdlin Phyllite | Sapphire-tourmaline schist |
| A1017-JPT002 | • | - | " | Foliated phyllite with retrograde cordierite porphyroblasts |
| A1017-JPT004 | • | - | Mylonite | Mylonitised Mt Neill Granite Porphyry |
| A1017-JPT008 | • | - | Four Mile Creek Gneiss | Sillimanite gneiss with large coin-shaped pods of fibrous sillimanite |
| A1017-JPT010 | • | • | Freeling Heights Metasediments | Garnet-biotite-?cordierite schist |
| A1017-JPT012 | • | - | Four Mile Creek Gneiss | Clinopyroxene-bearing calc silicate |
| A1017-JPT013 | • | - | " | Sillimanite gneiss |
| A1017-JPT018 | • | - | Mount Adams Quartzite | Kink folded feldspathic, micaceous quartzite |
| A1017-JPT024 | s | - | Freeling Heights Quartzite | Fine grained, micaceous quartzite with heavy mineral laminations |
| A1017-JPT026 | • | - | Four Mile Creek Gneiss | Sillimanite gneiss |
| A1017-JPT027 | s | - | " | Sillimanite gneiss with fibrous sillimanite and Kfeldspar growing from quartz and muscovite |
| A1017-JPT028 | s | - | " | Biotite schist with abundant zircons with pleochroic halos. |
| A1017-JPT029a | s | • | " | Biotite-sillimanite-muscovite-Kfeldspar-quartz schist |
| A1017-JPT029d | • | • | " | Sillimanite-tourmaline schist with large green tourmaline porphyroblasts and abundant fibrous sillimanite |
| A1017-JPT033 | s | • | Mt Adams Valley Mélange | Olivine gabbro with spectacular symplectites of spinel and clinopyroxene forming from olivine and plagioclase. Rock also contains kaersutite |
| A1017-JPT034 | s | - | " | Unusual weathered ?igneous rock containing green weathering minerals and abundant magnetite |
| A1017-JPT035 | s | - | " | Weathered calc-silicate found adjacent to previous. Allotriomorphic texture. |
| A1017-JPT038 | s | - | " | Bizarre metasomatised dolomite with spherical scapolite crystals and prismatic tourmaline ("Dalmatian skarn") |
| A1017-JPT040 | • | - | " | Mt Adams Valley Mélange. Chaotic mass of grits and clays supporting numerous exotic clasts |
| A1017-JPT042 | s | - | Mt Neill Granite Porphyry | Sheared granite |
| A1017-JPT043 | s | | ?Yagdlin Phyllite | Coarse grained, green, sapphire-chlorite-phlogopite schist |
| A1017-JPT044 | ss | • | ?" | As above, with strange concentric reaction rims in large relict porphyroblasts (now spinel + chlorite) |
| A1017-JPT045 | s | - | Mt Neill Granite Porphyry | Sheared granite |
| A1017-JPT047 | • | - | Freeling Heights Metasediments | Massive, dirty quartzite |
| A1017-JPT048 | s | • | " | Biotite schist with large relict hexagonal porphyroblasts (now quartz groundmass) and abundant ilmenite |
| A1017-JPT049 | • | - | " | Biotite schist with relict ?garnet |
| A1017-JPT051 | s | - | Four Mile Creek Gneiss | Sillimanite gneiss |
| A1017-JPT054 | s | - | " | Allanite bearing granite gneiss with symplectic reaction textures between feldspars and abundant opaques |
| A1017-JPT056 | • | - | " | Red leucocratic quartz undersaturated granite gneiss with abundant primary sulfides |

| | | | | |
|---|---|---|---|---|
| A1017-JPT057 | s | • | Freeling Heights Metasediments | Epidote-scapolite-plagioclase quartzite (highly recrystallised) |
| A1017-JPT060 | • | • | Four Mile Creek Gneiss | Highly radioactive amphibolite with isoclinally folded feldspar vein. |
| A1017-JPT061 | • | - | " | Paragneiss (quartzitic) |
| A1017-JPT066 | • | • | " | Highly strained paragneiss with sillimanite, quartz, orange Kfeldspar, micas and magnetite |
| A1017-JPT068 | s | • | Freeling Heights Metasediments | Coarse grained biotite schist with large (2cm) relict porphyroblasts (now quartz groundmass) |
| A1017-JPT070 | •• | - | Mylonites | Mylonitised paragneiss with strong foliation and lineation defined by sillimanite and mica |
| A1017-JPT071 | s | - | " | Mylonitised leucogneiss? |
| A1017-JPT072 | • | • | Four Mile Creek Gneiss | Biotite schist with folded quartz veins |
| A1017-JPT074 | s | • | Mt Adams Quartzite | Biotite-phlogopite schist with relict porphyroblasts |
| A1017-JPT075 | s | - | Four Mile Creek Gneiss | Very hard, foliated mafic gneiss with abundant perthitic feldspar and opaques - some hornblende (quite radioactive) |
| A1017-JPT078 | • | • | " | Unusual coarse grained, contact metamorphosed calc-silicate with abundant ilmenite and diopside (not foliated) |
| A1017-JPT079 | s | - | " | " |
| A1017-JPT081 | s | • | " | Lower grade version of previous with prismatic cummingtonite defining the foliation |
| A1017-JPT083 | - | - | " | Crenulated biotite schist |
| A1017-JPT084 | s | • | Mt Adams Valley Mélange | Pink-brown calc-silicate with garnet and diopside (highly recrystallised, very coarse grained) |
| A1017-JPT085 | s | • | " | " (with sphene) |
| A1017-JPT086 | •• | • | " | " |
| A1017-JPT087 | - | - | " | Troctolite |
| A1017-JPT089 | s | • | " | Crenulated, hard pelite with biotite reacting to corundum |
| A1017-JPT090 | • | • | " | Biotite bearing calc-silicate |
| A1017-JPT092 | s | • | " | Wollastonite bearing calc-silicate with garnet, diopside, sphene, 2 feldspars and ilmenite-highly recrystallised |
| A1017-JPT096 | • | • | Four Mile Creek Gneiss | Epidote-scapolite-quartz-plagioclase rock |
| A1017-JPT097 | • | - | " | Sillimanite gneiss |
| A1017-JPT100 | • | - | Yagdlin Phyllite | - |
| A1017-JPT101 | • | - | Mt Neill Granite? | Highly sheared ?granite |
| A1017-JPT102 | • | - | Yagdlin Phyllite | - |
| A1017-JPT104 | • | • | " | Contact metamorphosed phyllite with abundant sillimanite prisms (randomly oriented) |
| A1017-JPT105 | • | • | " | Phyllite with 2 phases of porphyroblastesis |
| A1017-JPT107 | • | • | " | Phyllite with large sillimanite prisms |
| A1017-JPT108 | • | • | Mt Adams Valley Mélange | Two pyroxene granulite |
| A1017-JPT110 | • | - | " | Mylonitised granite with blue quartz |
| A1017-JPT112 | • | • | Four Mile Creek Gneiss | Biotite-cordierite-(garnet) schist |
| A1017-JPT114 | • | • | Mt Adams Valley Mélange | Two pyroxene granulite |
| A1017-JPT115 | •• | •• | Four Mile Creek Gneiss | Cordierite-orthoamphibole rock |
| A1017-JPT116 | • | - | " | Mylonitised paragneiss |
| A1017-JPT117 | • | • | " | Cordierite-biotite schist |
| A1017-JPT118 | • | • | Yagdlin Phyllite | Phyllite with large sillimanite prisms reacting to sapphire |
| A1017-JHV78 | • | • | " | Garnetiferous phyllite |

# Appendix 5

## Map and block diagram

See pocket inside back cover.

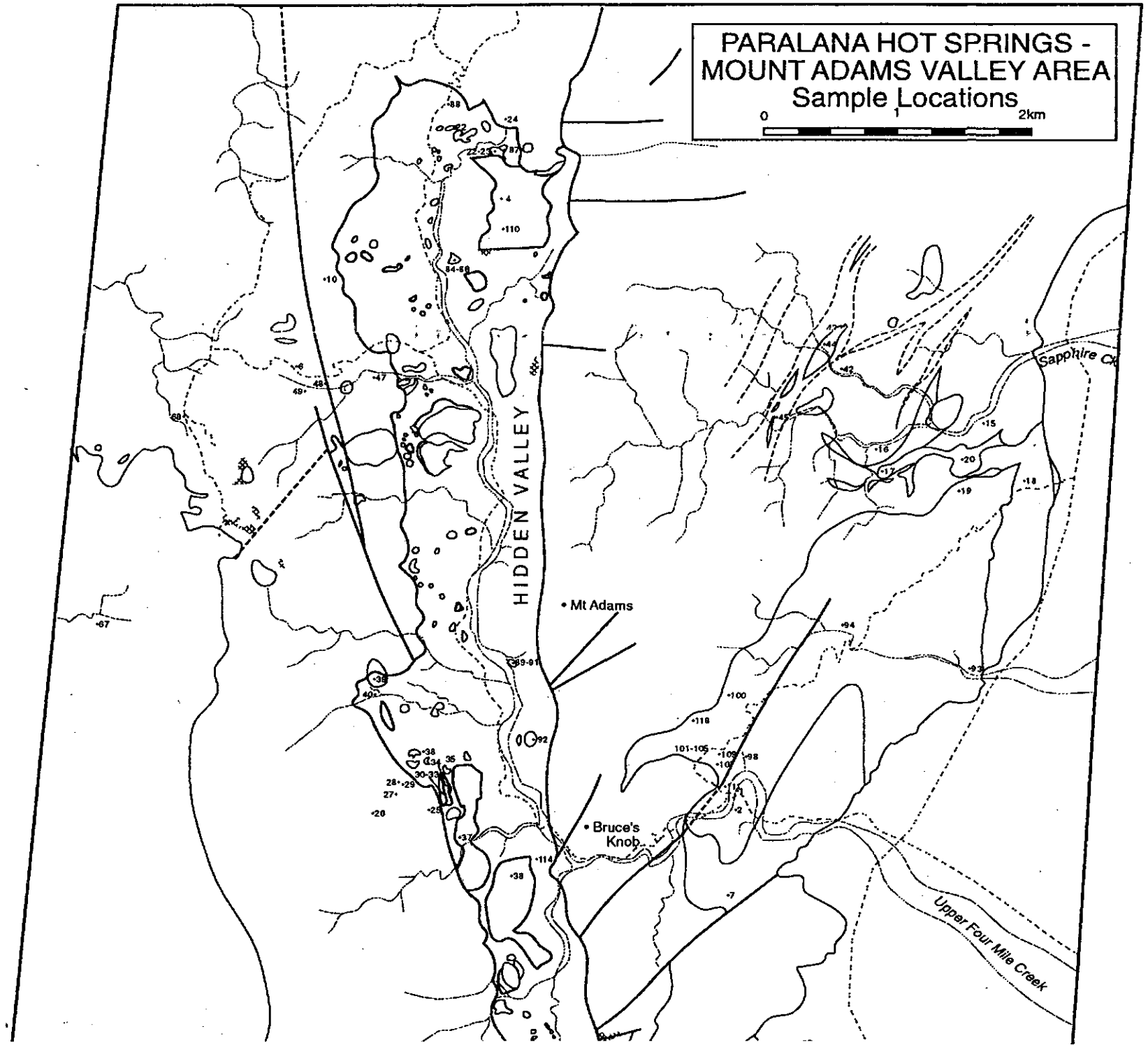
PARALANA HOT SPRINGS -
MOUNT ADAMS VALLEY AREA
Sample Locations
0
1
2km
HIDDEN VALLEY
Mt Adams
Bruce's Knob
Upper Four Mile Creek
Sapphire Cr

Four Mile Creek
Mylonite Creek
Hot Springs Creek
Paralana Hot Springs
Paralana Plateau
MAWSON PLATEA
N
S
E
W

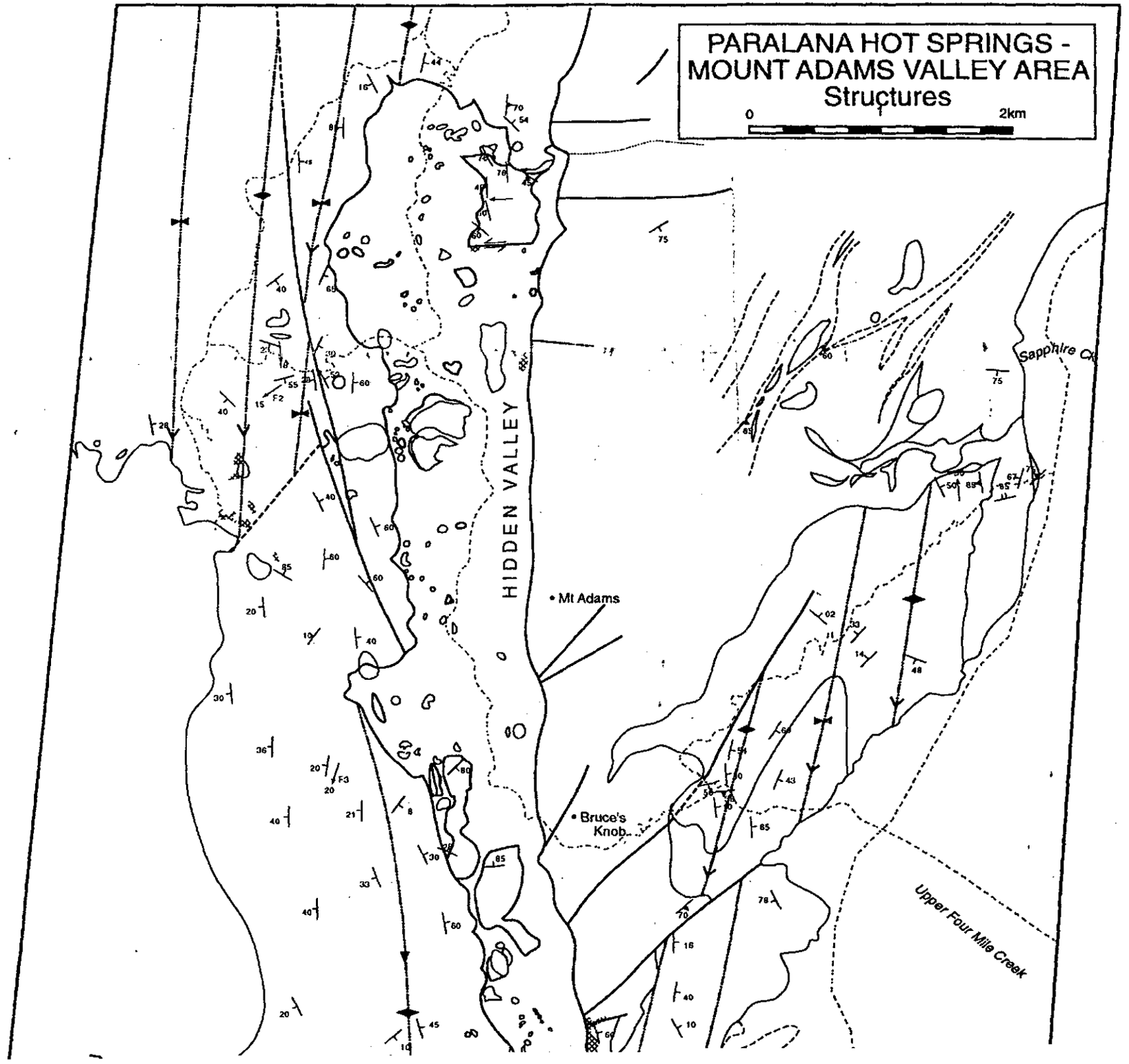
PARALANA HOT SPRINGS -
MOUNT ADAMS VALLEY AREA
Structures
0
2km
HIDDEN VALLEY
Mt Adams
Bruce's Knob
Upper Four Mile Creek
Sapphire Cr

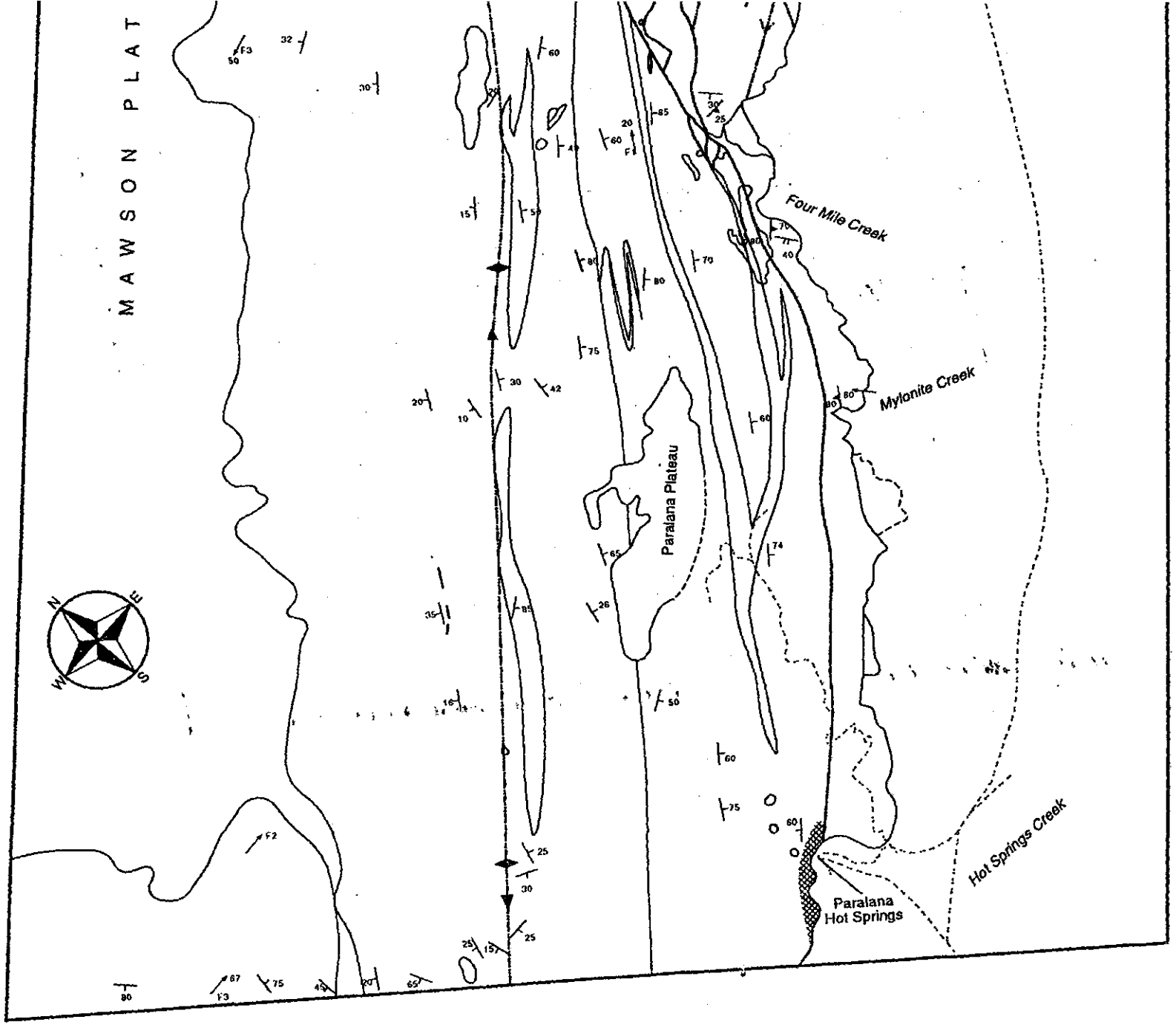
MAWSON PLAT
Four Mile Creek
Mylonite Creek
Paralana Plateau
Paralana
Hot Springs
Hot Springs Creek
N
E
S
W

# LEGEND

## PARALANA HOT SPRINGS - MOUNT ADAMS VALLEY AREA

| | | | |
|---|---|---|---|
| | **Quaternary** | Undifferentiated flat lying alluvial and playa sediments. | |
| | **Tertiary** | Green kaolinised sands and grits, conglomeratic in part. Possibly forms matrix of Mt Adams Valley mélange. | |
| | **Mesozoic** | Pale brown-white weathered fossiliferous sandstones, silicified in part. | |
| ? | **Carbonate** | Massive white calcite, found as rafts in Mt Adams Valley. | |
| ? | **Calc-silicates** | Hard, high grade calc-silicates with complex mineralogies. | |
| PERMIAN | **British Empire Pegmatite** | Massive quartzofeldspathic, micaceous pegmatites. | |
| PERMIAN | **British Empire Granite** | Medium to coarse grained, heterogeneous, undeformed, leucocratic granite. | |
| NEOPROT. - ORDOVICIAN | **Mylonite** | Highly strained L-S tectonite of para- and orthogneissic origin. | |
| NEOPROT. - ORDOVICIAN | **Adelaidean** | Flat lying Adelaidean sediments, interpreted to underlie Mesozoic sediments to the east of the Paralana Fault System. | |
| UNKNOWN | **Troctolite** | Coarse grained, olivine gabbro found as rafts in the Mt Adams Valley Mélange. | |
| UNKNOWN | **Granulite** | High grade mafic, pyroxene-bearing granulites, found as rafts in the Mt Adams Valley Mélange. | |
| MESOPROTEROZOIC | **Corundum Schists** | Sapphire bearing phlogopite - chlorite ± tourmaline schists adjacent to Mt Neill Granite. | |
| MESOPROTEROZOIC | **Amphibolites** | Undifferentiated amphibolites. | |
| MESOPROTEROZOIC | **Mt Neill Granite** | Heterogeneous, quartz undersaturated porphyritic granite - granite syenite, sub-volcanic in part. | |
| MESOPROTEROZOIC | **Freeling Heights Metasediments** | Sequence of massive, crossbedded, micaceous quartzites and mica schists. | |
| MESOPROTEROZOIC | **Mt Adams Quartzite** | Massive, crossbedded, feldspathic quartzite with pelitic interbeds. | |
| MESOPROTEROZOIC | **Yagdlin Phyllite** | Finely laminated brown-green phyllites. | |
| PALAEO-PROTEROZOIC | **Orthogneisses** | Sequence of highly deformed, I- and A-type granite gneisses. | |
| PALAEO-PROTEROZOIC | **Paragneisses** | Highly deformed, quartzofeldspathic migmatites and sillimanite gneisses with pelitic intebeds. | |

| | |
|---|---|
| | **Creeks** |
| | **Lithological boundaries** |
| | **Inferred Lithological Boundaries** |
| | **Faults** |
| | **Inferred Faults** |
| | **Roads** |
| | **Breccia** |
| | **F2 fold axes** |
| 21 | **Bedding** |
| 44 | **Schistosity** (when not parallel to bedding) |
| 75 | **Kink band foliation** |
| 12 | **Lineation** |
| · 58 | **Sample location** |
| | **Tectonic mélange** |
| 36 | **Anticline (with plunge)** |
| 18 | **Syncline (with plunge)** |
| | **Fault vergence** |
| 351000 | **AMG easting** |
| 6659000 | **AMG northing** |

# BLOCK DIAGRAM

## Paralana Hot Springs - Mt Adams Valley area

Scale (km)

0 1 2 3 4 5

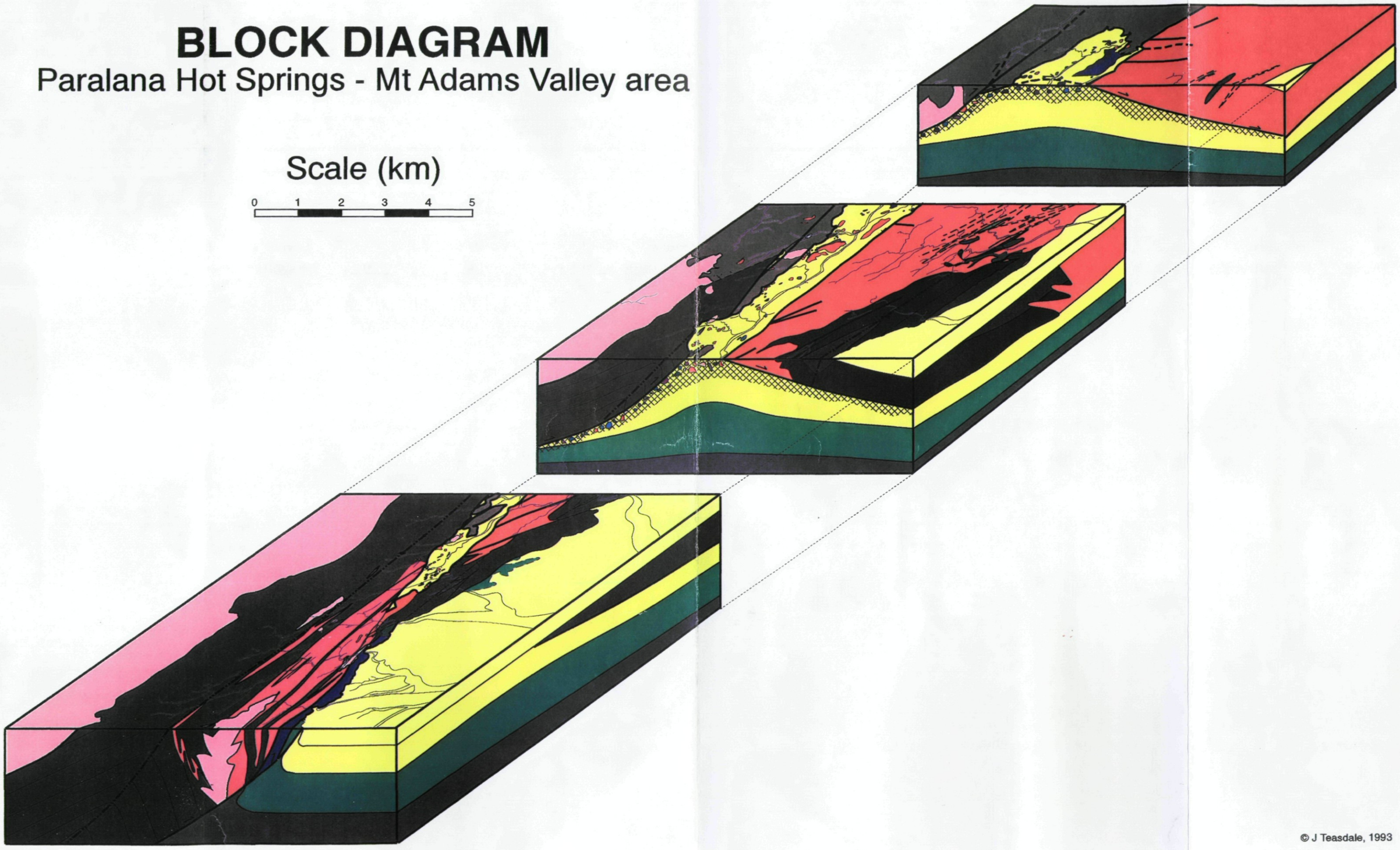

# PARALANA HOT SPRINGS - MOUNT ADAMS VALLEY AREA

0 1 2km

HIDDEN VALLEY

Mt Adams

Bruce's Knob

Upper Four Mile Creek

Four Mile Creek

Mylonite Creek

Paralana Plateau

Hot Springs Creek

Paralana Hot Springs

MAWSON PLATEAU

N E S W